https://doi.org/10.5194/essd-2026-241
Preprint. Discussion started: 24 July 2026

Open Access Earth System Science Data Discussions

The Arctic Radiation-Cloud-Aerosol-Surface Interaction Experiment (ARCSIX) airborne campaign dataset

Patrick C. Taylor[1], Armin Sorooshian[2,3], Rei Ueyama[4], Sebastian Schmidt[5,6], Ihab Abboud[27], Quincy Allison[4,7], Kevin Barry[8], Sebastian Becker[9,10], Holly A. Bender[11], Joseph R. Bennett[4,7], James B. Blair[12], Niklas Bohn[11], Linette Boisvert[12], Matthew D. Brown[1], Roelof Bruintjes[13], Anthony Bucholtz[14], Megan Buzanowicz[1,15], Brian Cairns[16], Filippo Calì Quaglia[17], Eduard Chemyakin[1], Bo Chen[8], Gao Chen[1], Hong Chen[4], Yu-Wen Chen[4,5], Zezhen Cheng[18], Swarup China[18], Dan Chirica[4], Yonghoon Choi[1], Peter Colarco[12], Brian Collister[1], Ewan Crosbie[1,*], Maurice J. Cross[1], Janet Daniels[1,19], Paul DeMott[8], Joshua P. DiGangi[1], Alcide Giorgio di Sarra[20], Glenn S. Diskin[1], Erica K. Dolinar[21], Eva-Lou Edwards[1], Samuel Ephraim[22], Nikolaos Evangeliou[23], Romanos Foskinis[24], Francesca Gallo[1], Lan Gao[25], José Luis Gómez-Amo[26], Daisy Gonzalez[4,7], Christine Groot Zwaaftink[23], Pawan Gupta[12], Ivan Heckman[27], Michael Hendrickson[12,28], Miguel Ricardo A. Hilario[2,**], Ken Hirata[5,6], Michelle Hofton[29], Andrew L. Holen[30], Ulas Im[24,31], Alia L. Khan[32], Ralph A. Kahn[5,12], Alexei V. Korolev[27], Sonia Kreidenweis[8], Thomas Krumpen[33], Nathan Kurtz[12], Leslie Lait[4], Bradley Lamkin[25], Jack Landy[34], Nurun Nahar Lata[18], Paul Lawson[35], Samuel LeBlanc[4,7], Sean Leavor[1,15], Jing Li[36], Thorsten Markus[37], Hal Maring[37], Andreas H. Massling[31], Camille Mavis[8], Flynn McGinnity[38], Kerry Meyer[12], Gabriel Mojica[1,15], Richard H. Moore[1], Parker Morris[35], Giovanni Muscari[17], Vikas Nataraja[4,5], Amin R. Nehrir[1], Athanasios Nenes[24,31,39], Edward P. Nowottnick[37], Matteo Ottaviani[16,40], Chelsea Parker[12,41], Ryan Patnaude[8], Michael Perez[22], Russell J. Perkins[8], Colten Peterson[12,42], Alek Petty[12,41], Stevie Phothisane[4,7], Chris Polashenski[43,44], Kerri A. Pratt[30], Kayla M. Preisler[2], John Prytherch[45], David Rabine[12], Jens Redemann[25], Ju-Mee Ryoo[4,7], Joseph Schlosser[1,46], Vanessa Selimovic[30], Michael A. Shook[1], Morgan Silverman[1,19], Henrik Skov[31], Alexander Smirnov[12,51], Cassidy Soloff[2], Amy Solomon[9], Snorre Stamnes[1], Azusa Takeishi[35,***], David R. Thompson[11], K. Lee Thornhill[1,19], Rachel Tilling[12,41], Michael Tjernström[47], Monica Tosco[17,48,49], Pedro C. Valdelomar[26], David Van Gilst[4,7], Jian Wang[36], Zhien Wang[38], Andrzej Wasilewski[16,28], Manfred Wendisch[50], Brent Wilder[11], Edward L. Winstead[1], Albert Wu[12,15], Peng Xian[21], Lauren M. Zamora[12,41], Jiaoshi Zhang[36], Lei Zhang[36], Lu Zhang[31], Luke Ziemba[1], Paquita Zuidema[22]

[1]NASA Langley Research Center, Hampton, VA 23681, USA
[2]Department of Hydrology and Atmospheric Sciences, University of Arizona, Tucson, AZ 85721, USA
[3]Department of Chemical and Environmental Engineering, University of Arizona, Tucson, AZ 85721, USA
[4]Earth Science Division, NASA Ames Research Center, Moffett Field, CA 94035, USA
[5]Laboratory for Atmospheric and Space Physics, University of Colorado, Boulder, CO 80309, USA
[6]Department of Atmospheric and Oceanic Sciences, University of Colorado, Boulder, CO 80309, USA
[7] Bay Area Environmental Research Institute, NASA Ames Research Center, Moffett Field, CA 94035, USA
[8]Department of Atmospheric Science, Colorado State University, Fort Collins, CO, 80523, USA
[9]Cooperative Institute for Research in the Environmental Sciences, University of Colorado, Boulder, CO, 80309, USA
[10]Institute of Geophysics and Meteorology, University of Cologne, 50969 Cologne, Germany
[11]Jet Propulsion Laboratory, California Institute of Technology, Pasadena, CA 91001, USA
[12]NASA Goddard Space Flight Center, Greenbelt, MD 20771, USA

https://doi.org/10.5194/essd-2026-241
Preprint. Discussion started: 24 July 2026

[13]NSF National Center for Atmospheric Research (NCAR), 1850 Table Mesa Dr, Boulder, CO 80305

[14]Department of Meteorology, Naval Postgraduate School, Monterey, CA 93943, USA

[15]ADNET Systems Inc., Bethesda, Maryland

[16]NASA Goddard Institute for Space Studies, New York, NY

[17]Istituto Nazionale di Geofisica e Vulcanologia, 00147 Rome, Italy

[18]Environmental Molecular Sciences Laboratory, Pacific Northwest National Laboratory (PNNL), Richland, WA 99352, USA

[19]Analytical Mechanics Associates, Hampton, VA, 23666

[20]Italian National Agency for New Technologies, Energy and Sustainable Economic Development, Frascati, 00044, Italy

[21]U.S. Naval Research Laboratory, Monterey, CA 93943, USA

[22]Department of Atmospheric Sciences, Rosenstiel School, University of Miami, Miami, FL, 33149, USA

[23]Department for Atmospheric and Climate Research (ATMOS), Stiftelsen NILU (former Norwegian Institute for Air Research), 2007 Kjeller, Norway

[24]EPFL, Lausanne, Switzerland

[25]School of Meteorology, University of Oklahoma, OK 73072, USA

[26]Solar Radiation Group, University of Valencia, Burjassot, Spain

[27]Environment and Climate Change Canada, Toronto. ON, M3H 5T4, Canada

[28]Autonomic Integra LLC, Bethesea, MD, USA

[29]Department of Geographical Sciences, University of Maryland, College Park, Maryland

[30]Department of Chemistry, University of Michigan, Ann Arbor, MI, 48109, USA.

[31]Aarhus University, Department of Environmental Science, 4000, Roskilde, Denmark

[32]Aerospace Engineering Sciences Department, Colorado Center for Astrodynamics Research, University of Colorado – Boulder, CO, USA

[33]Alfred-Wegener-Institut Helmholtz-Zentrumfu¨rPolar-und Meeresforschung, Bremerhaven,Germany

[34]University of Tromsø: The Arctic University of Norway, Norway

[35]SPEC Incorporated, Boulder, Colorado, USA 80301

[36]Center for Aerosol Science and Engineering, Department of Energy, Environmental and Chemical Engineering, Washington University in St. Louis; St. Louis, MO, 63130, USA

[37]NASA Headquarters, Washington DC, 20546, USA

[38]School of Marine and Atmospheric Sciences, Stony Brook University, Stony Brook, NY 11794, USA

[39]FORTH, Patras, Greece

[40]Terra Research Inc, Hoboken, NJ 07030

[41]Earth System Science Interdisciplinary Center, University of Maryland, College Park, College Park, Maryland

[42]Goddard Earth Sciences Technology and Research (GESTAR) II, University of Maryland-Baltimore County, Baltimore, MD 21250, USA

[43]Cold Regions Research and Engineering Laboratory, U.S. Army Corps of Engineers, Hanover, NH, USA

[44]Thayer School of Engineering, Dartmouth College, Hanover, NH, USA

[45]Department of Earth Sciences, Uppsala University, Uppsala, Sweden

[46]Hampton University, Center for Atmospheric and Planetary Sciences, Hampton, VA, USA

[47]Department of Meteorology and Bolin Centre for Climate Research, Stockholm University, Stockholm, Sweden

https://doi.org/10.5194/essd-2026-241
Preprint. Discussion started: 24 July 2026

[48]Department of Environmental Sciences, Informatics and Statistics, Ca' Foscari University of Venice, Mestre, 30172, Italy
[49]Italian National Agency for New Technologies, Energy and Sustainable Economic Development, Rome, 00123, Italy
[50]Institute for Meteorology, Leipzig University, 04103 Leipzig, Germany
[51]Science Systems and Applications, Inc., Lanham, MD, USA
*Now at: Urban Sky, Denver, CO 80216
**Now at: Space Science and Engineering Center, University of Wisconsin-Madison, Madison, WI 53706, USA
*** Now at: NSF National Center for Atmospheric Research (NCAR), 1850 Table Mesa Dr, Boulder, CO 80305

Correspondence to: Patrick C. Taylor (patrick.c.taylor@nasa.gov)

https://doi.org/10.5194/essd-2026-241
Preprint. Discussion started: 24 July 2026

Open Access Earth System Science Data Discussions

Abstract. The NASA airborne Arctic Radiation-Cloud-aerosol-Surface-Interaction Experiment (ARCSIX) collected a unique data set providing a near-simultaneous characterization of radiative fluxes, surface, cloud, and aerosol particle properties to address science questions on the surface radiation budget, the processes governing the cloud lifecycle, atmospheric composition, and the interactions between the surface and atmosphere. The overarching goal of ARCSIX was to quantify the contributions of surface, clouds, aerosol particles, and precipitation to summer sea ice melt. ARCSIX consisted of two deployments in 2024 (Spring: 2024-05-28 through 2024-06-13 and Summer: 2024-07-25 through 2024-08-15) to capture pre- and post-melt conditions. ARCSIX provided coordinated remote sensing and *in situ* sampling using three aircraft in a high-flyer/low-flyer configuration. The NASA G-III served as the high-flying remote sensing platform with two lower flying *in situ* and near-target remote sensor observing platforms, NASA P-3B and SPEC Inc. Learjet. ARCSIX data are well-suited to improve satellite remote sensing capabilities in the Arctic. ARCSIX included an array of sea ice mass balance buoys deployed in the Lincoln Sea that were regularly overflown during the campaign. ARCSIX research flights spanned the Baffin Bay, Lincoln Sea, west and north of the Canadian Archipelago, and the Greenland north and northeast coasts. During the spring deployment, 19 research flights took place covering 114 flight hours: 10 flights and 68 hours by the P-3B and nine flights and 46 hours by the G-III. During summer, 24 research flights covered 136 flight hours: nine flights and 75 hours by the P-3B, five flights and 26 hours by the G-III, and 10 flights and 35 hours by the Learjet. A total of 13 coordinated flights with 2+ aircraft were carried out. This paper describes the ARCSIX flight strategy, instrumentation, and data set access, and usage details. ARCSIX data are publicly available at https://doi.org/10.5067/SUBORBITAL/ARCSIX/DATA001.

1 Introduction

The Arctic climate system is characterized by high variability and rapid, widespread change. Recent studies indicate that warming in the Arctic has outpaced the global average by up to four times since 1979 (Lenssen et al. 2019; IPCC 2021; Rantanen et al. 2022; Taylor et al. 2022; Wendisch et al., 2023a). This rapid warming has been accompanied by substantial changes throughout the Arctic system including: reductions in sea ice area, thickness, and volume and a shift from a predominantly multiyear to a seasonal ice pack (Kwok 2018; Stroeve and Notz 2018), reductions in Arctic Ocean surface albedo (Duncan et al. 2020); earlier sea ice melt (Markus et al. 2009; Bliss et al. 2023); melt of mountain glaciers and the Greenland Ice Sheet contributing to global sea level rise (Box et al. 2022); transformation of the land regions from tundra grasses to shrubs (Pearson et al. 2013); thawing of permafrost (Smith et al. 2022); reduced snow cover providing new sources of atmospheric dust (Groot Zwaaftink et al. 2016); increases in frequency and intensity of Arctic wildfires (McCarty et al. 2021); and changes in Arctic Ocean physical (salinity, temperature, and stratification) and biological properties (Polyakov et al. 2013; Meier et al. 2014; IPCC 2021). The increase in human activity in the region and a growing appreciation of the influence of Arctic surface conditions on northern hemisphere weather forecasting are driving an increased demand for comprehensive datasets to help improve Arctic forecast systems. Historically, high quality Arctic data have been scarce due to challenges of *in situ* data collection and uncertainties in traditional space-borne observations of Arctic surface and lower atmospheric properties. Although it is obvious that the Arctic is rapidly changing, less clear are the rate and details of future change. Will the future rate of change in key Arctic system properties remain steady or change? Addressing this requires an improved understanding of the Arctic surface-atmosphere interaction processes that contribute most strongly to the observed changes and represent a gap in current environmental observations and prediction capabilities (Taylor et al. 2022a; Boisvert et al. 2022).

Surface-atmosphere interaction is a collection of multi-way processes between sea ice, atmospheric thermodynamics, clouds, aerosols, and radiation that unfold simultaneously and continuously. For example, the surface albedo feedback represents

https://doi.org/10.5194/essd-2026-241
Preprint. Discussion started: 24 July 2026

a sea ice-radiation interaction whereby radiation-induced snow and ice melt darkens the albedo and accelerates melt. Clouds influence the rate of the surface albedo reduction by altering surface insolation, while the surface albedo change modulates the net cloud radiative effect on the surface (Sledd and L'Ecuyer 2019; Alkama et al. 2020). The sea ice insulation feedback is a surface-atmosphere interaction process operating through a turbulent flux response to sea ice concentration that influences the lower atmospheric temperature and humidity structure with the potential to feed back on clouds and radiation (Boisvert et al. 2022; Boeke et al. 2021). In concert, sea ice concentration influences the emission of particles and gaseous pre-cursors from the ocean that influence radiative fluxes directly and indirectly by altering cloud and surface optical properties (Abbatt et al. 2019). Interwoven is the Arctic low-cloud lifecycle that is influenced by internal cloud processes (e.g., primary and secondary ice formation processes, riming, drizzle formation, etc.) and interactions with the external environment influenced including by aerosol, sea ice, and atmospheric dynamic and thermodynamic conditions (Morrison et al. 2012; Tan et al. 2023). Unravelling the physics of these multi-way interactions and improving our understanding of their influence on the sea ice evolution requires collocated data of cloud microphysics, aerosol properties, surface properties, and radiative fluxes; this is the motivation for the NASA Arctic Radiation-Cloud-aerosol-Sea ice Interaction eXperiment (ARCSIX).ARCSIX was conducted in two field deployments in Pituffik, Greenland from 2024-05-28 through 2024-06-13 and 2024-07-25 through 2024-08-15, comprising three aircraft, and the most comprehensive dataset ever collected in the Arctic. The NASA ARCSIX dataset provided the necessary collocated measurements to assess *the contributions of surface properties, clouds, aerosol particles, and precipitation to the Arctic summer surface radiation budget to sea ice evolution.* Another key motivation for these measurements is their potential to improve the interpretation of satellite remote sensing data of the Arctic. The ARCSIX dataset described herein enables novel investigations of the form and function of surface-atmosphere coupling processes within the Arctic system.

ARCSIX adds to the scarce inventory of airborne datasets in the region north of Greenland that can be used to better understand the co-evolution of the Arctic surface-atmosphere interactions. PAMARCMiP (Polar Airborne Measurements and Arctic Regional Climate Model Simulation Project; Wendisch et al. 2023a) campaigns in 2009, 2012, and 2018 included flights over the Lincoln Sea measuring sea ice thickness and atmospheric and cloud properties. The NETCARE (Network on Climate and Aerosols: Addressing Key Uncertainties in Remote Canadian Environments; Abbatt et al. 2019) project also conducted airborne aerosol and cloud measurements over the same region in 2014-07 and 2015-04. More recently, the CHACHA (CHemistry in the Arctic: Clouds, Halogens, and Aerosols; Fuentes et al. 2025) airborne campaign occurred in 2022-02 through 2022-04 based in Utqiaġvik, Alaska and provided cloud, aerosol, and reactive gas measurements, with flights focused on sea ice lead induced cloud formation in the Chukchi Sea that informed flights over the North Water Polynya in the Baffin Bay during ARCSIX. The 2004 Mixed-Phase Arctic Cloud Experiment (M-PACE; Verlinde et al. 2007), the 2008 Indirect and Semi-Direct Aerosol Campaign (ISDAC; McFarquhar et al. 2011), and the Arctic Radiation-IceBridge Sea and Ice Experiment (ARISE; Smith et al. 2017) campaigns, also flown in the Alaskan Arctic, and the Arctic Summer Cloud Ocean Study (ASCOS; Tjernström et al. 2014) Oden cruise were vital to the development of hypotheses of the mixed-phase cloud lifecycle that guided ARCSIX sampling strategies. Lastly, the complementary CAESAR (Cold Air outbreak Experiment in the Sub-Arctic Region; Zuidema et al. 2026) airborne campaign occurred in 2025-03 in the near-by Nordic Seas and captured mixed-phase cloud evolution in the convective, cold air outbreak regime that was not captured during ARCSIX. These campaigns listed here are most relevant to ARCSIX and this list is not meant to be exhaustive.

https://doi.org/10.5194/essd-2026-241
Preprint. Discussion started: 24 July 2026

Open Access Earth System Science Data Discussions

The goal of this article is to provide a reference for users of the data collected, processed and disseminated by the ARCSIX mission. The paper also provides background on the science objectives, flight strategies, flight details, platforms, and

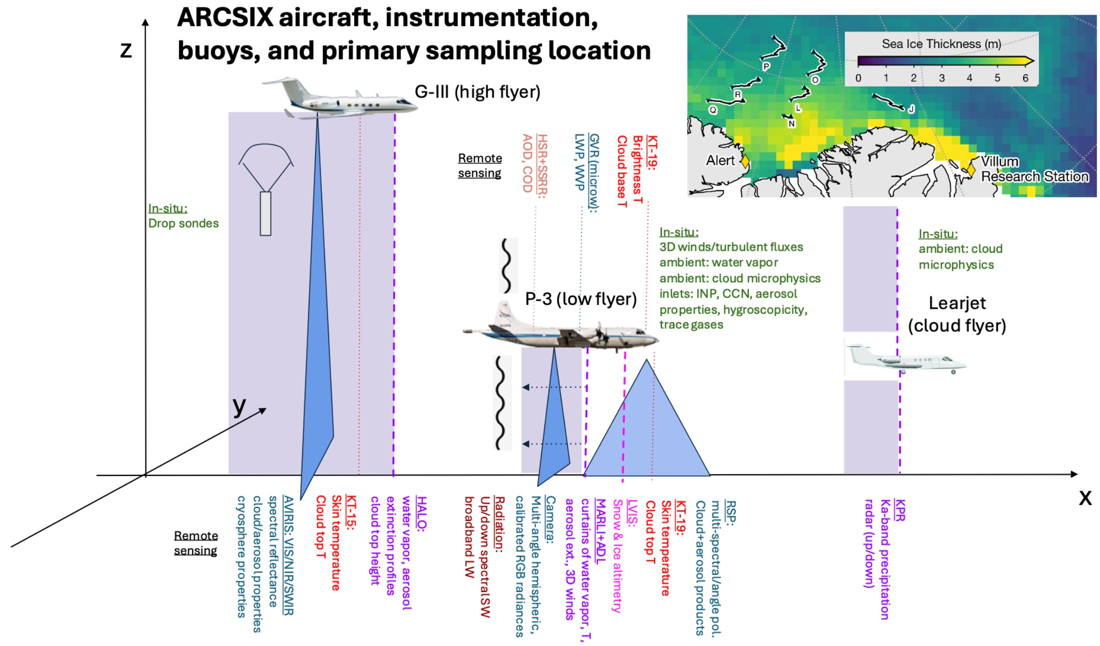

Figure 1: ARCSIX aircraft roles and instrumentation overview with an inset showing the primary flight region and sea ice mass balance buoy drift tracks. Background shows 2024-04 mean gridded sea ice thickness estimates derived from NASA's ICESat-2 (IS2SITMOGR4 version 4, Petty et al., 2025). Instrumentation schematic courtesy of Sebastian Schmidt. Inset courtesy of Vikas Nataraja and Alek Petty. (b) Code available at https://doi.org/10.5281/zenodo.20433891 (Nataraja 2026).

instrumentation of ARCSIX. The campaign carried out 13 coordinated flights with 2+ aircraft (see Section 2). Sections 3, 4, and 5 summarize the airborne instrumentation and associated datasets available from the NASA P-3B, NASA G-III, and Stratton Park Engineering Company (SPEC) Learjet platforms. Sections 6 and 7 describe ground-based instrumentation and ancillary datasets that provide context for the core ARCSIX airborne data sets. Conclusions are provided in Section 8. A forthcoming paper will provide a comprehensive overview of ARCSIX science accomplishments.

2 Campaign Overview

The ARCSIX campaign consisted of two field deployments based at Pituffik Space Base in northwest Greenland: from 2024-05-28 through 2024-06-13 (spring) and 2024-07-25 through 2024-08-15 (summer). These periods bookend the prime sea ice melt season capturing the period of the most rapid sea ice melt. Measurements were collected from three aircraft flown in close coordination employing a low-flyer, high-flyer concept (Fig. 1). The "low-flyer" NASA P-3B (Section 3) acquired *in-situ* aerosol particle, cloud, and atmospheric measurements, along with surface property and radiation observations under clear sky conditions and below, above, and inside cloud layers. The "high-flyer" NASA G-III (Section 4) surveyed surface and

https://doi.org/10.5194/essd-2026-241
Preprint. Discussion started: 24 July 2026

atmospheric properties with remote sensing instruments and dropsondes from ~11 km, providing context for coordinated P-3B and Learjet observations, and serving as a bridge to satellite observations. This approach provides collocated and synchronous *in situ* and remote sensing data to validate satellite remote sensing retrievals and develop next generation approaches. The SPEC Learjet (also a low-flyer/cloud-flyer; Section 5) carried the same suite of cloud microphysical measurements as the P-3B, enabling simultaneous multi-level *in-situ* cloud and aerosol sampling and included a Ka-band cloud radar. The P-3B and G-III platforms flew in both deployments and were joined by the SPEC Learjet in summer. Nine Sea Ice Mass Balance Buoys (SIMBs; Fig. 1; Section 6, Polashenski et al. 2011) were deployed approximately one month before ARCSIX by the University of Dartmouth Cold Regions Research and Engineering Laboratory (CRREL) to track sea ice properties and drift. SIMB drift from installation through 2024-08-25 (or the end of buoy reporting) is depicted in Fig. 1, inset.

Pituffik was an ideal location for ARCSIX as it provided direct access to the last refuge of thick, multi-year Arctic sea ice. The fate of this sea ice is critical to the Arctic region and the globe. The ice pack within the Lincoln Sea, as shown by the SIMB tracks (Fig. 1), generally drifts towards the north coast of Greenland and leads to a thicker, more consolidated ice pack. This general climatological drift pattern was advantageous for ARCSIX as it allowed for the coherent re-sampling of sea ice floes required to quantify the influence of radiative processes on sea ice melt. Capturing a range of surface conditions was also required to address ARCSIX science. Strong gradients in sea ice albedo, thickness, spectral reflectance, and melt pond fractions were expected, and found, off the north coast of Greenland. Also accessible from Pituffik was the northern Fram Strait (a key pathway for mid-latitude air to enter the Arctic and a region of rapid sea ice transport out of the Arctic). In addition, airmasses advected into the ARCSIX domain from the central Arctic, boreal North America, and Eurasia provided opportunities to sample and assess the influence of biomass burning from wildfires on the region.

2.1 Science Questions and Objectives

ARCSIX was organized around three overarching questions that focused on science areas where additional understanding is needed to improve environmental modelling capabilities: namely, radiation, cloud life cycle, sea ice processes, and their interactions. Addressing these questions required simultaneous measurements of the surface-atmosphere system. ARCSIX also included a remote sensing and modelling objective to ensure the data collection strategy aligned with remote sensing and modelling community needs.

- **Science Question 1 (Radiation), SQ1:** What is the impact of the predominant summer Arctic cloud types on the radiative surface energy budget?
- **Science Question 2 (Cloud Lifecycle), SQ2:** What processes control the evolution and maintenance of the predominant cloud regimes in the summertime Arctic?
- **Science Question 3 (Sea Ice), SQ3:** How do the interactions between surface properties and atmospheric forcings affect the sea ice evolution?
- **Remote Sensing and Modelling Objective:** Enhance our long-term space-based monitoring and predictive capabilities of Arctic sea ice, clouds, and aerosols.

Each science question contains sub-questions that informed flight plan design and strategies (see white paper for additional information, https://espo.nasa.gov/ARCSIX_White_Paper). ARCSIX data collection was designed to help constrain cloud and sea ice process models, to evaluate scientific understanding and to improve satellite observing capabilities.

https://doi.org/10.5194/essd-2026-241
Preprint. Discussion started: 24 July 2026

2.2 Data collection principles and flight modules

Addressing ARCSIX science required data to be collected with specific characteristics. Observations need to statistically represent the radiatively important lower-tropospheric cloud systems regardless of their observability from space (*SQ1* and *Remote Sensing and Modelling Objective*). Cloud system measurements must constrain key evolution processes (e.g., water vapor and aerosol sources, aerosol chemical composition, physical properties, distribution relative to clouds and the surface, cloud formation, phase partitioning, and precipitation) to enable the development of forcing data sets to drive cloud and aerosol process models (*SQ2 and SQ3*). ARCSIX data need to resolve the spatial and temporal variability of sea ice properties, including surface albedo and reflectance, thickness, melt pond coverage and size distribution, and its co-evolution with atmospheric conditions through the melt season (*SQ1 and SQ3*). This requirement motivated ARCSIX to resample the same sea ice floes. Lastly, coordinated aircraft flight plans (i.e., near-simultaneous measurements of the same cloud using remote sensing from above while obtaining *in-situ* measurements) enable the evaluation and development of spaceborne cloud and aerosol remote sensing (*Remote Sensing and Modelling Objective*). This requirement led ARCSIX to prioritize the collocation of high-flying and low-flying aircraft in space and time. These key science-driven data collection requirements drove the construction of predefined flight modules. In the description of the flight modules below, instruments and aircraft inlets are mentioned that present constraints on the flight module designs but are incompletely described. Complete descriptions of all platforms and instrumentation are provided in Sections 3-6.

2.2.1 Square Spiral

A spiral maneuver (Fig. 2a) involves the continuous turning at a fixed bank angle, nominally ~15° for ARCSIX, while changing altitude by ~1000 ft per minute. This maneuver has conventionally been used to obtain vertical profiles of aerosol and radiation quantities (Cochrane et al., 2019). However, many instruments, most notably radiation and cloud microphysical

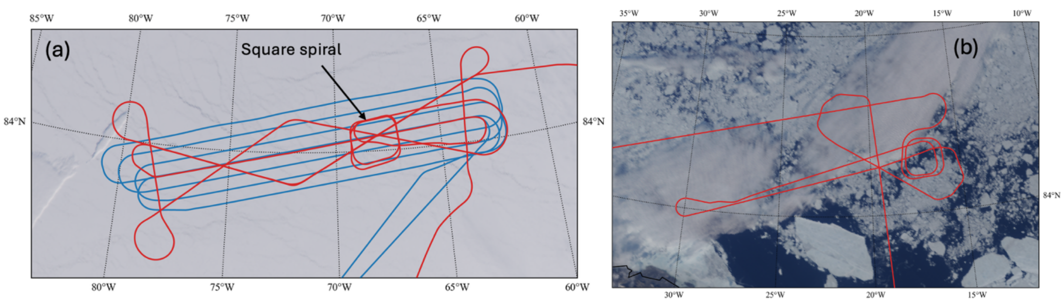

Figure 2: Example flight tracks executed for surface bi-directional reflectance distribution function (BRDF) characterization: (a) 31 May 2024 (RF3) "bowling alley" flight tracks (P-3B in red and G-III in blue) plotted on top of an Aqua MODIS RGB at 1530 UTC (granule date 2024152.1530) and (b) 1 August 2024 (RF14) "bow tie" maneuver by the P-3B plotted on top of a Terra MODIS RGB at 1430 UTC ~10 minutes after entering the maneuver (granule date: 2024214.1430). Courtesy of Kerry Meyer code available from Meyer (2026).

sensors, make their most reliable measurements when the aircraft is flying straight and level. ARCSIX adopted a square spiral that has been used in previous campaigns (Redemann et al. 2021). In the square spiral maneuver, continuous turning is replaced with intermittent descending turns separated by ~1-minute straight and level legs. This enables the collection of radiation and other data while also obtaining the vertical profile of in situ measurements. Square spirals were executed on most flights.

https://doi.org/10.5194/essd-2026-241
Preprint. Discussion started: 24 July 2026

2.2.2 "Bowling alley" and "bowtie" patterns

A dedicated pattern was devised to collect data to develop generalized models of the bidirectional reflectance distribution function (BRDF) for sea ice (Fig. 2a). Data collected during these patterns support studies of the surface radiative properties and the development of an operational sea ice BRDF product for passive satellite imagers to improve retrievals over sea ice.

The BRDF "bowling alley" flight module was executed under clear-sky conditions as joint P-3B/G-III flight maneuvers and received its moniker from the parallel flight tracks (Fig. 2). In the module, the G-III flies a raster pattern at ~11 km to map the spectral surface reflectance and secondarily provide lidar curtains of the aerosol and water vapor structure. The raster pattern resembles the planks of a "bowling alley" lane, within which the P-3B performed its maneuvers, appearing to "bumper bowl" by bouncing off the "gutter bumpers" of the G-III lane. The P-3B's crisscrossing pattern starts at high-altitude (~6 km, selected for surface characterization) and is repeated at low-level (~90 m to 1 km). The pattern provides multi-angular measurements of the crossing points such that the Research Scanning Polarimeter (RSP; Section 3.2.2) multi-angle measurements combined with the Airborne Visible Infrared Imaging Spectrometer - Next Generation (AVIRIS-NG; Section 4.3) hyperspectral mapping provide data needed for sea ice BRDF development. The transition from high to low altitude is performed as a box spiral over one of the crossing points, providing flux divergence, surface albedo scale dependence information, and a vertical profile of aerosols. The low-level portion of the bowling alley provided minimum altitude (~90 m) views of the surface for albedo characterization. These low-level legs also provide *in-situ* measurements of the near-surface aerosol distribution and properties. The flight pattern was executed over a range of surface types: dry snow, partial sea ice coverage, and ponded sea ice.

The inconsistent availability of the G-III during the summer deployment required an adjustment to the BRDF pattern, simplifying the pattern to a "bow-tie" (Fig. 2b) that provided three crossings of a single point. The bowtie consisted of three straight lines (length ~20-25 km) over a single point and was executed by performing two 270° left turns. The bowtie was flown at variable altitudes between 300 and 760 m, selected by the flight scientist. When the G-III was available during summer, the bow tie pattern was retained (e.g., Research Flight (RF19)). In summer, the number of P-3B high-level legs was reduced to collect passes of the low-level centerline at multiple altitudes. This adjustment allows for the assessment of the spatial heterogeneity and scale-dependence of surface albedo to support remote sensing and surface radiation budget science goals. Versions of this flight pattern were executed during two spring flights and six summer flights.

2.2.3 Cloud Walls

A dedicated multi-aircraft sampling pattern, referred to as the "cloud wall", was developed to sample the cloud system and its surrounding environment. The cloud wall sampling pattern includes *in situ* and remote sensing observations with the goal of understanding microphysical and dynamical processes that influence the Arctic cloud lifecycle and surface cloud radiative effects. The cloud wall was flow within cloud systems with at least a 100 km horizontal extent within a consistent meteorological regime. The P-3B characterized a region spanning a ~100 km flight track with the faster G-III extending its flight legs to survey the broader area. The G-III released dropsondes on the edges and within the domain to

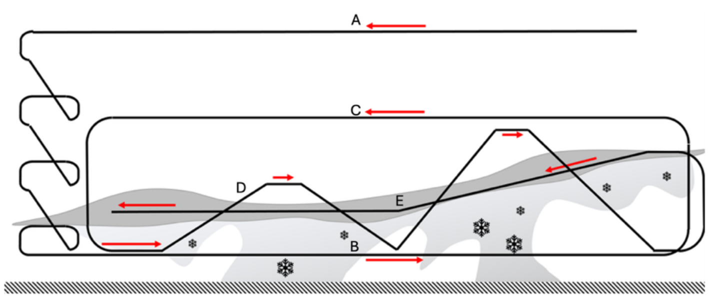

Figure 3: Schematic of the cloud wall pattern: A-high altitude overflight, B-below cloud leg (~90 m), C-above cloud leg, D-cloud porpoise leg, and E-in-cloud leg. Not all cloud walls are flown sequentially from A-E. The order varied based on logistical constraints and the maximization of aircraft coordination.

constrain the large-scale atmospheric conditions for cloud process modeling. The axis of each wall was typically flown perpendicular to the prevailing low-level flow, to maximize the statistical sampling of the cloud system. Aircraft were collocated along the walls (preferably in the same direction of flight) to provide *in situ* microphysical datasets to validate and improve remote sensing retrievals. In summer, the addition of the Learjet provided the unique ability to perform coordinated sampling with three aircraft, further enriching the quality of the dataset and offering new avenues for constraining aerosol-cloud interactions, cloud-surface interactions, and radiative processes.

The P-3B cloud wall observations (Fig. 3, leg A) generally began with an overflight of the cloudy region at high altitude remote sensing survey (~6 km), providing a followed by a square spiral descent, preferably in a clear region nearby the cloud system, to minimum altitude (~90 m). A cloud wall generally consisted of four vertically-stacked level legs of at least 10 minutes (minimum of 70 km) in length. The first two legs (B and C) capture the atmospheric environment (surface, radiation, aerosol, and thermodynamics) below and above the cloud, respectively, and served as a reconnaissance for the third and fourth legs that involved *in-situ* sampling of the cloud. These involved a "porpoise" leg with 5 m s^{-1} (1000 ft min^{-1}) slant ascents and descents through the layer (leg D) providing vertical profiles of cloud microphysical and thermodynamic profiles (including inversion characteristics) and a level, in-cloud leg (leg E) with sustained cloud sampling through a counterflow virtual impactor (CVI) inlet (Sect. 3.5.1) to provide properties of the cloud residual particles (i.e. composition of cloud condensation nuclei and ice nucleating particles, Sec. 3.5.6). This default leg order mitigated inlet and probe icing by placing the in-cloud sampling environments at the end of the module. In several cases, the order of legs was adjusted (in real-time) to attain better coordination/collocation between aircraft. For example, in RF2, a P-3B porpoise at the start of a second wall immediately followed a porpoise leg concluding the first wall, allowing the G-III to conduct two overpasses of the P-3B in quick succession at two different locations within the cloud system. Starting 2024-06-06, the porpoise leg strategy was altered to include a 30-second pause (leg D) between direction changes to provide additional above- and below-cloud aerosol sampling.

One or two complete cloud wall patterns were performed per flight. Only one cloud wall was possible for cases with a longer transit to the northeast coast of Greenland near Villum Research Station, a long-term aerosol and meteorological ground sampling site near Station Nord (https://www.villumresearchstation.dk, 81.6°N, 16.7°W; Sect. 6) (e.g., RF10, on 2024-06-13). In this flight, supplementary sampling of all or some wall component legs was implemented sequentially along a survey flight line. In cases of two complete cloud walls, they were placed approximately parallel to each other so that two states of the same cloud system or an anticipated gradient in cloud properties were captured. The spacing of the walls included, where possible, a quasi-Lagrangian scene evolution (Wendisch et al. 2025).

The G-III contributed large-scale thermodynamic, aerosol, and cloud observations to the flight pattern and dropsonde releases. Repeated and coincident overpasses of the P-3B cloud wall legs were standardized, centered on, and typically twice the length of the P-3B cloud wall to accommodate the approximate factor-of-two difference in flight speed. In the ideal implementation, the aircraft had the same direction of travel, and the G-III overflew the P-3B at the wall midpoint. In most cases, the coincidence was generally within 5 minutes for the entire flight leg. Multiple walls were connected by flying a near-perpendicular leg along the spine of the large-scale flow that passed through their midpoints. Dropsondes were generally released at the endpoints of the extended wall legs, and along the axis connecting two cloud walls resulting in both a perimeter and near-field context. For flights where the P-3B performed one cloud wall and an extended survey, the wall coordination was similarly implemented and the survey line included periodic delay modules where the G-III characterized the cross-track variability allowing the aircraft to maintain closer collocation.

The guiding principles of the cloud wall flight pattern were consistent throughout both deployments, but implementation details varied according to the specifics of the cloud and meteorological conditions. Cloud walls were performed during six

https://doi.org/10.5194/essd-2026-241
Preprint. Discussion started: 24 July 2026

coordinated P-3B and G-III flights in the spring campaign, while three of the four multi-aircraft cloud walls sampled during the summer deployment also included the Learjet (RF16, 17, and 18). For these cases, the Learjet exclusively performed porpoise legs (leg D) allowing the P-3B to focus on the level legs (Leg E). The Learjet porpoise legs were like the P-3 with 5 m s^{-1} (1000 ft min^{-1}) slant ascents and descents through the full depth of the cloud layer but did not include a pause at cloud top and base. The shorter range of the Learjet kept these three coordinated flights closer to Pituffik. In total, ARCSIX sampled ~14 total cloud walls (8 in Spring, 6 in Summer) and 13 P-3B/G-III coordinated cloud walls across nine flights (see Section 2c).

2.2.4 Sea ice characterization and evolution: Repeat line sampling

Capturing the key properties and processes that influence sea ice thinning, snow depth change, and melt pond formation is central to ARCSIX science. The principal requirement was to resample the same sea ice floes throughout the deployments on a weekly cadence. This was accomplished by re-flying lines that connected the sea ice buoy array as they drifted while measuring sea ice, radiation, cloud, and aerosol properties. Sea ice surface sampling required long (~200 km), high-altitude (~6 km) level legs in cloud-free or very thin cloud conditions. In several cases long, high-altitude legs were executed at the beginning of flight patterns as a natural extension of the transit legs. Additionally, these legs were included in the BRDF flight plan (Fig. 2). Several sea ice survey flights (e.g., RF1) were executed to provide regional context of the sea ice properties.

2.2.5 Low-level flight legs: aerosol sampling

Low-level sampling of the near-surface atmosphere was necessary for cloud lifecycle and aerosol science. Low-level flight legs were not a dedicated maneuver but integrated within the BRDF and cloud wall flight modules. BRDF flights contained as many as three hours of flight time below ~300m. These low-level legs are used to characterize near-surface aerosols where local sources are expected to have the greatest influence due to the stratification of the often-stable atmosphere. In addition, many low-level legs were executed within the Nares Strait - a region of water and sea ice between northwest Greenland and Ellesmere Island, Canada that experiences high winds due to orographic funneling. These conditions often form a sea-ice-free region called the North Water Polynya at the southern mouth of the Nares Strait close to Pituffik (Monroe et al. 2021). The strong winds within the Nares Strait suggest that the region could serve as a key source region for marine aerosols and surface dust. The ARCSIX dataset contains several Nares Strait legs between the two seasonal deployments. Notably, RF8 was devoted to low-level and cloud sampling over the North Water Polynya in the northern Baffin Bay and adjacent broken sea ice.

2.3 Flight Summary and Weather Conditions

ARCSIX collected a comprehensive set of surface, radiation, cloud, and aerosol measurements over sea ice spanning from the Baffin Bay, Lincoln Sea, west and north of the Canadian Archipelago, and the north and northeast coasts of Greenland. Figure 4 depicts the flight paths for the spring and summer deployments. The research flight hours across all aircraft totalled ~250 (Table 1). During the spring deployment, 19 research flights took place covering 113.5 flight hours: 10 flights and 68.0 hours by the P-3B and nine flights and 45.5 hours by the G-III. During summer, 24 research flights covered 136.25 flight hours: nine flights and 75.0 hours by the P-3B, five flights and 26.0 hours by the G-III, and 10 flights and 35.25 hours by the Learjet. Data were collected during seven transit flights.

Table 1. Summary of flight hours by campaign and aircraft.

	Research Flights (RFs)				RF Hours			Research Flight Dropsondes
	P-3B	G-III	Learjet	Coordinated Flights	P-3B	G-III	Learjet	

https://doi.org/10.5194/essd-2026-241
Preprint. Discussion started: 24 July 2026

Spring (2024-05-28 through 2024-06-13)	10	9	0	9	68.0	45.5	0	78
Summer (2024-07-25 through 2024-08-15)	9	5	10	4	75.0	26.0	35.25	85
Campaign Total	19	14	10	13	143.0	71.5	35.25	163

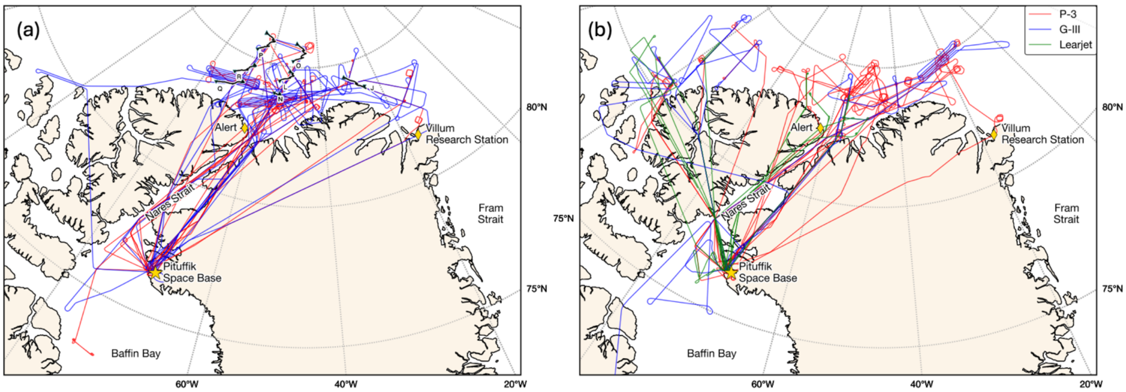

Figure 4: Flight tracks for the (a) Spring Deployment and (b) Summer Deployment are shown. P-3B tracks are in red, G-III in blue, and Learjet in green. Courtesy of Vikas Nataraja. Code available from (Nataraja 2026).

The order of executed flight plans was determined as a balance between weather conditions, campaign objectives, and logistical concerns (e.g., airport opening times, flight crew rest requirements). The balance evolved from leveraging available weather conditions in the beginning of each deployment to a stronger emphasis on addressing missing objectives at the end. Campaign flight plan types clustered weekly due to progress towards objectives and the variability in weather conditions. Tables S1 and S2 provide a summary of each flight for the spring and summer deployments, respectively, including the objective, region, take-off and landing times, the number of dropsondes, and special notes. Movies of the campaign flight tracks are available on the campaign story map (https://www.earthdata.nasa.gov/learn/gis/storymaps/introduction-nasas-arcsix-campaign; Last accessed 2026-07-20).

2.3.1 Meteorology and Flight Summary

The spring deployment began after the passage of an Arctic cyclone across the Lincoln Sea, which resulted in a thinning of the cloud layer, low predicted AODs (< 0.1) from the NASA Goddard Earth Observing System forward processing (GEOS-FP, see Section 7d) model, and decreasing relative humidity at mid-levels (500-700 hPa) over the snow-covered buoy region. The spring deployment flights began with a focus on capturing the initial sea ice conditions and dry snow surface properties (RF1 and RF3; Table 2). In subsequent weeks, the ARCSIX flight domain was largely dominated by a high pressure system located north or northwest of Greenland. These conditions supported several cloud and aerosol focused flights during the second and third weeks of the spring deployment (RF4, 6, 7, 9, and 10; Table S1). The Lincoln Sea experienced warming due to large-scale subsidence as a result, and relatively calm winds near the surface allowing for Lagrangian cloud sampling in early June (RF6

https://doi.org/10.5194/essd-2026-241
Preprint. Discussion started: 24 July 2026

and RF7). Northeasterly winds transported air mass from the Lincoln Sea into the northern Baffin Bay through the Nares Strait during much of the spring deployment, until the flow reversed direction (from Baffin Bay into Lincoln Sea) by the last spring research flight (RF10) in mid-June. Melt onset began north of Greenland around 2024-06-11 coinciding with RF09.

The meteorological conditions of the summer deployment differed significantly from those of the spring deployment. In contrast to the long-lived high pressure system north of Greenland, the large-scale weather pattern in the summer was characterized by a series of transient low pressure systems which traversed across Greenland and the Arctic Ocean. These cyclones were typically associated with complex, multi-layered clouds and frontal precipitating bands, but with relatively quiescent conditions in their cold sector. Cloud-free areas often developed in the vicinity of these systems, allowing for clear-sky BRDF sampling over these regions (RF12, RF13, RF14, RF15; Table S2). Highly variable surface weather at Pituffik posed operational challenges during the summer deployment. Around the transient Arctic cyclones several cases of low clouds were sampled (RF 16,17, 18; Table S2). These cloud cases were generally more complex than in the spring. A more detailed description of the synoptic-scale meteorological conditions during each research flight is provided in the Supplementary Information.

2.4 Summary and Special flight details

A few special comments that influenced execution:

- ARCSIX was a three-aircraft campaign; however, maintenance challenges occurred with the Learjet in spring and the G-III during the summer. The result was four research flight days with all three aircraft between 2024-08-07 and 2024-08-15.
- Individual instrument calibrations occurred throughout flights, generally during high-altitude transits and just before landing. LVIS calibration maneuvers necessitated pitching and rolling the aircraft and were generally performed before or after science data collection.
- Instrument sampling from the community aerosol inlets (isokinetic and CVI) were 'zeroed' during high-altitude transits to verify leak-free sampling.
- The G-III experienced maintenance issues diverting during the transit flight returning to Langley. The G-III was unavailable during the first two weeks of the summer deployment. An effort was made to use the P-3B to minimize the impact of the G-III's absence by adding a higher altitude above-cloud leg to gather additional remote sensing data, when possible. At the beginning of the summer deployment, the radiation and surface characterization objectives were prioritized as they were less impacted by G-III's absence.
- In the summer, ARCSIX coordinated several other campaigns including the Polar5 aircraft, as part of the Norwegian IceBird campaign, the Icebreaker Oden in the Nares Strait during the North Greenland Earth-Ocean-Ecosystem Observatory (GEOEO) (GEOEO 2025) campaign, and the CleanCloud CLAVIER field campaign at based at Villum.
- Several satellite underflights occurred in summer including of NASA's Ice, Cloud, and land Elevation Satellite-2 (ICESat-2) on RF15, the Polar Radiant Energy in the Far InfraRed Experiment (PREFIRE; L'Ecuyer et al., 2021) satellite GRF-11, and underflights of NASA's Plankton, Aerosol, Cloud, ocean Ecosystem (PACE) satellite over Canada and of the European Space Agency's Earth Cloud Aerosol and Radiation Explorer (EarthCARE) satellite during the transit home.
- During the summer deployment, a rare low sea ice concentration anomaly occurred off the northeastern coast of Greenland. Several research flights were focused on sampling the sea ice evolution associated with this event. Additionally, one of the deployed SIMBs (Buoy J) melted out during the event. A manuscript on this event is in preparation.
- Because of the stability of the Arctic atmosphere, aircraft exhaust was occasionally sampled during turns.
- Data taken during transit flight is considered of science quality and appropriate for analysis.

https://doi.org/10.5194/essd-2026-241
Preprint. Discussion started: 24 July 2026

3 P-3B Instrumentation and Datasets

The NASA P-3B Orion included a comprehensive instrument suite to characterize atmospheric state, radiation, surface properties, trace gases, aerosols, and clouds. This included a blend of *in-situ* and remote sensing instrumentation described in detail below and summarized in Fig. 5 and Table 2 with associated measurement details (resolutions, uncertainties) and references for instruments and data products. Research flights were generally 6-8 hours long, typically between 0.15 and 6 km altitude, and generally in coordination with the higher-flying G-III aircraft described in Section 4. Occasionally, the P-3B was able to sample down to 90 m altitude and up to 7.8 km targeting surface emissions and stratospheric intrusions, respectively.

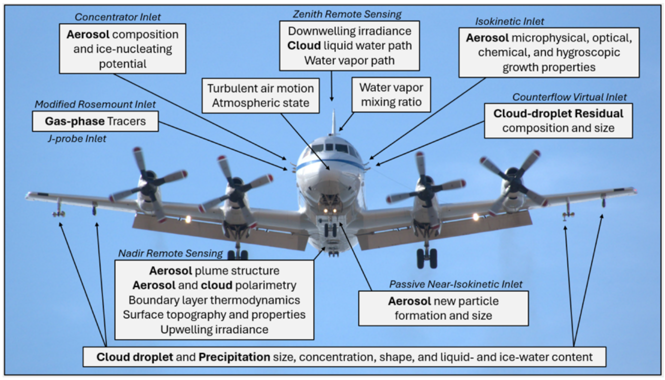

Figure 5: P-3B instrumentation configuration. Courtesy of Luke Ziemba.

Table 2: Summary of P-3B instrumentation and measurements. Inlet column species if an instrument samples from a single inlet or is manually switched between multiple inlets: Isokinetic Clarke (ISO), Counterflow Virtual Impactor (CVI), Concentrator (Conc), and Passive Isokinetic Compensation (PIC).

Instrument	Measured Parameter	Uncertainty	Size Range (µm)	Time Resolution (s)	Inlet	Reference/Notes
Navigation and State Variables						
Northrop Grumman Litton 251 EGI, UNS-1Fw Flight Management System, Sperry Aircraft Data Computer	Latitude, Longitude	~5 m SEP; 0.01°	N/A	1	N/A	
	Altitude (radar, pressure, GPS)	(+/-) 20 feet, baro correction disabled.	N/A	1	N/A	
	Ground and Vertical Speed, Mach Number, Solar Reflectance Angles	0.1 ms-1; 0.01M	N/A	1	N/A	
	Angles (Track, Drift, Pitch, Roll)	0.01°	N/A	1	N/A	
Northrop Grumman Litton 251 EGI & Avionics Rosemount 102 Sensor	Horizontal Wind Speed and Direction	~ 1 ms-1; 10°	N/A	1	N/A	
	Total Air Temperature	0.3-0.5° C	N/A	1	N/A	
Heitronics KT-19.85II Thermometer	Infrared Surface and Cloud Top Temperature	0.5° C + function of ambient T	N/A	1	N/A	Haggerty et al., 2003
Edgetech Vigilant Hygrometer	Dew Point Temperature	0.5° C	N/A	1	N/A	
5-port pressure system (TAMMS)	3-D Winds	w: 10 cm/s; u,v: 50 cm/s	N/A	0.05	N/A	Thornhill et al., 2003
TAMMS Static Temperature	Temperature	0.2° C	N/A	0.25	N/A	Thornhill et al., 2003
TAMMS Static Pressure	Pressure	0.25 mb	N/A	0.016	N/A	Thornhill et al., 2003
Diode Laser Hygrometer (DLH)	Water Vapor	5% or 0.1 ppmv	N/A	<0.05	N/A	Diskin et al., 2002
DLH, TAMMS	Relative Humidity with respect to liquid and ice (derived variable)	10%	N/A	<0.05	N/A	Diskin et al., 2002; Thornhill et al., 2003

https://doi.org/10.5194/essd-2026-241
Preprint. Discussion started: 24 July 2026

Multi-functional Airborne Raman Lidar (MARLi)	Vertical profiles of water vapor, temperature, lidar scattering ratio (LSR), depolarization ratio	Calibration: water vapor, 5%; T. 1 K	N/A	~1-20	N/A	Liu et al. 2014; Wu et al. 2016
5-Beam Airborne Doppler Radar (ADL)	Vertical profiles of reflectivity and radial velocity	0.4 m/s	N/A	1	N/A	
Radiation						
Solar Spectral Flux Radiometer (SSFR)	Spectral Solar irradiance: downwelling and upwelling	5%	N/A		N/A	Schmidt and Pilewskie, 2012
Hyperspectral Radiometer (HSR1 or SPN-S)	Diffuse and total irradiance: downwelling	7%	N/A		N/A	Norgren et al., 2022
Solar Spectral Radiance Radiometer (SSRR)	Radiance	5%	N/A		N/A	
Wide-Field Of View (FOV) Camera	Radiance	5%	N/A		N/A	
Modified Kipp & Zonen CM-22 pyranometers	Broadband solar irradiance: downwelling and upwelling	3%	N/A		N/A	Bucholtz et al., 2010
Modified Kipp&Zonen CG-4 pyrgeometers	Broadband IR irradiance: downwelling and upwelling	3%	N/A		N/A	Bucholtz et al., 2010
Dynamax SPN1 Total/Diffuse Solar Radiometer	Diffuse and global broadband shortwave irradiance: downwelling	5%	N/A		N/A	Badosa et al., 2014
KT19.85 II IR Pryometer	Temperature	+/- 0.5 °C	N/A		N/A	
Surface Properties						
Land, Vegetation, and Ice Sensor Facility Lidar (LVIS-F)	L1B Geolocated Return Energy Waveforms, L2 Geolocated Surface Elevation and Canopy Height	+/- 0.1m	N/A		N/A	
LVIS Cameras: PhaseOne 150 MP, Canon 20 MP, Canon 50 MP (values in column 3 represent cross-track width, along-track distance, and pixel size, respectively)	Camera Imagery	PhaseOne 150 MP (1780m, 324m, 0.13m^2), Canon 20 MP (Spring, 6428m, 4285m, 1.15m^2), Canon 50 MP (Summer, 6428m, 4285m, 0.74m^2)	N/A	~1-3	N/A	
Trace Gases						
Picarro model G2401-m	CO, CO_2, CH_4	5 ppb (CO)	N/A	2.5	Modified Rosemount TAT	DiGangi et al., 2021
		0.1 ppm (CO_2)		2.5	Modified Rosemount TAT	
		1 ppb (CH_4)		2.5	Modified Rosemount TAT	
2B Tech. Inc. model 205	O_3	greater of +/-5 ppbv or +/-5%	N/A	2	Forward J-probe	Wei et al., 2021
Aerosols						
Brechtel Mfg. Inc. Counterflow Virtual Impactor vs. Isokinetic Inlet	Inlet Flag	NA	NA	1	Iso/CVI	
TSI-3772 CPC	Particle Concentration	10%	0.01 - 5	1	Iso	Moore et al., 2017

https://doi.org/10.5194/essd-2026-241
Preprint. Discussion started: 24 July 2026

TSI-3772 with Thermal Denuder (350° C)	Nonvolatile (350°C) Particle Concentration	10%	0.01 - 5	1	Iso	Moore et al., 2017
TSI-3321 Aerodynamic Particle Sizer (APS)	Aerosol Size Distributions	20%	0.5-5.7	1	Iso	McNaughton et al., 2007
Nuclei-Mode Aerosol Size Spectrometer (NMASS)	Number size distribution (cut size diameters of 3, 5, 10, 21, 31 nm)	0.2	0.003 - 0.06	1	PIC	Williamson et al., 2018
Ultra-High Sensitivity Aerosol Spectrometer (UHSAS)	Number size distribution	0.2	0.06 - 1	1	PIC	Kupc et al., 2018
Printed Optical Particle Spectrometer (POPS)	Number size distribution	0.2	0.14 - 3	1	PIC	Gao et al., 2016
Fast Integrated Mobility Spectrometer (FIMS)	Number size distributions	20%	0.01-0.5	1	Iso/CVI	Wang et al., 2017, 2018
Aerodyne HR-ToF-AMS	Non-refractory Chemically Resolved Mass Concentration	<50%	0.06-0.6	25	Iso/CVI	DeCarlo et al., 2008
Aircraft Aerosol Time-of-Flight Mass Spectrometer (A-ATOFMS)	Chemically resolved number fractions of six chemically distinct particle types	Number fraction standard error	0.09-2.0	300	Iso/CVI/Conc	Pratt et al., 2009
TSI-3563 Nephelometer	Dry Scattering Coefficient (450, 550, and 700 nm)	1 Mm^{-1}, 20%	<5 and <1 (with cyclone)	1	Iso	Ziemba et al., 2013
TSI-3563 Nephelometer with 80% humidification	f(RH) for Scattering (450, 550, and 700 nm)	10%	<1	1	Iso	Ziemba et al., 2013
Radiance Research Particle Soot Absorption Photometer (PSAP)	Aerosol Absorption (467, 530, and 660 nm)	0.5 Mm^{-1} near surface and 2 Mm^{-1} at high altitude, 15%	<5	1	Iso	Mason et al., 2018
DMT Inc. Single Particle Soot Photometer (SP2)	Refractory black carbon (BC) mass concentrations	20%	0.09-0.3	1	Iso/CVI	Schwarz et al., 2006
DMT Cloud Condensation Nuclei (CCN) spectrometer	CCN Concentration and Spectra	10% for CCN, ±0.04 for supersaturation	<5	1	Iso	Moore et al., 2009
Brechtel Mfg. Inc. Differential Aerosol Sizing and Hygroscopicity Spectrometer Probe (DASH-SP)	Size-resolved hygroscopic growth factor	0.045 (0.8% RH)	0.17-1.0	Dependent on particle concentration (median ~30 s)	Iso/CVI	Shingler et al., 2016b
Brechtel Mfg. Inc. Differential Aerosol Sizing and Hygroscopicity Spectrometer Probe (DASH-SP)	Size-resolved real part of refractive index	0.02	0.17-1.0	Dependent on particle concentration (median ~30 s)	Iso/CVI	Shingler et al., 2016b
Ice Spectrometer	Offline Ice nuclei number concentration reported per standard liter of air (1013.5 mb, 0 deg C)	90% confidence intervals reported	< ~6 µm		Iso/Conc	McCluskey et al., 2018
Continuous Flow Diffusion Chamber 1H (CFDC-1H)	Online Ice nucleating particle concentrations reported per standard liter of air (100 kPa, 0 degrees C)	90% confidence intervals reported	< 2.5 µm		Iso/CVI/Conc	Rogers et al., 2001; DeMott et al., 2015
			Clouds			
SPEC Inc. Fast 2D-Gray Probe	Number concentration and size distribution, extinction, ice water content, imagery	20%	5-3005 µm	1	N/A	

SPEC Inc. Fast Two Dimensional Stereo (F2D-S) - horizontal arm	Number concentration and size distribution, extinction, ice water content, imagery	20%	5-3005 µm	1	N/A	
SPEC Inc. Fast Two Dimensional Stereo (F2D-S) - vertical arm	Number concentration and size distribution, extinction, ice water content, imagery	20%	5-3005 µm	1	N/A	
SPEC Inc. Fast Cloud Droplet Probe (FCDP)	Number concentration and size distribution, extinction, liquid water content	50%	1.5-50 µm	1	N/A	Knollenberg, 1981; Lawson et al., 2017
SPEC Inc. High Volume Precipitation Spectrometer (HVPS4)	Number concentration and size distribution, extinction, ice water content, imagery	15%	75-45075 µm	1	N/A	Woods et al. (2018)
SPEC Inc. High Volume Precipitation Spectrometer (HVPS4) - horizontal 150µm arm	Number concentration and size distribution, extinction, ice water content, imagery	15%	75-45075µm	1	N/A	Woods et al. (2018)
SPEC Inc. High Volume Precipitation Spectrometer (HVPS4) - vertical 50µm arm	Number concentration and size distribution, extinction, ice water content, imagery	15%	25-15025µm	1	N/A	Woods et al. (2018)
SPEC Inc. High Volume Precipitation Spectrometer (HVPS4) - horizontal 50µm arm	Number concentration and size distribution, extinction, ice water content, imagery	15%	25-15025µm	1	N/A	Woods et al. (2018)
SPEC Inc. Hawkeye Two Dimensional Stereo (2D-S) - horizontal arm	Number concentration and size distribution, extinction, ice water content, imagery	15%	25-15025µm	1	N/A	Lawson et al., 2006; Woods et al., 2018
SPEC Inc. Hawkeye Two Dimensional Stereo (2D-S) - vertical arm	Number concentration and size distribution, extinction, ice water content, imagery	20%	5-3005 µm	1	N/A	Lawson et al., 2006; Woods et al., 2018
SPEC Inc. Hawkeye - CPI imaging component	Imagery	N/A	2.3-2000 µm		N/A	
SPEC Inc. Particle Phase Spectrometer (PPS) - Fast 2D-Gray	Number concentration and size distribution, extinction, ice water content, imagery	20%	2.5-1502.5 µm	1	N/A	
SPEC Inc. Particle Phase Spectrometer (PPS) - CPI imaging component	Imagery	N/A	0.73-800 µm		N/A	
Sky Tech Nevzorov LWC/TWC	Liquid and total water content	0.1 g cm^{-3}			N/A	Korolev et al., 1998
G-Band Vapor Radiometer (GVR; ProSensing)	Liquid water path (LWP) and water vapor path (WVP)	15 g m^{-2}, 0.5 kg m^{-2}	N/A	~6	N/A	Pazmany, 2007; Ephraim et al. 2025
Research Scanning Polarimeter (RSP): †Cross-track by along-track; ‡Non-imaging: along-track product with single cross-track elements	Cloud Top Effective Radius	1 µm/10%	N/A	100 m x 600 m†,‡	N/A	Alexandrov et al., 2012a/b
	Cloud Top Effective Variance	0.05/50%	N/A	100 m x 600 m†,‡	N/A	Alexandrov et al., 2012a/b
	Cloud Mean Effective Radius	20%	N/A	100 m x 600 m†,‡	N/A	Alexandrov et al., 2012a/b
	Cloud Optical Thickness	15%	N/A	100 m x 600 m†,‡	N/A	Nakajima and King, 1990
	Cloud Top Height	15%	N/A	100 m x 600 m†,‡	N/A	Sinclair et al., 2017

https://doi.org/10.5194/essd-2026-241
Preprint. Discussion started: 24 July 2026

Open Access Earth System Science Data Discussions

3.1 Atmospheric State

3.1.1 Meteorology and Navigation data

A UNS-1Fw Flight Management System and Sperry aircraft data computer were used to provide basic meteorological and navigational data including latitude, longitude, altitude, aircraft horizontal and vertical speed, roll/pitch/drift/track angles, solar reflectance angles, and horizontal wind speed and direction (Bennett et al. 2025a). Total air temperature and dew point temperature data were obtained with a Rosemount 102 sensor and Edgetech Vigilant Hygrometer, respectively. A Heitronics KT-19.85II pyrometer measured infrared surface and cloud top temperature. The time resolution of these archived data is 1 Hz. Instruments and data products are summarized in Table 2.

3.1.2 Turbulent Air Motion Measurement System (TAMMS)

The TAMMS obtained high resolution 3-D wind measurements, along with static temperature and pressure with a sampling frequency of 20 Hz (Thornhill et al. 2003; Bennett et al. 2025a). This system has extensive performance heritage on the P-3B and has been used for over two decades in field campaigns. Ambient winds are computed as the difference between the aircraft velocity with respect to the Earth and the air velocity with respect to the aircraft using the full wind equations (Lenschow 1986).

TAMMS data are available for the 19 P-3B research flights. Horizontal wind data are available for all legs; however, vertical winds are only provided for straight and level legs. During the campaign, the non-deiced temperature probe iced over several times and was replaced by the aircraft temperature data. In addition, missing data occurred due to the icing of our radome or pressure transducers. The temperature sensor was calibrated before the start of the mission and the pressure transducer immediately afterwards. Multiple calibrations were done during the mission and the results were added to the database of calibrations from previous calibration maneuvers dating back over 20 years. As a result, current uncertainties in the 3-D winds are +/- 0.25 m s-1 for the horizontal winds, +/- 0.1 ms-1 for the vertical winds and +/- 0.4 °C for the ambient air temperature.

3.1.3 Diode Laser Hygrometer (DLH)

Fast-response measurements (20 Hz) of water vapor were conducted with the DLH open-path near-infrared spectrometer (Diskin et al. 2002). The DLH measures light absorption over the ambient path with its “top hat” transceiver on the P-3B zenith port and the retroreflector on the aircraft tail. DLH takes advantage of three absorption lines with different strengths to measure water vapor from percent levels to below 1 ppmv. Data products from DLH include water vapor mixing ratio, and relative humidity (RH) with respect to liquid and ice (Table 2). The RH products are derived using static temperature and pressure data from the TAMMS.

DLH relies on a clear view between its transceiver and retroreflector, data are less reliable within dense liquid or mixed-phase clouds and when icing occurs. To overcome this limitation, a short path DLH (DLH-SP) was also deployed. The instrument creates an atmospheric optical path between two fins on the exterior of an aircraft window. This shorter path did not have the limitations of the longer path, although it has reduced sensitivity in very dry conditions. The combination of the two DLH measurements allowed for nearly complete data coverage, even during conditions with icing and high cloud optical density. DLH Water vapor mixing ratio data (uncertainty 10%) have been extensively validated and used in previous NASA airborne missions (e.g., Sorooshian et al. 2023).

https://doi.org/10.5194/essd-2026-241
Preprint. Discussion started: 24 July 2026

3.1.4 Multi-functional Airborne Raman Lidar (MARLi)

The MARLi operates with a 355 nm diode-pumped laser providing vertical distributions of water vapor and temperature. The MARLi provides profiles of aerosol/cloud lidar scattering ratio (LSR) and linear depolarization ratio (Liu et al. 2014; Wu et al. 2016; Wang 2025). The vertical resolution of raw MARLi measurements is 0.6 m while the temporal/horizontal resolution is 1-50 Hz depending on flight altitude. Further averaging was done during post-processing to improve signal-to-noise ratio. The archived data have a vertical resolution of 6 m. The horizontal resolution of archived data is chosen to optimize the cloud horizontal structure variations associated with boundary layer circulations. Additional averaging is required for water vapor and temperature measurements to further reduce random noise, especially below 500 m of the flight-level. These high-resolution water vapor and temperature data provide information on boundary layer structure and are used to resolve interactions between clouds and their environment. During ARCSIX, MARLi operated nominally except for RF4 on 3 June due to an aircraft power supply issue that affected multiple instruments.

MARLi retrievals require near-range overlap corrections for temperature, LSR, and depolarization ratio measurements. One correction is applied for an entire research flight for each variable. This approach does not fully account for temporal overlap function changes that occur within the first 200 m of a flight. One water vapor calibration was applied to the entire campaign. *In-situ* temperature measurements are used to correct small temperature drifts associated with cabin temperature variations. Past comparisons with co-located dropsonde measurements showed MARLi water vapor calibration uncertainty is better than 5% and temperature calibration uncertainty is better than 1K. The random errors of MARLi water vapor and temperature measurements increase with range-squared and could be significantly larger than the calibration errors in the current archived version together with clouds. Water vapor and temperature data below and near clouds are prone to larger uncertainties due to a reduced signal-to-noise. Optically thick water clouds attenuate Raman signals within ~200m, and no data should be used beyond this range in the water-dominated cloud layers. Water vapor and temperature data from descending and ascending legs could be biased due to temporal averaging based on data distance from the flight level and vertically changing water vapor and temperature. MARLi data may be biased at times due to high solar background from sea ice that impacts the linearity and calibration of the photomultiplier gain.

3.1.5 Airborne Doppler Lidar (ADL)

The ADL is a five fixed-beam all-fiber coherent Doppler lidar system that measures vertical profiles of aerosol and cloud structures and radial velocities. ARCSIX marked the first deployment of the ADL system and the data are experimental. Due to a laser issue, ADL operated with four beams: nadir on a stabilized platform and three 30-degree off-nadir beams (forward, back, and side). ADL sampled at 1 Hz horizontally with 18-45 m range bin sizes depending on flight level and a ~100m flight level blind-zone. ADL operates at 1.55µm requiring coarse mode aerosols or cloud particles to provide detectable signals. ADL radial velocity measurement accuracy (better than 0.4 m/s) was evaluated based on collocated ground-based Doppler lidar measurements in the U.S. Department of Energy's Atmospheric Radiation Measurement (ARM) User Facility at the Southern Great Plains. During ARCSIX, coarse mode aerosol concentrations were very low. Thus, ADL measurements are limited to cloud layers, near-surface layers during flight legs below 1 km, and some elevated long-range aerosol transport layers.

https://doi.org/10.5194/essd-2026-241
Preprint. Discussion started: 24 July 2026

3.2 Radiation

3.2.1 BroadBand Radiometer Suite (BBR)

The BBR suite provided measurements of upward and downward longwave (thermal-infrared; LW) and shortwave (solar; SW) radiative flux densities (irradiance) from the P-3B. The broadband radiometers deployed were CM22 precision pyranometers (SW) and CG4 pyrgeometers (LW) from Kipp & Zonen that were modified for aircraft use (Kipp and Zonen 2001; Kipp and Zonen 2004; Bucholtz et al. 2010; Bucholtz et al. 2025) and fix-mounted on the top and bottom of the aircraft. Measured upwelling and downwelling broadband irradiances (unit: W m^{-2}) are spectrally integrated over wavelengths from 0.2-3.6 μm and 4.5-42 μm for the SW and LW bands, respectively. Attitude correction was applied to the downwelling SW radiometer data to account for the change of sun-sensor geometry due to aircraft orientation (Long et al. 2010). The SW radiometers were calibrated using the standard alternating sun–shade method (ASTM 2005). The sensitivities for the SW radiometers from pre- and post-mission calibrations agree to within 3%. LW radiometer calibration was performed by comparing to a blackbody immersed in a variable temperature alcohol bath. Pre- and post-mission LW calibration coefficients also agree to within 3%.

The BBR suite included two other instruments mounted on top of the P-3B: a sunshine pyranometer (SPN1) and a KT-19 infrared pyrometer. The SPN1 measures diffuse and total (diffuse plus direct) radiative fluxes (Badosa et al. 2014; Long et al. 2010) with a spectral range of 0.4-2.7 μm and the KT-19 provides sky temperature measurements in the 9.6-11.5 μm interval. SPN1 data provide the direct–diffuse ratio needed for correcting the downwelling SW irradiances for aircraft attitude (Long et al. 2010; Bucholtz et al. 2008). The SPN1 calibration procedure followed manufacturer instructions.

The BBR suite performed well for both phases of the ARCSIX campaign with a few exceptions. During the spring deployment, a poor cable connection resulted in the upward facing solar radiometer data being unusable except for RF9. However, SPN1 data can be used as a back-up. The downward facing solar radiometer data experienced problems on RF8 and RF10. LW flux radiometer and KT19 data performed nominally during the spring. The entire BBR suite experienced no problems during the summer deployment.

3.2.2 Research Scanning Polarimeter (RSP)

The RSP (Cairns et al. 1999) is a passive scanner that provides hyper-angular polarimetric and radiometric observations along the aircraft ground track (roughly within ±55° from nadir) in nine spectral bands: from the visible/near infrared to shortwave infrared (410, 469, 555, 670, 863 and 961 1588, 1884 and 2264nm). Seven bands are in atmospheric windows and are used for remote sensing of clouds (Alexandrov et al. 2012a, 2012b, 2018), aerosols (Waquet et al. 2009; Knobelspiesse et al. 2011; Wu et al. 2016; Stamnes et al. 2018) and to characterize surfaces (Elias et al. 2004; Knobelspiesse et al. 2008; Litvinov et al. 2010, 2011; Ottaviani et al. 2015, 2019). The observations within strong water-absorption bands are used to estimate column water vapor (940 nm) and to detect thin cirrus clouds (1880 nm). Observations of a dark reference and a polarimetric calibrator are made on every scanner rotation to continuously track the calibration state. Considering both RSP1 (deployed on the P-3B during ARCSIX) and its copy (RSP2), >35 field deployments were completed successfully over the last 25 years.

Each datafile corresponds to a straight flight segment. L1B data contain calibrated and geolocated radiances, while L1C collocates the angular views from different scans to the nearest nadir pixel, providing a multi-angle view of the same scene. When a flight pattern such as a “bow tie” is performed, multi-angle observations at different relative solar azimuths of the surface can be used to construct the BRDF or estimate the parameters of a BRDF model. The RSP field of view is 14 mrad so its pixel size varies from 80 m at “high” P-3B altitudes (5.6 km) to 1.4 m at 100 m.

https://doi.org/10.5194/essd-2026-241
Preprint. Discussion started: 24 July 2026

Data are archived for Level 1B/C (radiance) and Level 2 (cloud) products including cloud top effective radius and variance, cloud optical thickness, cloud top height, cloud albedo, extinction cross section and lidar ratio. The L2 cloud data include parametric retrievals of cloud droplet effective radius and variance, estimates of their uncertainty and cloud droplet size distributions estimated using the Rainbow Fourier Transform technique (Alexandrov et al. 2012a, b). Bispectral retrievals of cloud droplet effective radius and optical depth are also made using non-absorbing (864 nm) and absorbing (1589 and 2264 nm) bands (Nakajima and King, 1990) or two absorbing bands (Meyer et al. 2025).

3.2.3 Shortwave Spectral Flux and Radiance Measurement Package

The spectral shortwave radiation measurement package includes four instruments: the Solar Spectral Flux Radiometer (SSFR), the Hyper-Spectral Radiometer (HSR1), the Solar Spectral Radiance Radiometer (SSRR), and a wide field-of-view (WFOV) camera. SSFR (Schmidt et al., 2021) measures downward and upward spectral irradiance from 370-2150 nm – roughly the wavelength range of AVIRIS-NG (Section 4c) and operates with an active levelling platform (ALP; Cochrane et al. 2019).

SSFR measures hemispherically averaged and incidence-angle weighted irradiance (W m^{-2} nm^{-1}) and was radiometrically calibrated in the laboratory before and after ARCSIX and sensor stability was tracked with a portable field standard. . The radiometric accuracy is generally 5%. However, the dedicated Inertial Navigational System (INS) that delivers aircraft attitude (pitch, roll) and heading to ALP malfunctioned briefly after some rapid turns during ARCSIX. This led to imperfect active alignment of the platform by the actuators that was corrected in software and is documented as a data quality flag. During these periods, the zenith accuracy degraded to 7%. SSFR's precision is 0.5% (mid-dynamic range). The accuracy of the derived flight-level albedo is between precision and radiometric accuracy because of partial error cancellation and will be described in future dedicated surface albedo publications.

The HSR1 spectrometer (Norgren et al. 2022) was fix-mounted to the top of the P-3 and measures downwelling irradiance for a part of SSFR's wavelength range (350–900 nm), with a comparable spectral resolution. The radiometric accuracy of HSR1 is 7%, and the precision is 0.5%. HSR1 provides the separation of the total irradiance into its diffuse and direct part, which is important for the angular correction of SSFR and useful for remote sensing of clouds and aerosols. Because HSR1 is fix-mounted, post-flight aircraft attitude correction was performed leading to additional uncertainty. The value of HSR1 for ARCSIX comes mainly from the spectral separation of the downwelling irradiance and should always be used in conjunction with SSFR. The broadband predecessor instrument SPN1 (Section 3b,i) provides further information.

SSRR has similar characteristics as SSFR (370–2150 nm; 6–12 nm resolution; 5% radiometric accuracy; 0.5% precision) but sampled nadir and zenith *radiance* (W m^{-2} nm^{-1} sr^{-1}). This was accomplished by different types of light collectors that were fix-mounted at nadir and zenith and observed pencil-beam radiance with a 3° field-of-view. It spectrally complements RSP (Section 3b,ii) and AVIRIS-NG (Section 4c) on the G-III.

The WFOV camera was mounted on the bottom of the aircraft and provided radiometrically and geometrically calibrated multi-angle reflectance with center wavelengths at three bands in the visible with center wavelengths at 493 nm (blue), 555 nm (green), and 626 nm (red). This was accomplished using a commercially available camera with RGB sensors with overlapping spectral bandpasses (~100 nm wide) that were characterized in the laboratory. The radiometric response was determined using a known standard (integrating sphere) with an accuracy of about 5%. The geometric attributes were determined in the laboratory and with night-sky observations allowing geolocation of pixels up to a viewing zenith angle of ±70º with 0.09° angular resolution. During the spring campaign, only the green channel is available. Where possible, SSFR, SSRR, HSR1, and camera data is complemented with radiative transfer calculations demonstrating accuracy and mutual agreement of the measurements.

https://doi.org/10.5194/essd-2026-241
Preprint. Discussion started: 24 July 2026

SSFR data is used to derive spectral surface albedo, atmospheric absorption (from net flux profiles in spiral ascents or descents), and cloud and aerosol radiative effects. In addition, it can be used to derive the column mixing ratio of trace gases such as ozone. SSRR nadir radiance, in conjunction with SSFR zenith irradiance, provides nadir reflectance, which complements AVIRIS-NG and RSP-derived surface and cloud information. SSFR zenith radiance can be used to retrieve cloud optical thickness and droplet effective radius when under flying clouds, complementing G-Band Vapor Radiometer (GVR) retrievals of LWP (Section 3.4.1). The WFOV camera reflectance data gives nearly horizon-to-horizon coverage of the angular dependence of surface reflectance, but it should only be used in conjunction with sensors with narrower spectral response functions (e.g., RSP, AVIRIS-NG, and SSRR).

3.3 Surface properties: Land Vegetation, and Ice Sensor (LVIS)

The NASA Land, Vegetation, and Ice Sensor (LVIS) was used to characterize sea ice properties and provide surface elevation and freeboard during ARCSIX (Fig. 6). The LVIS-Facility (LVIS-F) suite included a lidar and three downward looking cameras acquiring data in 1-3 second intervals depending on altitude.

LVIS is a wide-swath airborne imaging lidar system that operates a 1064 nm-wavelength laser and three detectors to determine the range and return pulse structure. The sensor provides topographic maps with decimeter accuracy (Table 2) and vertical height and structure measurements over sea ice (Fig. 6c). Routine pitch and roll calibration maneuvers were performed

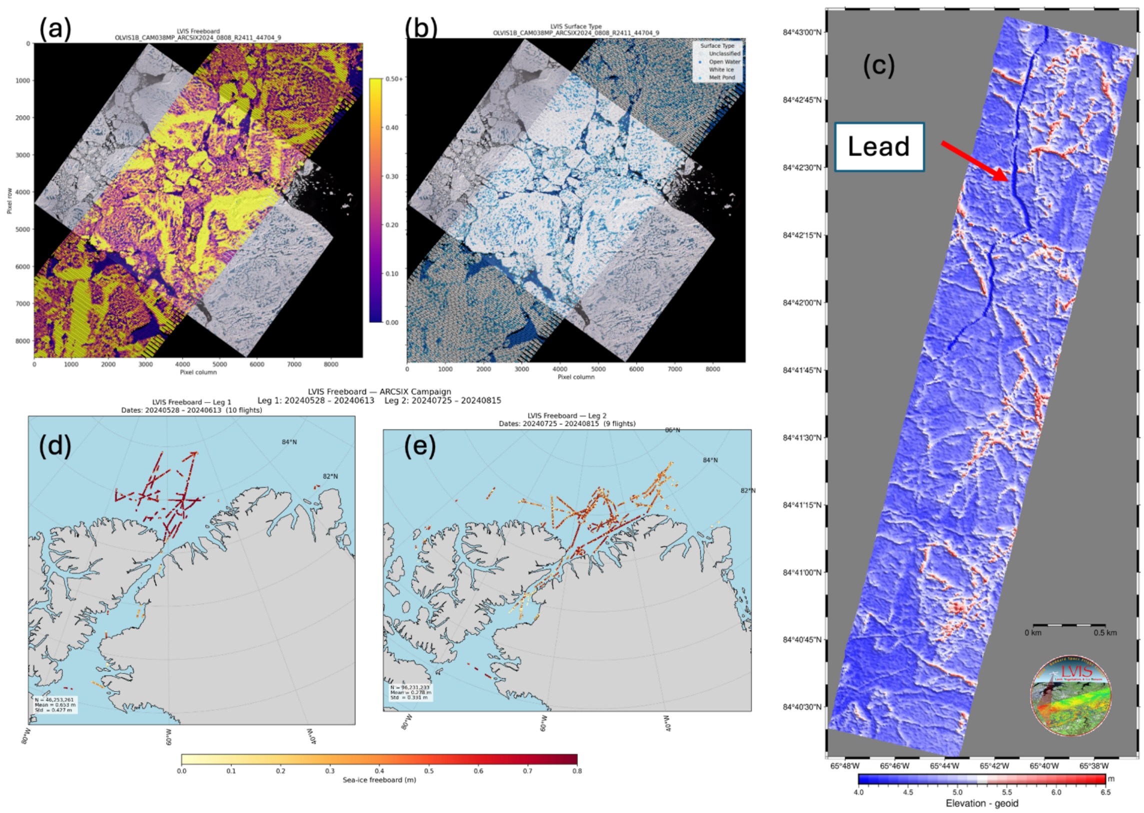

Figure 6: Panels (a) and (b) show an example section of freeboard and surface classifications overlain on the PhaseOne imagery. Panel (c) shows an example LVIS surface elevation retrieval from RF1. Panels (d) and (e) shows cloud screened LVIS derived freeboard retrieval for Spring and Summer deployments, respectively. Figure courtesy of Michelle Hofton and Nathan Kurtz.

https://doi.org/10.5194/essd-2026-241
Preprint. Discussion started: 24 July 2026

several times each flight. The optimal survey altitude for LVIS is 10 km, which results in a 2 km wide swath with 7-10 m footprints. However, ARCSIX operations typically occurred from ~2-6 km, meaning a swath width between 1.2 and 0.6 km. At flight altitudes lower ~1.2 km than optimal, the LVIS scanning rate lags aircraft speed creating gaps in the sampling. LVIS remained operating even at low altitudes - best effort data were collected to as low as 500 m, and data were obtained from as high as 6.0 km altitude. LVIS surface elevation retrievals are degraded or cannot be performed in the presence of clouds; gaps in the flight tracks often indicate the presence of clouds.

The high-resolution camera imagery provides surface type classification for local sea surface and freeboard determination. Three different cameras were deployed during ARCSIX (Table 2). LVIS obtained data on return energy and range to surface that can be used to retrieve sea ice freeboard and thickness. LVIS data are available at lvis.gsfc.nasa.gov/Data/Maps/GN2024Map.html (Blair and Hofton 2020)

Sea ice freeboard is derived from the LVIS surface elevation measurements and visible imagery acquired by the PhaseOne camera system. To ensure consistency with established satellite datasets, geophysical corrections were first removed from the LVIS surface elevation product in a manner equivalent to the ICESat-2 ATL07/10 rel007 data products (Kwok et al. 2025). These corrections include the removal of ocean, load, and pole tides using the pyTMD software (Sutterley et al., 2025), the EUMETSAT OSI SAF Dynamic Atmospheric Correction, and a mean sea surface (Kwok et al. 2020; Kwok and Morison 2016); all corrections are retained on the freeboard data product. PhaseOne camera imagery was classified using the Wright and Polashenski (2018) algorithm, which distinguishes surface types into open water, grey ice, white ice, shadow, and melt pond classes; these classifications are co-located with the LVIS data and retained on the product. Sea ice freeboard was then derived by using open water and grey ice classifications as local sea surface reference points, from which the geophysically-corrected sea ice surface elevation was subtracted to yield freeboard. An example section of freeboard and surface classifications overlain on the PhaseOne imagery is shown in Figure 6a,b and a map of the 25 km gridded mean freeboard values for each ARCSIX leg are shown in Figure 6d,e. The LVIS freeboard processing code is available (Kurtz 2026).

The LVIS-derived freeboard uncertainty is calculated as the combined uncertainty from the local sea ice surface elevation retrieval and the interpolated sea surface height (SSH) reference: $\sigma_{fb}^2 = \sigma_{surf}^2 + \sigma_{S\bar{S}H}^2$ (Magruder et al. 2025). The baseline uncertainty for an individual LVIS footprint over a flat surface (σ_{surf}) is estimated to be approximately 0.06 m, based on the local standard deviation of geophysically-corrected lead heights assessed within a 50-meter scale. LVIS requires a two-dimensional approach to accurately propagate SSH reference errors. To determine the uncertainty of the reference sea surface height ($\sigma_{S\bar{S}H}$), the spatial correlation of the SSH points must be carefully accounted for. Semivariogram analysis of detrended LVIS SSH anomalies over Arctic sea ice revealed a spatial correlation length of approximately 1.7 km, which is roughly equivalent to the width of the LVIS measurement swath at high altitude. Because local oceanographic conditions, lead dynamics, and physical constraints correlate water levels within this length scale, individual SSH footprint measurements within a 1.7 km radius are not statistically independent. Consequently, the SSH uncertainty is scaled not by the raw number of SSH measurements (N_{leads}), but by the effective number of independent SSH observations (N_{eff}), such that $\sigma_{S\bar{S}H}^2 = \sigma_{SSH}^2 / N_{eff}$. The value of N_{eff} is determined as a function of the total number of SSH points used in the local freeboard estimate, weighted by their spatial distribution relative to the 1.7 km correlation length. This ensures that dense clusters of footprint measurements over a single, highly correlated lead do not artificially diminish the estimated uncertainty of the local SSH reference. Thus, the uncertainty of an individual freeboard measurement from LVIS is at minimum 0.06 m, varying dynamically based on the spatial availability and distribution of lead points used to constrain the local sea surface height.

https://doi.org/10.5194/essd-2026-241
Preprint. Discussion started: 24 July 2026

3.4 Clouds properties, boundaries, and microphysics

3.4.1 G-Band Vapor Radiometer (GVR)

The ProSensing GVR (Pazmany 2007) is an upward-looking microwave sensor with four double-band channels (±1, ±3, ±7, and ±14 GHz) centered on the 183.31 GHz water vapor absorption band, with variable bandwidths (0.5, 1.0, 1.4, and 2.0 GHz, respectively). The radiometer was developed to fit into a cloud probe canister (Zuidema et al. 2012), but for ARCSIX was mounted at the end of the aircraft tail, with the sampling footprint set by a 1.7-degree beam width. The instrument is insensitive to ice particles, unless they are large, thereby making it well-suited to distinguish the super-cooled liquid water path component of mixed-phase clouds (Ephraim et al. 2025). The data time resolution is ~6 s. The sky brightness temperatures (T_bs) are calculated using receiver gain and offsets determined from two reference loads. The absolute accuracy of the reported load temperatures is nominally ~0.2 K (Pazmany 2007), corresponding to an error in the sky brightness temperature of ~3 K; the most significant source of calibration error (Cadeddu et al. 2007).

The GVR was examined and recalibrated at ProSensing prior to ARCSIX, with a new data computer incorporated. After the campaign, an offset was detected between the GVR T_bs and dropsonde-calculated T_bs under clear skies—GVR T_bs biased high. Dropsondes released under clear skies with coincident GVR measurements are used to develop a correction to the GVR clear-sky T_bs. The 95% confidence interval straddles 3-4 K for the ±14 GHz channel and 2-3 K for the ±7 GHz channel, establishing the limiting LWP uncertainty of 13-16 g m^{-2}. All four channels performed well during the spring campaign, but the ±7 GHz channel failed between the spring and summer campaigns.

The retrievals apply an optimal estimation method (OEM; Maahn et al., 2020), with the radiative transfer calculations relying on the Passive and Active Microwave TRAnsfer (PAMTRA) model (Mech et al., 2020). Dropsondes provide the a-priori thermodynamic profiles for the cloud walls. The cloud base temperature is measured by an upward-looking infrared radiometer and a cloud mask is derived based on the measured temperature. Cloud LWP is only derived when the infrared radiometer

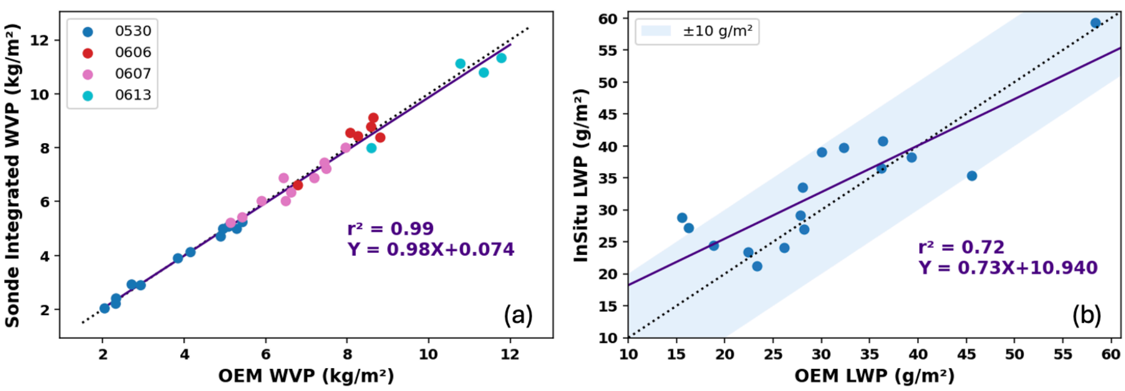

Figure 7: Comparison of (a) WVPs from dropsonde integration (y-axis) and the nearest GVR measurements (x-axis) split by altitude. and (b) LWPs for single layer porpoise legs from *in situ* FCDP measurements and the corresponding GVR values from bottom of porpoise.

indicates cloud.

The OEM-retrieved LWP and WVP values are archived in netCDF format for the 4 spring-campaign cloud walls along with the ProSensing-estimated LWPs and WVPs, the corrected and uncorrected T_bs, the altitude, latitude, and longitude, cloud base temperature when available, and the IR-radiometer-derived cloud mask. Initial in-field estimates of water vapor path (WVP) and liquid water path (LWP) relied on a neural network retrieval developed by ProSensing based on radiosondes launched from Albany, NY (Pazmany 2007). The dropsonde-integrated water vapor column agrees with the OEM-derived WVP

https://doi.org/10.5194/essd-2026-241
Preprint. Discussion started: 24 July 2026

values to within ±0.5 kg m^{-2} (Fig. 7a). Differences are reduced for smaller values of WVP, with dry measurements differing by 0.2 kg m^{-2} and moister measurements differing by 0.5 kg m^{-2}. These correspond to differences within 7%. For the cloud walls, coincident dropsondes and in situ liquid water content profiles provide an independent assessment of the retrievals. Comparing the *in situ* LWP, calculated by integrating the Fast Cloud Droplet Probe (FCDP; Sect. 3.4.2) measurements, to the bottom of the porpoise GVR LWP for flight sections that observed single layer clouds show that values are generally within 10 g m^{-2} (Fig. 7b). Typical OEM uncertainty for the single layer flight sections is ~20% (ranging from 3 g/m² to 12 g/m²).

In combination with the upward-viewing solar radiation measurements, these measurements provide the means to remotely ascertain the first aerosol indirect effect (Painemal and Zuidema 2013). Further work will extend the corrected LWP/WVP retrievals to scenes lacking dropsondes and lacking a functioning 7 GHz channel by developing a regression.

3.4.2 SPEC cloud probes

Cloud microphysical data were obtained with a suite of cloud optical probes from SPEC Inc. including the following: Fast Two-Dimensional-Gray probe (2D-Gray), Fast Two-Dimensional Stereo (F2D-S) probe with horizontal and vertical arms, Fast Cloud Droplet Probe (FCDP), a High-Volume Precipitation Spectrometer (HVPS-4), a Particle Phase Spectrometer (PPS), and Hawkeye Combination Cloud Particle Probe. These instruments obtained number size distributions (and derived products) for diameters up to 45,000 µm (Lawson et al. 2006; Woods et al. 2018; Knollenberg 1981; Lawson et al. 2017; Lawson et al. 1998). A Nevzorov hotwire probe was also deployed on the Learjet to measure liquid/total condensed water content (Korolev et al. 1998), and a WCM-2000 hotwire probe was deployed on the P-3 to measure liquid/total condensed water content (Lillie et al. 2005)

The Fast 2D-Gray probe produces four levels of gray-scale images by recording the shadowing with 10µm pixel resolution. These probes are meant to size small particles (<~100µm). The FCDP measures cloud droplet distributions and concentrations in the range of 1.5 to 50 µm. While designed for cloud droplet measurements, the FCDP has shown reliable measurements in cirrus ice clouds (Woods et al. 2018). The FCDP provides the arrival time, transit time, and pulse height of both the signal and qualifier pulse for each particle with 25 ns resolution. Recording individual particle statistics, especially arrival times, is used to eliminate closely spaced particles that may be the result of particles shattered on the probe inlet.

The F2D-S and HVPS-4 probes consist of two 128-photodiode linear arrays that capture 2D images of particles. The F2D-S has 10 µm pixel resolution at aircraft speeds up to 200 m s^{-1}. The stereo views of particles in the overlap region can also improve determination of three-dimensional properties of some particles. The F2D-S and 2D-Gray probes capture fine details of ice crystals and small water drops coexisting in mixed-phase clouds that were observed during ARCSIX. The HVPS-4 obtains particle images in the size range of about 0.1 cm to 6 cm at both 50 and 150 µm pixel resolution. The PPS provides measurements of hydrometeor phases in mixed-phased clouds and combines a 1 µm pixel resolution cloud particle imager (CPI) and a 5 µm pixel 2D-Gray probe. It is a prototype instrument developed to discriminate small water drops from ice crystals. This is the first time the PPS instrument has been flown on a research project.

The Hawkeye Combination Cloud Particle Probe was flown for ARCSIX and consists of four probes: (FCDP), a 10 µm channel 2D-S Probe, a 50 µm channel 2D-S Probe, and a Cloud Particle Imager (CPI). Hawkeye provides imagery of cloud particles and measurements of particle size distribution and number concentration.

SPEC also operated a Passive Cavity Aerosol Spectrometer Probe (PCASP) that provides aerosol particle size counts in the 0.1 to 3µm range. PCASP works like the cloud probes but is designed to detect smaller particles by measuring the light scattered by individual particles passing through the laser beam.

https://doi.org/10.5194/essd-2026-241
Preprint. Discussion started: 24 July 2026

The suite of aerosol and cloud probes provides liquid and total water content, hydrometeor number concentration and size distribution, liquid and ice water content, and particle imagery. Determining liquid water content (LWC) and ice water content (IWC)—total liquid water or ice present per unit volume—from the cloud probe data requires the integration of the combined hydrometeor particle size distribution (PSD) across multiple instruments. For ARCSIX, LWC can be computed using the combination of FCDP and optical array probes (OAPs). FCDP has a size range limited to 2-50µm and cannot be used to determine if a cloud is liquid-only, mixed-phase, or ice-only. OAPs have a larger uncertainty in the smaller size bins and should be used in conjunction with FCDP. HVPS-4 measurements should only contribute to LWC when drops >1mm are present. 2D Gray images can be used to identify the presence of irregularly shaped ice particles. The range of uncertainties in computing LWC using OAPs is large (about 20 to 100%) and depend on several factors, including the type of cloud, instrumentation, data

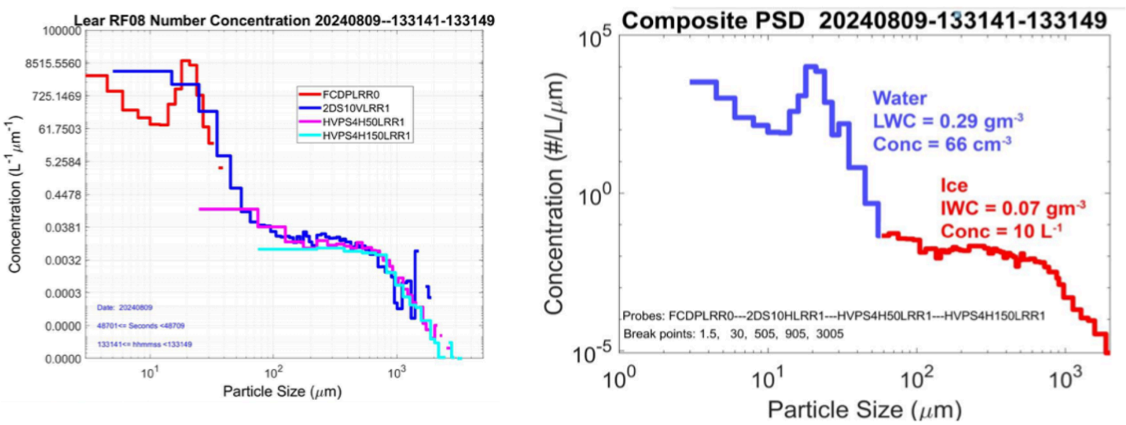

Figure 8: Example particle size distributions showing (a) size distributions from FCDP, the 2DS and the HVPS4 (b) the derived composite particle size distribution

analysis technique and the study being cited (Baumgardner et al. 1990; Twohy et al. 1997; McFarquhar et al. 2017; Faber et al. 2018)

Determining IWC requires the inclusion of additional probes. In clouds containing only small ice particles (<50µm) FCDP can be used to compute IWC. OAP data can be used to determine IWC for all ice and mixed phase clouds. For LWC and IWC in mixed phase clouds, first determine the percentage of each size bin that is ice using OAP images and multiply bins by these percentages (before applying the following method). Next, estimate IWC from PSD using the maximum diameter ($Dmax$) to Mass power law (Brown and Francis 1995) and estimate IWC from PSD using the Area-to-Mass power law (Baker and Lawson 2006). Both $Dmax$ to Mass and Area-to-Mass calculations are best performed on a composite PSD. Figure 8 shows an example composite PSD of the FCDP, the 2D-S and the HVPS-4 (FCDP 1.5-30 µm, 2D-S,H10 30-505 µm, HVPS-4, H50 505-905µm and HVPS-4,H150 905 µm +). A breakpoint is made at 50 µm that distinguishes between ice and water. IWC is calculated for bins greater than 50µm and LWC is calculated for bins less than 50 µm. The procedure to compute bulk properties of LWC and IWC where the sizes of ice particles and water drops overlap requires visual inspection of images and is manually intensive.

A few additional considerations when using microphysical probe data. For Nevzorov hot wire probes, errors in the TWC/LWC can come from larger droplets that do not vaporize fully on the hot wire and ice particles can register as water. Considerations for the FCDP are its small depth of field and since individual particles are sized and used to compute mass from diameter, sizing error is cubed in LWC calculations. For OAP probes, the depth of field increases as a function of the square of particle size, increasing until it reaches the distance between the probe arms. The concentration of particles up to 110 µm in

https://doi.org/10.5194/essd-2026-241
Preprint. Discussion started: 24 July 2026

maximum dimension are adjusted based on their depth of field. Out of focus particles that appear as "donuts" are resized using the diffraction-based correction (Korolev 1997).

3.5 Trace Gases and Aerosol Composition

3.5.1 Inlets

Most aerosol measurements were conducted downstream of a Clarke-style isokinetic shrouded solid-diffuser inlet in cloud-free air (McNaughton et al. 2007). Data collected downstream of this inlet needs to be filtered by data users during cloud penetrations due to potential cloud artifacts. Inlet icing periods have been removed prior to data archival. This inlet efficiently samples particles with aerodynamic diameters up to 5.0 µm (McNaughton et al. 2007). When in cloud, a subset of instruments sampled droplet residual particles downstream of a CVI inlet (Model 1204; Brechtel Mfg. Inc.), which has been extensively characterized for performance (Shingler et al. 2012). An inlet flag product is available and allows users to identify periods when each inlet was in use. These files provide relevant information from CVI sample periods including the estimated droplet cut size (applicable only to liquid water droplets) and the enhancement factor as calculated from information and/or equations provided by Shingler et al. (2012) and Anderson et al. (1993). The enhancement factor informs data users about how much ambient aerosol is concentrated in the inlet using information about the inlet tip area, aircraft velocity, and volumetric flow rate of sampled air. Instruments sampling downstream of the CVI included HR-ToF-AMS, DASH-SP, CFDC, A-ATOFMS, FIMS, SP2, and MPS (defined and described in the following sections).

Data users are advised to be critical of aerosol data within 10 s after an inlet switch. For un-switched instruments that always sampled from the Clarke inlet, it is recommended to use filtering to remove instances of cloud artifacts (e.g., LWC < 0.02 g m^{-3}). All aerosol measurements, unless specifically noted below, were passively dried from a combination of ram pressure at the inlet tip and generally warmer cabin temperatures compared to ambient. It is cautioned that dry aerosol measurements need to be extrapolated to ambient RH for comparison with remote sensing retrievals. Scattering hygroscopicity (i.e., f(RH)) and growth factor measurements can be used in this way. Specific instrument details can be found in individual file headers, and instrument PIs should be contacted for caveats to proper data use (e.g., rapid vertical changes, specific altitude restrictions, computation of bulk statistics).

The Particles in the Upper Troposphere, Lower Stratosphere (PUTLS; Sect. 3.5.3) package measured from a new inlet based on the design of the Passive Near-Isokinetic Inlet (PNII) (Jonsson et al. 1995). The PUTLS inlet was developed to integrate to the Clarke inlet base, replacing the inlet tip with a double-diffuser nozzle based on the PNII technique, comprising of a subisokinetic sampling interface, and a superisokinetic interface that mostly self-compensate when aircraft airspeed is varied. As a result, the inlet sample is passively compensated to be within 10% of isokinetic, minimizing the sampling bias of coarse-mode particles (>1 µm). During sampling the air parcel is slowed to near stagnation resulting in compression and adiabatic heating of the sample, evaporating volatile constituents. Thus, like the other aerosol measurements, the PUTLS data is a dry aerosol size. The PUTLS inlet has also been found to be largely resistant to ice particle shatter (Ueyama et al. 2025) due to its geometry and operation. Shatter response to mixed-phase and liquid droplet is still undergoing characterization. Data users are urged to exercise caution when in-cloud.

3.5.2 Picarro

A series of trace gases were measured to assist with air mass source classification (Vay et al. 2011; DiGangi et al. 2025). A Picarro G2401-m analyzer measured CO, CO_2, and CH_4 at 0.4 Hz resolution. Ozone was measured at 0.5 Hz resolution with a 2B Technologies Model 205 Ozone Analyzer. These systems have recent performance heritage in multiple airborne campaigns, including on the P-3B during the Cloud, Aerosol and Monsoon Processes Philippines Experiment (CAMP^{2}Ex; Reid et al. 2023). The Picarro system was calibrated hourly in flight with a single-point calibration and on the ground weekly using a 3-point calibration to verify slope calibration. The instrument was calibrated using World Meteorological Organization (WMO) standards linked to WMO X2014A (CO), X2019 (CO_2), WMO X2004A (CH_4) scales. The ozone analyzer was calibrated before and after ARCSIX using a NIST-traceable Ozone Calibration Source and zeroed hourly during flights using a potassium iodide (KI) scrubber. Uncertainties are 5ppb for CO, 0.1 ppm for Co2, and 1ppb for CH_4.

Trace gas mixing ratios together with back-trajectory analysis can be used to link air masses to source regions providing key information for ARCSIX science. Correlations among the various tracers can aid in identifying both transported and local sources and sinks. For instance, CO/CO_2 and CH_4/CO enhancement ratios provide information on biomass burning versus urban emissions, and O_3 enhancements provide indications of stratospheric influence and photochemical processing (Halliday et al. 2019; DiGangi et al. 2025)

3.5.3 Number Concentrations and Size Distributions

Aerosol number size distributions from 3 nm up to 5.7 μm were obtained from a series of instruments. Data from the Langley Aerosol Research Group Experiment (LARGE) instrument package was processed using automated procedures applied in recent field campaigns such as CAMP^{2}Ex (Reid et al. 2021) and Aerosol Cloud meTeorology Interactions oVer the western ATlantic Experiment (ACTIVATE; Sorooshian et al. 2023) to measure aerosol size distributions. All LARGE data are reported at standard temperature and pressure conditions (0°C, 1013.25 mb) and are synchronized to the time response for DLH. A pair of TSI-3772 condensation particle counters (CPCs) obtained number concentrations of particles with diameters larger than 10 nm; one instrument was untreated and one with an upstream thermodenuder (350°C) to measure only particles containing a non-volatile particle core. CPC data are corrected for coincidence errors when the aerosol concentrations exceed 10,000 cm^{-3}. LARGE also operated an Aerodynamic Particle Sizer (APS: 0.53 – 5.0 μm) to observe the size distribution of coarse-mode particles like mineral dusts and sea-salts. Integrated APS number, surface area, and volume concentration data for the full instrument range and for coarse-mode particles only (1.0 – 5.0 μm diameter) are provided based on the assumption of spherical particles. Note that any comparisons between APS aerodynamic diameter and measurements utilizing optical or mobility diameters require correction for particle shape and density.

A Fast-Integrated Mobility Spectrometer (FIMS) also provided aerosol particle distributions between 0.01 – 0.5 μm (Wang et al., 2017, 2018) with 1 Hz time resolution. The FIMS operates on the principle of spatially separating aerosol particles according to their mobility size and simultaneously detecting the separated particles of different sizes by applying an electric field. The original FIMS employs a uniform electric field (Kulkarni and Wang 2006a,b), and its dynamic size range is limited to a factor of 10 in electrical mobility to maintain a mobility resolution no less than 5. The FIMS deployed during ARCSIX employs a spatially varying electric field resulting in a greater dynamic size range compared to the original design (Wang 2009). The aerosol size distributions are derived using an inversion routine (Wang et al. 2018, Olfert et al. 2008) and reported at standard temperature and pressure conditions. The uncertainties in aerosol number concentration and particle diameter are estimated to be 20% and 3%, respectively.

The PUTLS instrument package provided aerosol size and concentration data at 1 Hz for particles between 0.003 and 3 μm using three separate instruments. A Nuclei-Mode Aerosol Size Spectrometer (NMASS) consists of 5 separate CPCs, typically operating with cutpoint diameters of 3, 7, 12, 22, and 32 nm (see International Consortium for Atmospheric Research on Transport and Transformation (ICARTT) header for values from each date) to examine the size range between 3 – 60 nm when used with the total number concentration obtained from the Ultra-High Sensitivity Aerosol Spectrometer the (UHSAS). The

NMASS data can be inverted to create a size distribution following the technique in Williamson et al. (2018) and is also used in creating the New Particle Formation (NPF) flag. A UHSAS and Printed Optical Particle Spectrometer (POPS) provided distributions of particle optical size in the ranges of 0.06 – 1 µm and 0.14 – 3 µm, respectively. High time resolution of aerosol size distribution data from FIMS and PUTLS enable investigations of new particle formation (e.g., Xiao et al. 2023; Zheng et al. 2021; Ueyama et al. 2025), vertical aerosol transport (e.g., Wang et al. 2016), and evolution of aerosol size distributions (e.g., Zaveri et al. 2022).

Error! Reference source not found.9 shows the campaign-wide geometric mean size distributions from the native sizing instruments. The comparison shows consistency across their overlapping size ranges, although some differences remain. Most differences are within one campaign-wide geometric standard deviation, suggesting that the campaign-mean differences are generally within the observed campaign variability. These differences are expected because the instruments use different measurement principles and sizing methods while reporting different types of particle diameters. The merged aerosol size distribution (Fig. 9) is based on measurements from the FIMS, UHSAS, POPS, and APS instruments. The native size distributions were first fit across overlapping size ranges using FIMS as the reference and then converted to a common volume-equivalent diameter basis before merging. The merged size distribution reconciles differences among the native sizing instruments and provides a physically reasonable and consistent representation of the observed aerosol size distribution.

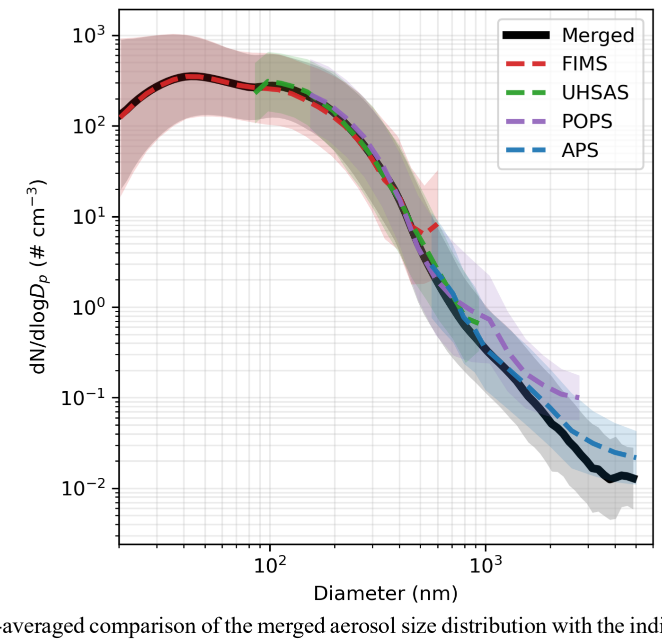

Figure 9: Campaign-averaged comparison of the merged aerosol size distribution with the individual FIMS, UHSAS, POPS, and APS size distribution measurements from 20 nm to 5 µm, for cloud free periods. The merged aerosol size distribution is shown as a solid black line, and the native instrument measurements are shown as dashed colored lines, with FIMS in red, UHSAS in green, POPS in purple, and APS in blue; all lines represent the geometric mean of the 1 min size distributions. Shaded regions indicate one geometric standard deviation. The code used to produce the archived ARCSIX aerosol size distribution and figure, is included in the GitHub repository under the notebooks folder as a SizeDistMerge case example. The jupyter notebook is "arcsix_1min_merged_sizedist_production.ipynb" (Chen 2026; https://doi.org/10.5281/zenodo.20709064).

3.5.4 Chemical composition

https://doi.org/10.5194/essd-2026-241
Preprint. Discussion started: 24 July 2026

Open Access Earth System Science Data Discussions

Online aerosol composition was measured with three different instruments and atmospheric particle samples were collected for off-line measurements to obtain a comprehensive picture of the chemical constituents of Arctic aerosols. The High-Resolution Time-of Flight Aerosol Mass Spectrometer (HR-ToF-AMS; Aerodyne; DeCarlo et al. 2008) obtained data on the non-refractory (i.e., volatile at 600°C) constituents with a nominal vacuum aerodynamic diameter range between 0.06 – 0.6 µm. These species include organic compounds, sulfate, nitrate, chloride, and ammonium, along with numerous mass-to-charge (m/z) fragments suggestive of different particle sources/species: 42 (amines), 43 (mixed hydrocarbons), 44 (oxidized hydrocarbons), 55+57 (hydrocarbons), 58 (NaCl), 60 (smoke), 79 (methanesulfonate/marine), and 91 (aromatic hydrocarbons). As done in recent campaigns (i.e., ACTIVATE, CAMP^{2}Ex) the instrument operated in 1 Hz fast-MS-mode, with 25 s with the chopper in the open position and 5 s in the closed position. The instrument's ionization efficiency was determined with 400 nm monodisperse ammonium nitrate particles, a relative ionization efficiency of 3.2 was used for ammonium (based on laboratory generated ammonium sulfate). A collection efficiency of 1.0 was applied to all data. Instrument limits of detection (LODs; µg m^{-3} at STP) at 1 Hz are as follows: 0.378(Org), 0.071(SO4), 0.137(NO3), 0.321(NH4), 0.057(Cl), 0.053(mz42), 0.048(mz43), 0.088(mz44), 0.050(mz55), 0.035(mz57), 0.024(mz58), 0.0026(mz60), 0.026(mz79), 0.021(mz91). While data below these LODs are not valid numerically, these data are retained in the archive for unbiased statistics, 0.5 times the LOD should be used for further averaging per MacDougall et al. (1980).

The Aircraft Aerosol Time-of-Flight Mass Spectrometer (A-ATOFMS) measures the size and chemical composition of individual dry particles between 0.09 - 2.0 µm vacuum aerodynamic diameter in real-time (Pratt et al. 2009; Gunsch et al. 2017; Murphy et al., 2019; Schill et al., 2020). A-ATOFMS directly measures both non-refractory (e.g., organics, ammonium, nitrate, sulfate) and refractory (e.g., soot (black carbon), sea salt, mineral dust, metals) material by using a Q-Switched 266nm laser to desorb and ionize each aerosol particle individually (Pratt and Prather 2012). The A-ATOFMS sampled atmospheric aerosols mainly from the aerosol concentrator (see Section 3.5.6) and cloud residual particles from the CVI.

During ARCSIX, the A-ATOFMS chemically analyzed >47,000 individual particles (including all research and transit flights). The single-particle dual-polarity (positive and negative ion) mass spectra (i.e. two mass spectra per individual particle) are analyzed in FATES (Flexible Analysis Toolkit for the Exploration of SPMS data; Sultana et al. 2017), and clustered using Art-2a (Song et al. 1999). The clusters are manually combined to represent chemically distinct particle types, including sea salt aerosol, aged biomass burning, mineral dust, and sulfuric acid-rich (with trace organics), based on the combinations and intensities of marker ions in the single-particle mass spectra (Pratt and Prather 2010; and prior Arctic A-ATOFMS measurements (Gunsch et al. 2017; Gunsch et al. 2020; Wu et al. 2024). Size-resolved number fractions of the chemically-distinct particle types are calculated, and if a sufficient number of particles are measured in a given time period, then these number fractions can be calibrated to particle type number and mass concentrations, following Froyd et al. (2019), and using the UHSAS and APS size distributions. Size-resolved single-particle type number fractions and associated standard errors (based on particle statistics) at 5 min time resolution are archived.

Refractory black carbon mass concentration measurements were conducted with a Single Particle Soot Photometer (SP2; Schwarz et al. 2006). The mass-response for the SP2 instrument was calibrated using monodisperse Aquadag soot surrogate particles and BC quantification was conducted using the broad-band high-gain detector only. Final data processing was performed with the PSI SP2 toolkit v4.116. Although the size range of measurements is sensitive to the density of incandescing particles; the size range is typically 90 – 300 nm.

Atmospheric particles were also collected using a 3-stage microanalysis particle sampler (MPS-3), corresponding to aerodynamic diameters of 0.05-0.3, 0.3-2.0, and >2.0 µm (Kirpes et al., 2020). The MPS sampled from the isokinetic inlet and CVI; Table S3 summarizes sampling times. Particles were impacted onto transmission electron microscopy (TEM) grids (carbon

https://doi.org/10.5194/essd-2026-241
Preprint. Discussion started: 24 July 2026

Open Access Earth System Science Data Discussions

Type-B Formvar film copper grids) and silicon (Si) wafers. During ARCSIX, 231 substrate samples were collected, with a time resolution of ~10 min - 1 h per sample and hundreds to thousands of particles collected per substrate. These samples are being analyzed using computer-controlled scanning electron microscopy with energy dispersive X-ray spectroscopy (CCSEM-EDX), Raman microspectroscopy, and optical-photothermal infrared (O-PTIR) spectroscopy (Mirrielees et al. 2022). CCSEM-EDX provides single-particle morphology and elemental composition, with *k*-means clustering enabling identification of single-particle types, including sea spray aerosol, mineral dust, soot, and organic-sulfate particles (e.g., Kirpes et al. 2018; Kirpes et al. 2022). Raman microspectroscopy and O-PTIR provide single-particle functional group analysis, enabling identification of marine organic compounds, minerals, and sulfate, for example (Kirpes et al. 2019; Mirrielees et al. 2022).

Atmospheric particles were also collected through the isokinetic inlet using an automated size and time-resolved aerosol collector (STAC) platform loaded with 20 customized 4-stage cascade impactors (50% cut-off sizes are 2.3, 0.62, 0.42, and 0.12 µm for Stages A to D, respectively; Cheng et al. 2022). Table S4 summarizes sampling times. The 4-stage cascade impactors were loaded with 1 transmission electron microscopy (TEM) carbon Type-B grids on stage A and B, two TEM carbon Type-B grids and a Silicon nitride (SiNx) substrate on Stage C, and one TEM carbon Type-B grid, one TEM carbon lacy grid, and one SiNx substrate on Stage D. A total of 116 impactor samples (i.e., 928 substrates) were collected, with a time resolution ranging from ~10 min to ~3 hours. As for the MPS TEM grids and Si samples, the STAC TEM grids are also being analyzed by CCSEM-EDX. These samples are being analyzed to probe their water-uptake activity and hygroscopicity (Cheng et al. 2021) and are being analyzed by transmission electron microscopy to probe detailed structures, individual particle optical properties, and volatilities (Cheng et al. 2024; Mathai et al. 2023; Veghte et al. 2018). SiNx substrate on Stage C can be used for Ice nucleation ESEM analysis to probe ice nucleation activity of individual particles (Lata et al. 2021). Additionally, Stage D SiNx substates can be analyzed with nanospray desorption electrospray ionization with high-resolution mass spectrometry (nano-DESI-HRMS) to probe the molecular formula of organics (Mansoura et al. 2025). Stage TEM carbon B-Film samples are being analyzed by scanning transmission X-ray microscopy with near-edge X-ray absorption and fine structure spectroscopy (STXM-NEXAFS) to probe the carbon functionalities of individual particles (Sharpe et al. 2026).

3.5.5 Optical Properties

Total light scattering coefficients at 450, 550, and 700 nm were measured with a TSI-3563 nephelometer and corrected for truncation errors using the method of Anderson and Ogren (1998). Data are provided at 1 Hz for bulk aerosol (< 5 µm) and for the sub-micron range (< 1 µm) owing to the use of a 1 µm cyclone (Mesa Labs/BGI, Ambient Particulate Inlet model SCC2.654) operated at 22 liters per minute. Absorption coefficients at 470, 532, and 660 nm were measured with a Radiance Research Particle Soot Absorption Photometer (PSAP; Mason et al., 2018). The PSAP data had various corrections applied following Virkkula (2010). A 9-second boxcar smoothing algorithm was applied for consistency with previous campaigns. Both the nephelometer and PSAP measurements were made for dried conditions (i.e., RH < 40 %).

Sub-micron aerosol extinction is calculated at 532nm as the sum of sub-micron scattering and bulk (< 5 µm) absorption. Note that although the size ranges for scattering and absorption are not matched, it can be assumed that super-micron absorption is negligible compared to sub-micron absorption. To do this calculation, the 550 nm scattering coefficients were converted to values at 532 nm using the calculated angstrom exponent. Consequently, an aerosol scattering threshold of 2 Mm^{-1} is used for calculations of extinction. Regarding the wavelength-dependent angstrom exponent parameters, both the scattering and absorption angstrom exponents were derived using scattering coefficients at 450 and 700 nm and absorption coefficients at 470 and 660 nm, respectively. Single scattering albedo (SSA) values are archived at the three nephelometer wavelengths (450, 550,

https://doi.org/10.5194/essd-2026-241
Preprint. Discussion started: 24 July 2026

700 nm). The SSA and angstrom exponent values archived, underwent 30 s running average smoothing and were only archived if the input coefficient data exceeded 2 Mm^{-1}.

Scattering hygroscopic growth was calculated with the f(RH) parameter by relying on a second sub-micron nephelometer (in parallel to the one measuring dry sub-micron scattering), which included humidification of the incoming aerosol stream to approximately 85% RH. The archived f(RH) variable represents the ratio of humidified (80%) and dried (20%) scattering, with scattering computed at target RHs via the gamma parameter (Ziemba et al. 2013). The gamma and f(RH) values reported represent sub-micron aerosol. Data are archived only when both the nephelometer scattering coefficients were ≥ 5 Mm^{-1}, the humidified nephelometer was within 10% of the 85% RH setpoint, and when the humidified RH exceeded the low RH by at least 25%. Note that values of f(RH) below unity are not entirely unexpected as such values have been reported in previous campaigns (e.g., Shingler et al. 2016a; Lorenzo et al. 2025). Measurements of RH and f(RH) were calibrated using the known deliquescence behavior of ammonium sulfate. Scattering and extinction coefficients at ambient RH are also archived using measured dry scattering (and absorption to calculate extinction), f(RH) and the gamma function, and ambient RH measurements from the DLH instrument.

The Differential Aerosol Sizing and Hygroscopicity Spectrometer Probe (DASH-SP; Brechtel Mfg. Inc.) provided an additional hygroscopicity measurement (Sorooshian et al. 2008; Shingler et al. 2016b). This instrument first selects dry particles of a desired size between 0.16 – 1 µm and then splits the flow between a dry channel with an optical particle counter (OPC, 405 nm) and a humidified channel where the air stream first goes through a diffusion-based humidifier followed by an identical OPC. The humidified RH was selected to be near 85% for most of ARCSIX to allow for better intercomparisons with the f(RH) measurement. Based on calibrations with laboratory-generated salts with known refractive indices, a 3-dimensional retrieval surface is used to provide both the dry particle refractive index (real part) and the final humidified diameter, which is divided by the originally selected dry diameter to provide a hygroscopic growth factor. The data archived include growth factor and effective values for the real part of the refractive index at 405 nm. Limitations are that the value assumes spherical particles and can be biased when absorbing components are present (Shingler et al. 2016a, b). The time resolution depended on ambient particle concentration and typically was less than 1 minute per scan. Uncertainty for DASH-SP measurements (real refractive index: 0.02; growth factor: 4.5%) was estimated by applying the 3-dimensional retrieval surface to calibration data from laboratory-generated pure salts spanning the measured range of dry diameters and calculating the pooled standard deviation of the residuals between retrieved and reference values for real refractive index and growth factor for dry conditions. These uncertainties are likely an upper bound, as a median of five consecutive DASH-SP measurements were averaged to improve sampling statistics. Uncertainty in RH (0.8% RH) was estimated by taking the median standard deviation of RH over the sampling periods of DASH-SP GF measurements.

3.5.6 Cloud Concentration Nuclei (CCN) and Ice Nucleating Particle (INP) Concentrations

A Cloud Condensation Nuclei counter (CCNc) measured CCN number concentration at specified instrument supersaturation, with most of ARCSIX focused on ~0.2%. The CCNc measured the number concentration of aerosols that activate within a continuous-flow cylindrical column at the specified supersaturation. The sample air flows through the center of the column surrounded by a particle-free sheath flow that is exposed to a streamwise thermal gradient. This creates a stable region of supersaturation. Aerosol particles that act as nuclei at the specific supersaturation grow into droplets and are then counted and sized by an OPC. We caution data users that this is not the supersaturation of the sampled clouds, rather a value prescribed for the instrument itself. The CCNc was pressure controlled at 500 hPa and resulting concentrations are corrected to standard temperature and pressure.

https://doi.org/10.5194/essd-2026-241
Preprint. Discussion started: 24 July 2026

Open Access Earth System Science Data Discussions

The INP concentrations were measured using two techniques: the Colorado State University Ice Spectrometer (CSU IS, Hiranuma et al. 2015, McCluskey et al. 2018) and a Continuous Flow Diffusion Chamber 1H (CSU CFDC-1H), both reporting number concentrations (# L^{-1} at STP conditions). The Ice Spectrometer is an offline immersion freezing device where filter samples are collected downstream of an isokinetic aerosol inlet using 47-mm diameter aluminum in-line filter holders with pre-cleaned 0.2 µm pore diameter Nucleopore polycarbonate filters overlaid on pre-cleaned 10 µm pore diameter filters to limit contamination (Barry et al. 2021). For ARCSIX, offline samples were generally collected during level legs with separate samples accumulated above and below cloud. and frozen at -20°C until analysis INP concentrations as a function of temperature are determined based on methods of Vali et al. (1971) with error estimates based on binomial statistics from Agresti and Coull (1998). Corrections are applied for freezing events observed during each experiment in a clean DI water sample and using for INP concentrations detected in field blanks collected throughout the field campaign. Prior to aliquoting sample for testing, additional treatments were performed on some samples, resulting in up to three different INP spectra for each sample: (i) no treatment, (ii) treatment to denature and deactivate proteinaceous or biological INPs through exposure to 95°C for 20 min, and (iii) treatment to remove organic INPs through exposure to H_2O_2 under UVB at 95°C for 20 min, followed by catalase addition to remove residual peroxide prior to testing.

Online CFDC measurements of INP concentrations were also collected complementing the offline INP spectra. The CFDC is an ice thermal gradient diffusion chamber that optically counts the number of single freezing aerosol particles (Rogers et al. 2001; DeMott et al. 2015). Measurements are made for one set of supersaturation and temperature conditions at a time, with significantly higher time resolution than filter samples and the ability to sample cloud water residuals. Measurements were performed between -31 and -18°C and 3-7% supersaturation, with respect to liquid water. To improve sampling statistics at low INP concentrations, as during ARCSIX, CFDC sampling during many periods was performed downstream of an aerosol concentrator (MSP 4240) that selectively enhances aerosol concentrations above ~500 nm. The instrument operates by concentrating aerosol in a major inlet flow (~250 LPMv) into a minor outlet flow (~1.5 LPMs) reaching enhancement factors of up to ~100x for supermicron aerosol. This sampling setup has been used previously for ground-based measurements (Tobo et al. 2013; McCluskey et al. 2017) and was deployed for the first time in an aircraft campaign during the National Science

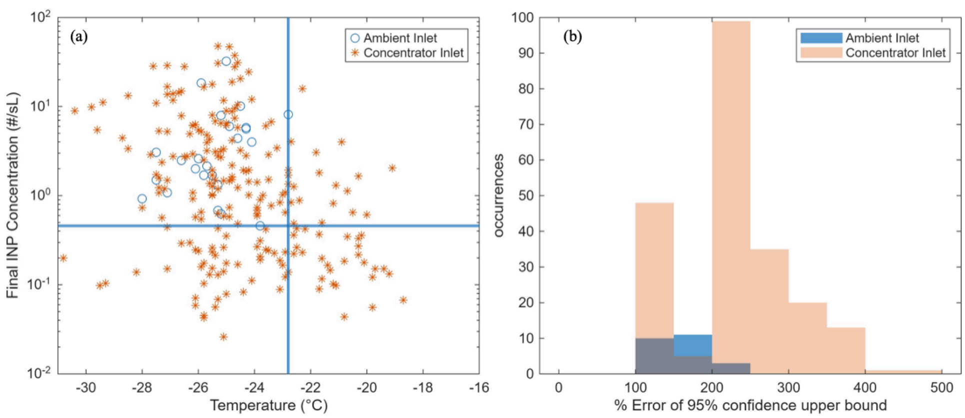

Figure 10: (a) All significant final CFDC INP concentrations measured during the ARCSIX campaign with colors indicating direct ambient measurements (blue) and measurements downstream of the aerosol concentrator (red). Blue lines are drawn for the lowest concentrations and warmest temperatures measured without the aerosol concentrator. (b) % Error values for 95% confidence interval upper bounds for significant data collected via direct ambient measurements (blue) and downstream of the aerosol concentrator (red). These are calculated as (upper bound/measured value) *100. Plotting code is available from Perkins (2026).

https://doi.org/10.5194/essd-2026-241
Preprint. Discussion started: 24 July 2026

Foundation (NSF) Cold Air Outbreak Experiment in the Sub-Arctic Region (CAESAR) campaign on the National Center for Atmospheric Research (NCAR) C-130 research aircraft immediately prior to ARCSIX. The CFDC also sampled INP concentrations in cloud-water residuals by sampling downstream of the CVI, resulting in three different sample types: (i) ambient sampling through an isokinetic inlet, (ii) enhanced sampling downstream of the aerosol concentrator, and (iii) sampling of cloud water residual INP downstream of the CVI. For all sampling types, a 2.5 µm aerosol impactor was utilized upstream of the CFDC to remove large hygroscopic aerosols that could be mistaken for INPs. INP concentrations are calculated for continuous measurement periods, subtracted for adjacent background measurement periods of HEPA filtered air (generally rotating 10-min sample periods and 5-min background periods). This is done using Poisson distribution statistics and uncertainty calculations as described in Barry et al. (2021).

For sampling types (ii) and (iii), corrections were necessary to infer ambient INP concentrations. For sampling downstream of the aerosol concentrator, INP enhancement ratios are more complex to derive due to size dependent enhancement and unknown, variable INP size distributions. These ratios are calculated using ratios of INP concentrations measured on the isokinetic inlet to those downstream of the concentrator. Aerosol size distributions were examined to determine periods where these comparisons are appropriate. For periods without good direct ambient concentrations for comparison, largely due to ambient concentrations falling below instrument detection thresholds, enhancement ratios were estimated based on observed enhancements in aerosol concentrations >500 nm. Uncertainty estimates are produced for the concentration ratio based on how well-constrained they are, of ±10% for the best constrained cases (good ambient-concentrator comparisons in a similar location and aerosol environment) up to factor of two uncertainty for the most poorly constrained. Uncertainties in some cases are further constrained by limiting enhancement ratios of 1 (all INP are too small to be enhanced) and 100 (all INP are super micron and concentrator operating at maximum efficiency). These are propagated multiplicatively with raw INP bounds to produce conservative final INP confidence intervals.

In practice, the use of the aerosol concentrator allowed for measurements at lower concentrations than the ambient inlet, evidenced by the range of measurements collected on each inlet in Fig. 10. From these data, at least one order of magnitude lower ambient INP concentration was measured with the aerosol concentrator. Because INP concentrations generally increase exponentially with decreasing temperatures, this also allows successful measurements at warmer temperatures than could be achieved with direct ambient measurements. One downside to aerosol concentrator measurements, however, is that upper uncertainties for INP concentrations are higher than for direct ambient measurements, shown in Fig. 7. Though this is largely due to uncertainties in concentration factors that can be better constrained if operating conditions are constrained to those where direct ambient measurements produce significant data. Stated differently, the increased uncertainty associated with concentrator sampling is due to ambient measurements producing non-significant data or not being performed; in some cases, this is due to the rapidly changing external conditions associated with aircraft sampling. Beyond these considerations, an additional advantage of the concentrator sampling is improved temporal resolution. Sample integration windows are largely constrained by the amount of time required to collect a significant number of INP detections, so shorter sampling windows can be utilized when higher detection rates are accomplished downstream of the aerosol concentrator. Overall, the data demonstrates the usefulness of the combination of aerosol concentrator and CFDC instrumentation in a challenging field environment, improving instrument sensitivity and temporal resolution in was that enhanced ARCSIX science. The downside to this sampling setup, less constrained error estimations, is largely due to sampling conditions that could not be sampled otherwise. In cases where ambient sampling was possible, concentration factors can often be well-constrained through proper operating procedures (switching between concentrator and ambient sampling), eliminating this downside.

https://doi.org/10.5194/essd-2026-241
Preprint. Discussion started: 24 July 2026

3.6 Airborne Cameras

Airborne camera images provide useful context for data analysis. Airborne images were collected by a nadir-facing camera mounted beneath the airplane and a forward-looking camera mounted in the cockpit. Table 2 summarizes the details of the Samsung SNB-9000 cameras used to provide forward and nadir views from the P-3B. Photos from these cameras were stitched with UTC time stamps and archived as MP4 videos. These cameras are not radiometrically calibrated.

4 G-III instrumentation

The NASA C-20B Gulfstream III (G-III) aircraft was used as a high-flying platform during ARCSIX generally flying at ~11.7 km (~39,000ft). The G-III contained two remote sensing instruments and dropsondes to provide vertically resolved atmosphere state, aerosol, and cloud information and reflected shortwave radiances to characterize the cloud and surface radiative properties (Fig. 11). Table 3 describes the associated measurement details (resolutions, uncertainties) and references describing individual instruments and data products. The flights were generally 5 hours long with a nominal airspeed of ~405 knots and flown in coordination with the P-3B.

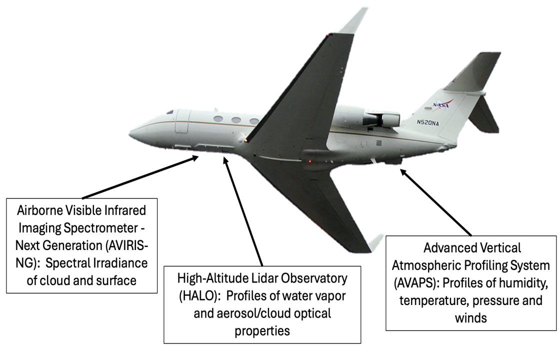

Figure 11: G-III instrumentation configuration (courtesy of Amin Nehrir and Brian Collister)

Table 3. Summary of G-III instrumentation and measurements.

Instrument	Measured/Retrieved Parameter	Uncertainty	Time/Spatial Resolution Details	Reference/Notes
Navigation and State Variables				
Northrop Grumman Litton 251 EGI, UNS-1Fw Flight Management System, Sperry Aircraft Data Computer	Latitude, Longitude	~5 m SEP; 0.01°	1 s	
	Altitude (pressure, GPS), Ground and Vertical Speed, Mach Number, Angles (Track, Drift, Pitch, Roll), Solar Reflectance Angles	~ 1 ms-1; 10°	1 s	
Northrop Grumman Litton 251 EGI & Avionics	Horizontal Wind Speed and Direction	~ 1 ms-1; 10°	1 s	
Rosemount 102 Sensor	Total Air Temperature	0.3-0.5° C	1 s	
KT15.95 II Infrared Pyrometer	Temperature		1 s	
AVAPS - Vaisala NRD41 Dropsonde	Latitude/Longitude	NA	4 hz	
	Altitude	NA	4 hz	
	GPS Altitude	NA	4 hz	
	Pressure	0.5 hPa	2 hz	Vömel et al., 2021, 2023; NRD41 Datasheet (https://docs.vaisala.com/v/u/B212680EN-A/en-US)
	Temperature	0.2°C	2 hz	
	Dew Point Temperature	0.1% RH	2 hz	
	Relative Humidity	3%	2 hz	
	Horizontal Wind (u and v components)	0.5 m s^{-1}	4 hz	

https://doi.org/10.5194/essd-2026-241
Preprint. Discussion started: 24 July 2026

	Vertical Wind	1 m s^{-1}	4 hz	
High-Altitude Lidar Observatory (HALO): "x m/y m" indicates x m vertical resolution and y m horizontal resolution along the track	Aerosol Backscatter (532/1064 nm)	0.2 Mm^{-1} sr^{-1}	15 m x ~2 km	Hair et al., 2008; Burton et al., 2015, 2018
	Aerosol Extinction (532 nm)	10 Mm^{-1}	300 m x ~12 km	
	Depolarization (532/1064 nm)	0.01	15 m x ~2 km	
	Aerosol Optical Depth (532 nm)	0.01	N/A x ~12 km	
	Aerosol Type (e.g., marine, dust, smoke)	Qualitative	300 m x ~12 km	Burton et al., 2012
	Specific Humidity	5-20%$^{+}$	~300-700 m x ~12 km	
	Total Precipitable Water Vapor	~1%	N/A x ~12 km	
	Relative Humidity (derived using reanalysis)	<20% $^{+}$	~300-700 m x ~12 km	
	Cloud top extinction profile (532 nm)	10 Mm^{-1}	1.25 m x ~0.2 km	Hair et al., 2026
	Cloud phase (e.g., liquid, ice, mixed phase) (532 nm)	NA	15 m x ~0.2 km	Crosbie et al., 2025
	Surface winds (over open water)	<2 m s^{-1}	N/A x ~ 2 km	Dmitrovic et al., 2024
Airborne Visible Infrared Imaging Spectrometer (AVIRIS-NG): ~11 m represents ground sampling distance	At-sensor Radiance (380-2510 nm)	1-5 % bias and varying SNR as a function of wavelength, airspeed, solar angle, and surface brightness; reference SNR for the brightest targets with slow airspeed is 800-1000	~11 m	Chapman et al., 2019
	Column Water Vapor	0.1 cm	~11 m	Thompson et al., 2021
	Aerosol Optical Depth (550 nm)	0.2	~11 m	Thompson et al., 2019; Brodrick et al., 2022
	Surface and Cloud Top Reflectance (380-2510 nm)	2-5%	~11 m	Thompson et al., 2016; Thompson et al., 2018
	Surface Broadband Albedo	< 0.01	~11 m	Painter et al., 2013
	Surface Radiative Forcing	4 W m^{-2}	~11 m	Painter et al., 2013
	Surface SW Radiative Flux	4 W m^{-2}	~11 m	Painter et al., 2013
	Optical Absorption Path (liquid and solid water)	0.07 cm	~11 m	Bohn et al., 2020
	Cloud Thermodynamic Phase (liquid, mixed, ice)	Qualitative	~11 m	Thompson et al., 2016; Marchant et al., 2016
	Cloud Mask (clear/cloudy discrimination)	Qualitative	~11 m	
	Cloud-top Height	TBD	~11 m	
	Cloud Effective Particle Radius	TBD	~11 m	Platnick et al., 2017; Platnick et al., 2021
	Cloud Optical Thickness	TBD	~11 m	
	Cloud Water Path (derived from CER, COT)	TBD	~11 m	

1010 **4.1 Atmospheric state and navigation data**

The acquisition of atmospheric state and navigational data on the G-III was conducted with a flight management system (Applanix AX 210). Collected data were like those on the P-3B as shown in Table 3.

https://doi.org/10.5194/essd-2026-241
Preprint. Discussion started: 24 July 2026

4.2 High-Altitude Lidar Observatory (HALO)

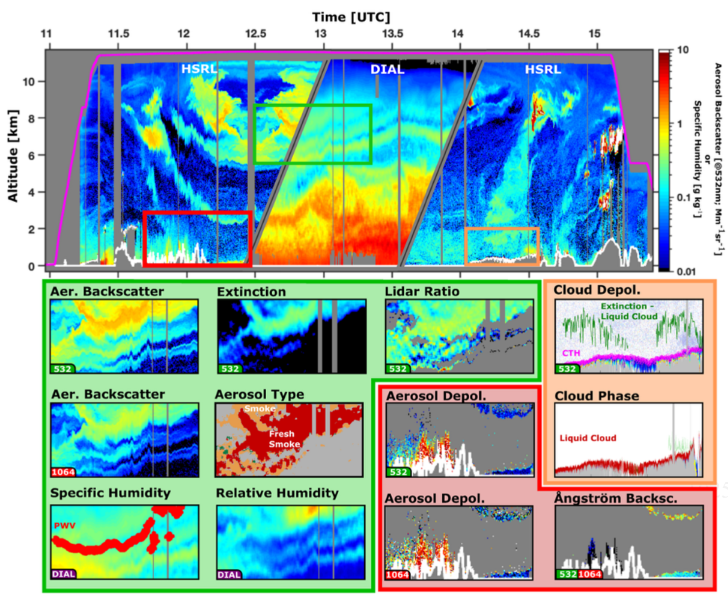

Figure 12: Examples of the available HALO data products for RF8 (2024-06-10) showing profiles of aerosol backscatter (532 nm) for the entire flight. Note the horizontal and vertical variability in the aerosol particles. Example code is provided by Collister and Nehrir (2026).

The NASA Langley Research Center HALO is a multifunctional airborne lidar system that provides vertically-resolved aerosol and cloud optical properties and profiles of water vapor or column measurements of methane depending on configuration. Figure 12 provides example data from RF8. HALO was operated in the water vapor/aerosol/cloud configuration during ARCSIX, employing the differential absorption lidar (DIAL) technique for water vapor profiling (Carroll et al. 2022) and the high spectral resolution lidar (HSRL) and elastic backscatter techniques (532 nm and 1064 nm, respectively) for aerosol and cloud measurements (Burton et al. 2015; Crosbie et al. 2025; Hair et al. 2008). DIAL provides a direct, vertically-resolved measurement of water vapor absorption via ratios of signal attenuation, eliminating the need for absolute calibration. The DIAL technique is implemented in HALO using four wavelengths (three wavelength pairs) spread across a water vapor absorption complex near 935 nm to capture the large dynamic range of absolute humidity that occurs between the stratosphere and planetary boundary layer (~0.001 to 23 g kg^{-1}). The 532 and 1064 nm channels are sampled at high vertical resolution (~1.25 m) to permit critical cloud and surface sampling, and both channels separate the return signal into co- and cross-polarized components. Estimated uncertainties are shown in Table 3 and archived for each aerosol and water vapor product.

HALO aerosol and water vapor products are archived in a single HDF5 file for each flight. Aerosol products include vertically and horizontally resolved "curtains" of aerosol backscatter at two wavelengths (532 and 1064 nm) and independent measurements of extinction at 532 nm (Hair et al. 2008). Intensive optical properties (*i.e.* concentration independent) derived

https://doi.org/10.5194/essd-2026-241
Preprint. Discussion started: 24 July 2026

Open Access Earth System Science Data Discussions

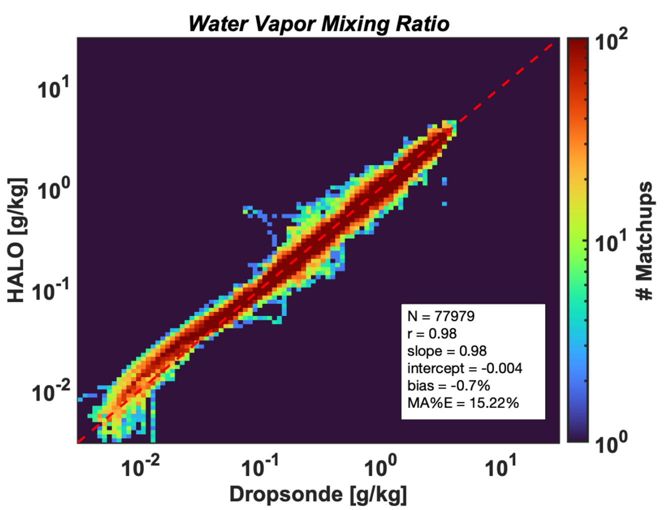

Figure 13: Comparison of HALO derived water vapor mixing ratio (y-axis) versus dropsonde measured water vapor mixing ratio for the full ARCSIX campaign. MA%Edenotes Mean Absolute percent error.

from HALO aerosol measurements include the backscatter Ångström exponent, lidar ratio (i.e., extinction-to-backscatter ratio), and aerosol depolarization ratio; these are used as input into the aerosol-type classification algorithm (maritime, polluted maritime, pure dust, dusty mix, smoke, fresh smoke, urban, and ice; Burton et al. 2012). A cloud mask is generated on a flight-by-flight basis using a Haar wavelet filter to identify strong vertical gradients in the 532 nm signal to select a threshold that separates sharp cloud edges from more diffuse aerosol features and removing signals below cloud top prior to computing the aerosol products. All aerosol products are screened for clouds except for unscreened aerosol scattering ratio and backscatter products that are archived in addition to their cloud-screened counterparts. To ensure that aerosol products are computed with sufficient signal-to-noise, a low signal mask is generated using a threshold on the molecular signal levels, and aerosol depolarization is computed only when the aerosol scattering ratio exceeds 0.1. HALO backscatter and depolarization products are archived as 10 s averages, extinction and lidar ratio products are averaged to 60 s, and all data are decimated to 10 s horizontal and 15 m vertical bins. Higher-resolution aerosol products are available upon request. Figure 13 shows agreement between HALO water vapor mixing ratio against AVAPS (Sect. 4.4) dropsondes for the entire campaign. The comparisons were limited to below 10 km. Strong correlation is observed between the two measurements in the troposphere, however, a known dry bias in the AVAPS measurements in the stratosphere is identified using the accurate HALO observations (Carroll et al. 2022).

HALO cloud and surface products are archived in a separate HDF5 file. Cloud products include cloud top and base heights for multilayer clouds (up to 5 layers), a suite of vertically integrated cloud optical properties (integrated attenuated backscatter, linear depolarization, water cloud extinction, and lidar ratios for opaque clouds), profiles of liquid-cloud extinction, and a cloud phase classification mask (water-dominant, mixed, ice dominant, horizontally oriented ice, aerosol; Crosbie et al. 2025; Sorooshian et al. 2025). Surface products include surface reflectance and depolarization as well as 10 m neutral stability wind speeds derived from wave slope variance estimates over open water (Dmitrovic et al. 2024). All cloud and surface products are reported at a horizontal resolution of 2 Hz. The cloud phase mask is reported at the same 15 m resolution as the aerosol data, and the water cloud extinction profiles are reported in 1.25 m vertical bins referenced to cloud top.

The ARCSIX team has also optimized machine-learning (ML)-based estimates of cloud condensation nuclei (CCN) concentrations at 0.2% supersaturation and aerosol absorption at 532nm, using the HALO lidar observations of aerosol backscatter, extinction, and depolarization as predictor inputs. These data have the same format and location as the HALO native

https://doi.org/10.5194/essd-2026-241
Preprint. Discussion started: 24 July 2026

data and are based on prior techniques published in Redemann and Gao (2024). Retrieval uncertainties are estimated considering two independent sources: ML model fitting error and lidar measurement error. The model fitting error is quantified from the prediction error on the training dataset, while the lidar measurement error is estimated as the standard deviation of predictions from random noise perturbations added to the HALO observables. The total retrieval uncertainty is then calculated as the root-sum-square of these two error components.

4.3 Airborne Visible Infrared Imaging Spectrometer - Next Generation (AVIRIS-NG)

AVIRIS-NG is a pushbroom spectral mapping system with high signal-to-noise ratio (SNR) for high performance spectroscopy (Hamlin et al. 2011). The instrument covers the entire solar reflected spectrum from 380-2510 nm at a spectral sampling of ~5 nm. The AVIRIS-NG sensor has a 1 milliradian instantaneous field of view, providing an altitude-dependent ground sampling distance ranging from sub-meter to 20 m scales. Each acquisition is a “flightline” forming a continuous rectangular strip of data that typically takes 1-10 minutes to acquire. At altitudes flown during ARCSIX, the width of each flightline is 6-12 km; flight lines generally exceed 50 km in length.

To quantify measurement uncertainty, an input signal-dependent, three-parameter instrument noise model is applied to AVIRIS-NG at-sensor radiances (Thompson et al., 2018). The model expresses a noise-equivalent change in radiance (NedL) for each instrument channel. The most dominant type of error usually is photon noise that is assumed to be decorrelated across channels. The full-spectrum SNR can then be derived by dividing the reference radiance measurement by the respective NedL. AVIRIS-NG SNR varies as a function of wavelength, airspeed, solar angle, and surface brightness, but for the brightest targets, such as snow and cloud tops, with slow airspeed, it commonly ranged between 800 and 1000.Subsequently, the atmosphere and surface modeling approach applied to AVIRIS-NG data allows the estimation of the posterior predicted distribution that effectively expresses the uncertainty of the retrieved state at the solution (Thompson et al., 2018). It incorporates measurement errors due to random noise and resolving errors caused by a lack of resolution in the inversion process and given prior correlations between the respective reflectance product at different wavelengths. AVIRIS-NG derived surface reflectance commonly shows a posterior predictive uncertainty of 2-5%.

AVIRIS-NG measurements can be used to obtain column water vapor (Thompson et al. 2021), optical absorption paths of liquid and solid water (Bohn et al. 2020), aerosol optical depth at 550 nm (Thompson et al. 2019; Brodrick et al, 2022), spectral surface reflectance (Thompson et al. 2018), from which snow and ice spectral and broadband albedo as well as radiative forcing and flux can be derived (Painter et al. 2013). In addition, cloud top reflectance (Thompson et al. 2016), which reveals cloud thermodynamic phase (liquid, mixed, or ice) (Thompson et al. 2016; Marchant et al. 2016), Cloud Optical Thickness (COT), and Cloud Effective particle Radius (CER) (Platnick et al. 2017; Platnick et al. 2021) can be retrieved. Uncertainties of these products are generally low as shown by multiple studies that used AVIRIS-NG data as the basis for their retrievals. Thompson et al. (2021) report a standard deviation of 0.1 cm for inferred column water vapor, while Bohn et al. (2020) show that optical absorption path lengths of liquid and solid water can be estimated to within 0.07 cm uncertainty over vegetation and snow surfaces. Likewise, it has been demonstrated that downstream products specifically for snow and ice exhibit low errors when retrieved from AVIRIS-NG data. Painter et al. (2013) found uncertainties of snow broadband albedo to be less than 0.01, and those of both snow radiative forcing and snow shortwave radiative flux to not exceed 4 Wm^{-2}. More challenging is the estimation of atmospheric aerosol properties, such as the aerosol optical depth at 550 nm. Mean uncertainties range around 0.2, which sometimes refers to up to 100% relative error (Thompson et al., 2019; Brodrick et al., 2022).

https://doi.org/10.5194/essd-2026-241
Preprint. Discussion started: 24 July 2026

4.4 Vertical Atmospheric Profiling System (AVAPS)

The AVAPS, manufactured by NCAR, was used to launch Vaisala NRD-41 dropsondes (Vömel et al. 2021, 2023) from the G-III. The sondes achieved a 99.4% success rate (169/170 sondes). The average drop altitude was ~11.7 km—the G-III flight level. Typical descent times for these sondes, assuming a fall rate of ~11 m s^{-1}, was 15 min from 14 km and 8 min from 7.5 km. The NCAR Atmospheric Sounding Processing EnviroNment (ASPEN) software (V4.0.2) was used for post-processing and archiving. Data were processed in real-time and all complete profiles uploaded to Global Telemetry System (GTS) for assimilation into real-time weather forecast models. Such data ingestion is invaluable given the scarcity of observations in the study region. Data collected from the dropsondes provides a vertical profile of atmospheric measurements such as ambient temperature and pressure, dew point, and relative humidity at 2 Hz as well as GPS position (latitude, longitude and altitude) and the three-dimensional winds (u, v, and w) at a resolution of 4 Hz. Manual releases were performed using a set up similar to several recent NASA field missions including ACTIVATE (Sorooshian et al. 2023) and the Investigation of Microphysics and Precipitation for Atlantic Coast-Threatening Snowstorms (IMPACTS). The number of sondes deployed on each flight depended on the objective: 2-4 sondes deployed during a clear-sky/radiation/surface characterization flight and 8-15 sondes deployed during a cloud focussed flight.

5 Learjet instrumentation

The SPEC Learjet (Fig. 14) included a comprehensive instrument suite for measuring cloud microphysical properties like the P-3B; see Table 4 for measurement details (resolutions, uncertainties) and references describing individual instruments and data products. In addition, the Learjet carried a ProSensing Ka-Band Probe Radar-Radiometer (KPR) to provide vertical information on cloud properties and processes. Learjet flights were 3-4 hours in duration and measured within a cloud layer using a porpoising maneuver (Leg D in Fig. 4). The Learjet was only available during the summer campaign.

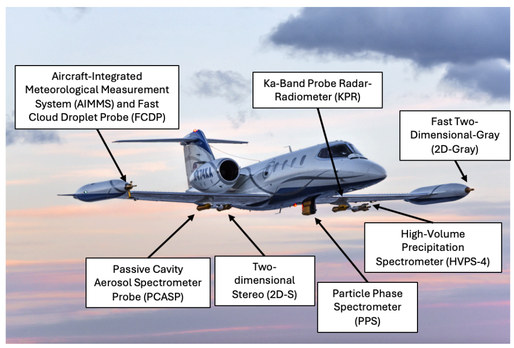

Figure 14: Learjet instrumentation configuration. (courtesy of Paul Lawson).

The SPEC Learjet instrument payload focused on detailed cloud microphysical observations. The Learjet had a M300 Series data acquisition system that obtained key navigational and atmospheric state data, including latitude/longitude, altitude, aircraft heading and total air speed, temperature, dew point temperature, static pressure, icing rod frequency, and 3-D winds. The cloud microphysical probes used were identical to those deployed on the P-3B as shown in Table 4.

The Learjet payload included a Ka-band precipitation radar (KPR) developed by ProSensing, Inc, (Pazmany and Haimov 2018). It extended in front of the wing of the Learjet and switched from zenith to nadir views at 5 Hz with interleafed short RF and linear FM pulses. A five-point, two-dimensional median filter was applied to smooth the measurements and remove clear-sky noise. It has a "deadband" that extends 150 m in both zenith and nadir directions from the aircraft. The KPR is insensitive to low concentrations of small cloud droplets (i.e., < ~ 30 µm diameter) and registers return from drizzle and ice particles that are larger than about 100 µm.

Table 4. Summary of Learjet instrumentation and measurements.

https://doi.org/10.5194/essd-2026-241
Preprint. Discussion started: 24 July 2026

Instrument	Measured Parameter	Uncertainty	Size Range (µm)	Time Resolution (s)	Reference
Navigation and State Variables					
Aventech AIMMS20AQ Dual GPS (Aircraft-Integrated Meteorological Measurement System)	Latitude, Longitude	10 m	N/A	1	Beswick et al. (2008)
Royal Air FAA RVSM Certification	Altitude	20 m	N/A	1	
Sperry Directional Gyroscope	Aircraft Heading	1°	N/A	1	
Royal Air FAA RVSM Certification	Air Speed	1 m s^{-1}	N/A	1	
Rosemount 102 Sensor	Static Temperature	0.3° C	N/A	1	Lawson and Cooper (1990)
Edgetech Chilled Mirror C-137	Dew Point Temperature	2.0° C	N/A	1	
Rosemount Icing Ord 871LM5	Icing Rod Frequency (i.e., icing rate)	N/A	N/A	1	Baumgardner and Rodi (1989); Cober et al. (2001)
Aventech AIMMS-20	Horizontal Wind Speed and Direction; Vertical Wind Speed	5° and 5 m s^{-1}; 1 m s^{-1}	N/A	1	Beswick et al. (2008)
Microphysical Variables					
SPEC Inc. Fast 2D-Gray Probe	Number concentration and size distribution, extinction, ice water content, imagery	20%	5-3005	1	
SPEC Inc. Two Dimensional Stereo (2D-S) - horizontal arm	Number concentration and size distribution, extinction, ice water content, imagery	20%	5-3005	1	Lawson et al. (2006); Woods et al. (2018)
SPEC Inc. Two Dimensional Stereo (2D-S) - vertical arm	Number concentration and size distribution, extinction, ice water content, imagery	20%	5-3005	1	Lawson et al. (2006); Woods et al. (2018)
SPEC Inc. Fast Cloud Droplet Probe (FCDP)	Number concentration and size distribution, extinction, liquid water content	50%	1.5-50	1	Knollenberg (1981); Lawson et al. (2017)
SPEC Inc. High Volume Precipitation Spectrometer (HVPS4) - vertical 150µm arm	Number concentration and size distribution, extinction, ice water content, imagery	15%	75-45075	1	Woods et al. (2018)
SPEC Inc. High Volume Precipitation Spectrometer (HVPS4) - horizontal 150µm arm	Number concentration and size distribution, extinction, ice water content, imagery	15%	75-45075	1	Woods et al. (2018)
SPEC Inc. High Volume Precipitation Spectrometer (HVPS4) - vertical 50µm arm	Number concentration and size distribution, extinction, ice water content, imagery	15%	25-15025	1	Woods et al. (2018)
SPEC Inc. High Volume Precipitation Spectrometer (HVPS4) - horizontal 50µm arm	Number concentration and size distribution, extinction, ice water content, imagery	15%	25-15025	1	Woods et al. (2018)
SPEC Inc. Particle Phase Spectrometer (PPS) - Fast 2D-Gray	Number concentration and size distribution, extinction, ice water content, imagery	20%	2.5-1502.5 µm	1	
SPEC Inc. Particle Phase Spectrometer (PPS) - CPI imaging component	Imagery		0.73-800 µm		
Sky Tech Nevzorov LWC/TWC	Liquid and total water content	0.1 g cm^{-3}			Korolev et al. (1998)
Radar					

https://doi.org/10.5194/essd-2026-241
Preprint. Discussion started: 24 July 2026

ProSensing Ka-Band Probe Radar-Radiometer (KPR)	Vertical profiles of reflectivity and Doppler velocity	N/A	Pazmany and Haimov (2018)

6 Ground-based Observations

6.1 Sea ice buoy Array

The SIMB buoy array was composed of nine buoys (SIMB3; Polashenski et al. 2011; Planck et al. 2019; Fig. S2) deployed in the Lincoln Sea ~1 month before ARCSIX RF1 and were routinely overflown during the campaign. The buoys are named alphabetically, J-R, in the order they were activated. Initial positions and drift tracks are shown in Fig. 1. Each buoy contains a downward facing acoustic rangefinder to measure the position of the sea ice/snow surface, an upward facing acoustic rangefinder mounted to measure ice bottom position, downwelling and upwelling SW radiation instruments, a barometric pressure sensor, air temperature sensor, and a digital temperature string. The digital temperature string was 1.6 m in length with measurements provided at a 0.02 m spacing extending to ~60 cm deep into the sea ice. SW radiation was measured using an upward and downward looking Apogee pyranometers (SP-510 & SP-610, respectively). Initial snow depth and ice thickness measurements were made at installation. Four of the buoys (L, O, P, R) include Snow Thickness and Temperature Observation System (SnowTATOS), a low-cost, autonomous system for snow depth measurements on sea ice. Instantaneous measurements are reported every 4 hours and data are archived at the Arctic Data Center (Polashenski et al. 2024; Raphael et al. 2025).

6.2 Thule High Arctic Atmospheric Observatory (THAAO)

The Thule High Arctic Atmospheric Observatory (THAAO) is located on South Mountain (Akinnaarssuaq; elev. 220 m asl) at 76.51° N and 68.74° W THAAO houses a suite of instruments devoted to the observation of the Arctic atmosphere and radiation budget. Details of the instruments operating at THAAO during ARCSIX and the parameters observed are summarized in Table 5 and Figure S2. The datasets collected at THAAO are available for download from the web portal (https://www.thuleatmos-it.it).

During ARCSIX, THAAO conducted additional measurements to facilitate combined airborne studies. Radiosonde launches were routinely performed, at least daily, and made available on the GTS for assimilation. Lidar acquisitions provide vertical profiles of aerosol backscattering and extinction coefficients. The Solar Radiation Group of the University of Valencia deployed a zenith spectrometer (TWST; Niple et al. 2016) and a calibrated RGB all-sky imager at THAAO, improving aerosol-cloud observations (Valdelomar et al. 2021; Gómez-Amo et al. 2025). Four aircraft overpasses of THAAO were conducted during ARCSIX by the P-3 (2024-5-30, 2024-0606, and 2024-06-10, and 2024-08-01) and by the G-III (2024-06-10). These overpasses enable intercomparisons and radiative closure studies under both clear-sky and cloudy conditions.

Ground-based single particle measurements of refractory black carbon (rBC) were also collected at THAAO with an Extended Range Single Particle Soot Photometer (SP2-XR) continuously from 2024-06-19 through 2024-09-29. The SP2-XR directly measured attributes of incandescent particles, such as refractory black carbon, and scattering particles, such as dust. The instrument yielded 1-minute resolution data for variables including the concentrations, masses, and volume-weighted diameters of these particles, and equivalent coating thickness (ECT). In addition, daily surface concentrations of biomass burning smoke, dust, and anthropogenic and biogenic fine aerosols (ABF) were extracted from global simulations of the Navy Aerosol Analysis and Prediction System Reanalysis (NAAPS-RA) to categorize specific days into high or low smoke and dust deposition events

https://doi.org/10.5194/essd-2026-241
Preprint. Discussion started: 24 July 2026

and to track air mass origins and confirm whether elevated particle levels resulted from long-range transport (e.g., from Canada) or local contamination (Khan et al., 2017; Khan et al., 2023; Xian et al., 2022).

Table 5. Summary of instrumentation with DOIs available at THAAO during 2024.

Instrument [Company (Model)]	Measured / Retrieved Parameter	Altitude (km) [min – max]	Resolution [Time / Vert]	Reference [dataset]
Weather - Surface				
Automatic Weather Station [Campbell Scientific]	Pressure, Temperature, Relative Humidity, Wind, Snow Height	sfc	1 min / —	Ciardini et al. (2026)
Atmosphere - Vertical Profile / Column integrated				
Ceilometer [LUFFT (CHM 15k Nimbus)]	Cloud Cover, Base Height and Geometrical Depth	0.1 – 15	15 s / 15 m	Di Iorio et al. (2022)
Radiosondes [Vaisala (RS92 / RS41)]	Pressure, Temperature, Relative Humidity, Wind	0.005 – 20	~60 min / ~5 m	Muscari et al. (2026)
Microwave Radiometer [RPG (HATPRO G2)]	IWV, LWP	Column	1 s / —	Pace et al. (2023b); Pace et al. (2023c)
NASA AERONET [Cimel (CE318-T)]	AOD	Column	5 min / —	Holben et al. (1998); Giles et al. (2019)
VESPA-22 Spectrometer [in-house developed]	IWV	Column	15 min / —	Muscari et al. (2018a)
VESPA-22 spectrometer [in-house developed]	Water Vapour Profiles	25 – 75	6 h / 7–10 km	Muscari et al. (2018c)
Broadband and Spectral Radiation - Surface				
Pyranometer _dn [Kipp&Zonen (CMP21)]	Downwelling SW irradiance	sfc	30 s / —	Meloni et al. (2026a)
Pyrgeometer_dn [Kipp&Zonen (CGR4)]	Downwelling LW irradiance	sfc	30 s / —	Meloni et al. (2026a)
Pyranometer_up [Eppley (PSP) / Kipp&Zonen (CMP21)]	Upwelling SW irradiance	sfc	30 s / —	Meloni et al. (2026b)
Pyrgeometer_up [Eppley (PIR) / Kipp&Zonen (CGR4)]	Upwelling LW irradiance	sfc	30 s / —	Meloni et al. (2026c)
Pyrometer [Heitronics II (KT 19.85)]	Infrared Sky Brightness Temperature	sfc	30 s / —	Pace et al. (2023a)
Atmospheric Composition - Surface				
Droplet Measurement Technology (DMT) Single Particle Soot Photometer – Extended Range	Refractory black carbon concentrations, average and volume-weighted diameters of the particles, equivalent coating thickness (ECT) and total coating metrics	5 m	1 min / —	Khan and Peng (2026)
Sky Imagers - Surface				
All-sky-camera [Moonglow Tech]	Sky Images – Visible (jpg)	sfc	1 min / —	Meloni et al. (2026c)

https://doi.org/10.5194/essd-2026-241
Preprint. Discussion started: 24 July 2026

7 Complementary data products

7.1 Flight reports

Each flight and aircraft has an archived flight report drafted by the flight scientist and available a resource for data users to learn about the context and special features of a particular flight. Users should consult these for context only and rely on the final data process to confirm the details within the reports.

7.2 Aircraft collocation viewer and data map

The ARCSIX collocation viewer (https://konradsebastian.github.io/arcsix-datamap/collocations.html), is an interactive map visualizing the coordinated sampling geometry of the ARCSIX campaign. The viewer displays the flight tracks of the NASA P-3B, NASA G-III, and SPEC Learjet as geolocated lines, allowing user to identify aircraft-aircraft collocations such as 'wall' maneuvers, including their timing. Satellite underpass segments from EarthCARE (ATLID, CPR, MSI), PACE (HARP2, OCI, SPEXone), and PREFIRE are overlaid as time-tagged events; overflight times at the ground-based stations Alert, Qaanaaq (QNQ), Pituffik/Thule (THAAO), and Villum are indicated by markers. Aircraft-to-aircraft collocations are displayed as a separate event type. The user selects a flight date from a tabbed date index, then filters the display by aircraft, satellite sensor, ground station, and event type using interactive toggle controls. The map enables rapid visual assessment of which aircraft, satellite, and ground-based observations are available and how closely they are coordinated. Once the user identifies a period of event of interest, they can go on to the data map and archive to find the relevant data. To visualize the timing of the flights as video sequences, we instead refer the data user to the flight animations in the ARCSIX Story Map (https://storymaps.arcgis.com/stories/916e1291bd99487c97b06ed5895897da).

The ARCSIX data map (https://konradsebastian.github.io/arcsix-datamap) is a web-based reference page providing a single-entry point to all instruments, datasets, and data archives from the ARCSIX 2024 airborne campaign and related activities to aid in data access. Instruments and datasets are organized by platform (NASA P-3B, NASA G-III, SPEC Learjet, surface networks, and satellite/model datasets). Each entry lists the instrument description, key measured variables and associated uncertainties, the responsible PI, and direct links to the dataset DOI and the NASA ASDC/EarthData archive. Entries for datasets still pending public release are flagged accordingly, and the page is updated as new collections become available. In addition to the instrument inventory, the page hosts PI presentations from the 2025 ARCSIX Data Workshop, allowing users to review concise oral introductions to each instrument. Reader code and analysis software, where available, are also linked from the respective instrument entries. The data map is intended as the recommended first stop for users seeking to locate, assess, or download any ARCSIX data.

7.3 Coupled Arctic Forecast System (CAFS)

Adapted from the Regional Arctic System Model (RASM; Maslowski et al. 2012; Cassano et al. 2017), the Coupled Arctic Forecast System (CAFS; Solomon et al. 2024) provides regional-scale weather forecasts within the Arctic region by coupling dynamical ocean, sea ice, land, and atmospheric models. CAFS initial conditions are taken from the 0000 UTC NOAA GFS deterministic atmosphere forecast, satellite-derived sea ice concentration (SIC), and the NOAA day/night blended satellite sea surface temperature product (Maturi et al. 2017). A sea ice thickness product from the European Space Agency's Cryosat-2 satellite (Tilling et al. 2018) was used to initialize the model in spring 2018 and has been running cycled thereafter. Three-hourly GFS forecasts are used as lateral boundary conditions.

https://doi.org/10.5194/essd-2026-241
Preprint. Discussion started: 24 July 2026

CAFS was a key source of forecast information used for ARCSIX flight planning. Regional forecast products were provided for the sea ice off the north and northeastern coast of Greenland. In addition to standard maps, novel model diagnostics were developed from the 10-day forecasts and made available for flight planning and are available to support data analysis (Colarco and Solomon 2026).

7.4 GEOS-FP aerosol and meteorological forecasts

The NASA Goodard Earth Observation System-Forward Processing (GEOS-FP) Earth system model was used to provide near-real-time 12.5 km resolution aerosol and meteorological forecasts and assimilation products during the campaign (Lucchesi 2018; Colarco and Solomon 2026) (https://gmao.gsfc.nasa.gov/gmao-products/geos-near-real-time-data-products/). Data were made available to the team in a dedicated portal (https://fluid.nccs.nasa.gov/missions/mission_ARCSIX/), providing aerosol concentrations and meteorological conditions at specific buoy, ship, and ground-station locations. Aerosol fields for dust, sea salt, sulfate, nitrate and carbonaceous aerosols were produced online and radiatively coupled in GEOS-FP using the Goddard Chemistry Aerosol Radiation and Transport (GOCART) module (Colarco et al. 2010). Aerosol optical depth is assimilated in GEOS-FP and GMAO reanalysis products (see below) as in Randles et al. (2017).

GEOS-FP aerosol forecasts have not been thoroughly validated in the Arctic. However, validation data for the Modern-Era Retrospective analysis for Research and Applications, Version 2 (MERRA-2) aerosols is available, providing some insight into the model's performance (Randles et al. 2017; Buchard et al. 2017; Zamora et al. 2022; Vinogradova et al. 2020; Wu et al. 2020; Xian et al. 2022; Zhuravleva et al. 2020). Aerosol information to support ARCSIX data analysis is also available from the more recent GEOS-IT global reanalysis at 50 km resolution (https://gmao.gsfc.nasa.gov/gmao-products/geos-it/), including the assimilation of satellite observed aerosol optical depth similar to MERRA-2. Through ARCSIX, local dust emissions are currently being added in GEOS research model runs and will be available soon in the ARCSIX data archive alongside the GEOS-FP products extracted along the ARCSIX flight tracks.

7.5 FLEXPART Atmospheric transport modelling for a moving receptor (black carbon and dust)

Long-range transport of BC and dust during the ARCSIX campaign was examined using the Lagrangian particle dispersion model FLEXPART version 10.4 (Pisso et al. 2019). FLEXPART was driven by hourly meteorological fields from the European Centre for Medium-Range Weather Forecasts (ECMWF) Reanalysis v5 (ERA5), (Hersbach et al. 2020). Particles were released at the exact height of the moving receptor (G-III, Learjet, P-3 flight lines) and tracked backward in time for 30 days, (Bond et al. 2013; Kok et al. 2017). Footprint emission sensitivity (FES) expresses the probability of gridded emissions to reach the receptor and can be converted to modelled concentration at the position of the airplane, if coupled with an emission inventory (Popovicheva et al., 2025). Concentrations are given (a) as a function of time elapsed since the emission has occurred (age spectrum), showing if the aerosol is fresh or aged, (ii) as a function of the continental contribution (continent spectrum), if masked for specific regions/continents, and (c) as a function of different sectoral emissions (source spectrum), such as those that are usually defined in bottom-up emission inventories (Evangeliou et al. 2026).

Anthropogenic emissions were adopted from the latest version (v6b) of the Evaluating the CLimate and Air Quality ImPacts of ShortlivEd Pollutants (ECLIPSE) dataset (Klimont et al. 2017). Emission sectors in ECLIPSE include industrial combustion (IND), residential and commercial emissions (DOM), energy production sector (ENE), transportation (TRA), emissions from waste treatment and disposal sector (WST), shipping emissions (SHP) and gas flaring emissions (FLR) (Böttcher et al. 2021). Wildfire emissions were adopted from the Copernicus Global Fire Assimilated System (CAMS GFAS) (Kaiser et al. 2012).

https://doi.org/10.5194/essd-2026-241
Preprint. Discussion started: 24 July 2026

Dust emissions were computed at 3-hourly time resolution at 0.25° resolution using the FLEXDUST module (Ginoux et al. 2001; Groot Zwaaftink et al. 2016; Groot Zwaaftink et al. 2022). Emissions for 10 different particle sizes for dust with diameters 0.2 – 20 µm were calculated in the products. FLEXPART simulation outputs for black carbon are available at https://atmo-access.nilu.no/ARC6_BC.py and for dust at https://atmo-access.nilu.no/ARC6_DUST.py (Evangeliou et al. 2026).

7.6 CERES FM2 scans and CRS

The Clouds and the Earth's Radiant Energy System (CERES) project provided special data products to support ARCSIX. The Terra-FM2 instrument was operated in programmable azimuthal plane scan (PAPS) mode from 2024-05-24 through 2024-06-17 and from 2024-07-22 through 2024-08-24. PAPS mode targeted a predetermined location during an overpass to gather measurements at a broader set of viewing geometries (Fig. 15) to explore the angular variations in the radiative fluxes. The center buoy location (Buoy L) and its drift were used to determine the focal point of the scanning. To accomplish the scanning pattern, the azimuth angle of the instrument scan is changed after each zenith scan and is stopped at nadir (θ = 0°) during the operation. An important note for data users is that the footprint size increases substantially from ~20 km^2 at nadir to > 50 km^2 at larger view zenith angles. The Bidirectional Scan data (L1B) and the Single Scanner Footprint (SSF) radiative fluxes, clouds, and aerosols for these scans are archived (NASA 2025a).

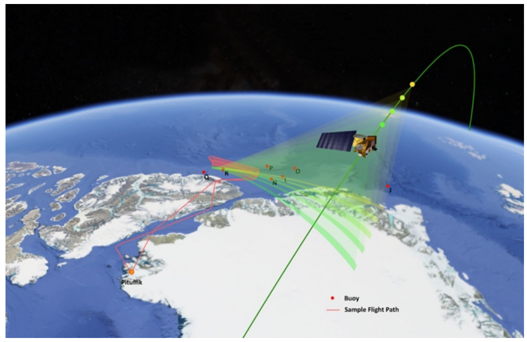

Figure 15: Schematic of CERES FM2 scan centered on the buoy L during the RF3, 31 May. (Courtesy of Janet Daniels)

The CERES team also provided a L2 Cloud Radiative Swath (CRS) Ed4 data product for the ARCSIX period. The CRS data set extends the L2 SSF radiative flux data by computing radiative fluxes at the instantaneous footprint scale using the NASA Langley Fu–Liou Radiative Transfer Model (Fu and Liou 1993; Kratz and Rose 1999; Kato et al. 1999, 2005). The CRS Ed4 framework is used for radiative closure studies, the evaluation of cloud and aerosol retrievals, and to understand changes in the input datasets used in other data products (Rutan et al. 2015; Loeb et al. 2018; Kato et al. 2018). The CRS data product is provided for the cross-track scanning CERES Terra FM1 and Aqua FM3 instruments (NASA 2025b,c,d).

7.7 Ice, Cloud, and land Elevation Satellite-2 (ICESat-2)

NASA's Ice, Cloud, and land Elevation Satellite-2 (ICESat-2; Neumann et al. 2019) provides high-resolution laser altimetry measurements used to retrieve critical surface properties, including sea ice freeboard and roughness. During the first phase of the ARCSIX campaign, an intense solar storm forced ICESat-2 into a safe-hold mode, resulting in a gap in science data collection between 20024-05-10 and 2024-06-21. Nominal science operations resumed on 2024-06-21, allowing for the successful acquisition of high-quality data throughout the second half of the campaign.

The mean sea ice freeboard during this active period, derived from the ATL20 gridded product, is presented in Fig. 16a. These regional satellite observations provide essential surface characterization that when combined with localized ARCSIX measurements, are crucial for accurately retrieving sea ice thickness. To facilitate the direct validation of these satellite retrievals, the NASA P-3B aircraft conducted a targeted under flight of ICESat-2 along Reference Ground Track (RGT) 704 on 2024-08-

https://doi.org/10.5194/essd-2026-241
Preprint. Discussion started: 24 July 2026

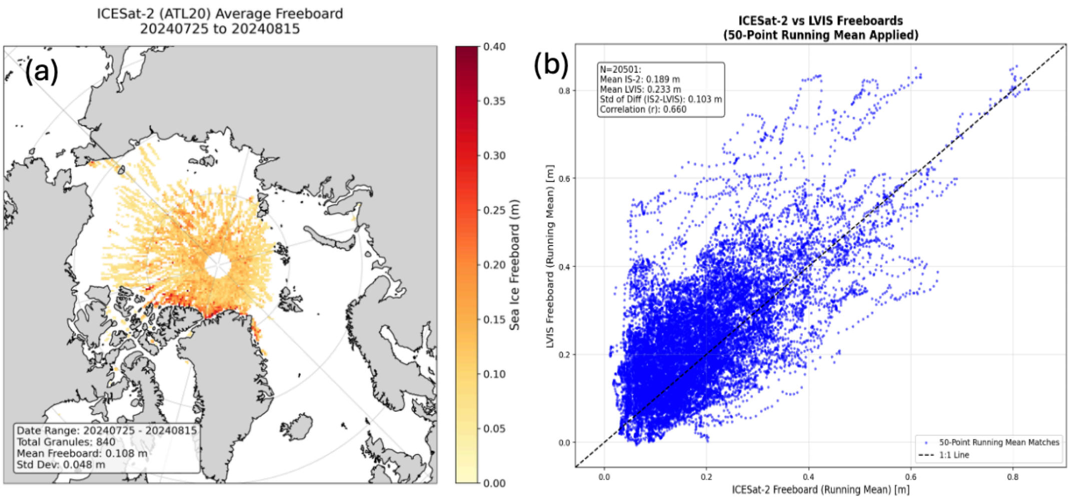

Figure 16: Average (a) ICESat-2 freeboard (units: m) during from July 25-August 15, 2015 and (b) comparison of LVIS-derived freeboard (y-axis) and ICESat-2 free-bard (x-axis) for the RF15 underflight. Courtesy of Nathan Kurtz.

02. Figure 16b shows the initial comparison between IceSat-2 and LVIS freeboard applying a 50-point running mean to the LVIS data to account for time differences; the results show good agreement between the two measurements. Further comparison and analysis of the IceSat-2 and LVIS freeboard comparison is the subject of forthcoming paper.

7.8 Surface Stations

Long-term surface aerosol measurements and weather stations of greatest relevance to ARCSIX include the AERONET stations at Eureka (ØPAL), Pituffik (Thule), Alert, and Svalbard (Hornsund and Ny-Ålesund), THAAO at Pituffik (discussed in Section 6b), the Villum Research Station near Station Nord, and additional research observations at Eureka, Alert, SIGMA-B, and Ny-Ålesund. During the deployment, ARCSIX collaborated with the CLeancloud Arctic VIllum ExpeRiment (CLAVIER) field campaign, which took place (2024-07-15 through 2024-08-15) at the Villum Research Station at the northeastern tip of Greenland. In addition to the standard instrumentation at Villum, which includes a Scanning Mobility Particle Sizer (SMPS), a Cloud Condensation Nuclei Counter (CCN-100), a High-Volume Sampler (HVS), a Nephelometer, an Aethalometer, a Neutral cluster and Air Ion Spectrometer (NAIS), a wind lidar and a ceilometer, CLAVIER incorporated several additional instruments, including an AeRosol aerosol-cloud lIdar System (ARIS lidar), a Wideband Integrated Bioaerosol Sensor (WIBS-5/NEO), a Proton-Transfer-Reaction Mass Spectrometry (PTR-MS), a white-light aerosol spectrometer (WELAS), and the newest aethalometer (AE36s).

Several ships of opportunity operated in the high Arctic around the time of the ARCSIX summer campaign, including the Oceania (2024-06-11 through 2024-08-11), the Kronprins Haakon (2024-06-21 through 2024-08-03), the Oden (2024-08-07 through 2024-09-15), and the Polarstern (2024-08-10 through 2024-08-25), each carrying MicroTops aerosol sun photometers (https://aeronet.gsfc.nasa.gov/new_web/maritime_aerosol_network_v3.html) and a broad range of weather, sea ice, and oceanographic measurement instrumentation. Oden at this time was in the Nares Strait as part of GEOEO 2024 expedition (https://www.polar.se/en/expeditions/previous-expeditions/arctic/geoeo-north-of-greenland-2024/). Onboard atmospheric instrumentation included a W-band cloud radar, microwave radiometer, ceilometer and a radiosounding station with 12-hourly weather balloon releases. The data products from these systems are combined to produce the CloudNet classification product

https://doi.org/10.5194/essd-2026-241
Preprint. Discussion started: 24 July 2026

Open Access Earth System Science Data Discussions

(Illingworth et al., 2007). Additional instrumentation included surface turbulent and radiative flux systems and comprehensive surface meteorology. Quality controlled data from the GEOEO expedition are published at the Bolin Centre data repository (https://bolin.su.se/data, search term "GEOEO").

ARCSIX overflew the Oden several times during the summer campaign (2024-08-07, 2024-08-08, 2024-08-15 August), twice overflew ØPAL (2024-08-07, 2024-08-09 August), SIGMA-B (2024-07-29, 2024-07-30), Villum (2024-06-13 and 2024-08-01), and THAAO (2024-05-30, 2024-06-06 and 2024-06-10, and 2024-08-01), and flew near or over Alert nearly every day. Additional information, including principal investigators and links to data from some of these sources is available under the "ARCSIX Collaborator Data" link at https://earthdata.nasa.gov/s3fs-public/2026-04/ARCSIX%20Collaborator%20Data.pdf?VersionId=d2XKaWn21Wc_E0ZDWARbk48zr_X3pu6e.

7.9 Alfred Wegener Institute (AWI) IceBird Airborne Campaign

The Alfred Wegener Institute (AWI) Institute for Polar and Marine Research IceBird program is a series of airborne surveys undertaken to profile changing sea ice conditions in the western Arctic, typically in both spring and summer. The IceBird summer campaigns provide insight into the composition of the ice thickness (Belter et al., 2021), surface roughness (Krumpen et al. 2025) and melting state (Buth et al. 2025) change over time and support satellite product validation (Landy et al. 2022). The main payloads on IceBird Summer are: the EM-bird instrument for sea ice thickness, a Riegl VQ580 laser scanner for sea ice roughness and freeboard, and a Modular Aerial Camera System (MACS) multi-camera (RGB, NIR, TIR) for melt ponds and documenting general ice conditions (https://www.awi.de/en/science/climate-sciences/sea-ice-physics/projects/ice-bird.html). In 2024, eight summer surveys were made from Station Nord, Greenland, with the AWI Polar 5 DC-3 aircraft, between 2024-07-26 and 2024-08-07, for measurements covering an along-track distance of approximately 3700 km (Fig. S3; Landy et al. 2026a). These flights profiled sea ice between the Lincoln Sea and north of Fram Strait, coordinating directly on several occasions with ARCSIX activities. On 2024-07-31, a survey through the Lincoln Sea overflew ARCSIX buoys N, L, and O. On 2024-08-01, a survey north of Station Nord followed two legs of a survey covered by the ARCSIX aircraft at approximately the same time. This was while a flaw lead, with a width up to 200 km, opened between the north coast of Greenland and the ice covered in the survey. On 2024-08-02, a survey was coordinated with ARCSIX flights over the Lincoln Sea. An example of the profile and distribution of sea ice thickness recorded by the EM-bird on the 2024-07-31 IceBird survey between Nares Strait and 85N is shown in Figure S3, including thicker >2 m ice around 100 km north of Nares Strait and then ice of ~1.5 modal thickness over the ARCSIX buoys.

7.10 On-ice Micro-Met Stations

A set of eight micro-met stations (Fig. S4) from the Arctic University of Norway (UiT) were deployed on sea ice in 2024-04 and 2024-05, each station in conjunction with one of the ARCSIX IMB deployments (SIMB3_2024J, K, L, M, N, O, Q, R). The stations included a MaxiMet GMX560 Marine sensor recording air temperature, humidity and pressure, wind speed and direction from a sonic anemometer, GPS location, and compass direction, on 30-minute intervals. Stations were powered with a 6V lead-acid battery recharged by an external solar panel and lasted up to the end of 2024-09. Measurements were transmitted with Iridium telemetry and are available at https://data.npolar.no/dataset/9b81d93d-17da-4dfd-a9b5-7aec2a3cb234 (Landy et al. 2026b).

https://doi.org/10.5194/essd-2026-241
Preprint. Discussion started: 24 July 2026

8 Conclusions

This paper describes a collection of airborne, satellite, and ground-based datasets central to achieving ARCSIX science. ARCSIX was based in Pituffik, Greenland (76.53N and 68.82W), spanning 2024-05-28 through 2024-08-15 and sampled the Baffin Bay, Canadian Archipelago, to the north and northeast Greenland coast, and the Lincoln Sea regions. This manuscript provides an overview of the general characteristics of the ARCSIX campaign, locations of the data, notes on data usage, and points to available code developed by the ARCSIX team to support analysis, serving as a resource for studies using the ARCSIX dataset. The ARCSIX mission constitutes the most comprehensive dataset of simultaneous sea ice properties, radiation, clouds, aerosol particles, and atmospheric chemistry measurements collected in the high Arctic. The ARCSIX dataset enables novel investigations of the form and function of surface-atmosphere coupling processes within the Arctic and critical improvements in the interpretation of satellite remote sensing data that are needed to advance understanding of the rapidly evolving Arctic.

Appendix A: Summary of abbreviations

Abbreviation	Definition
ØPAL	Zero Altitude PEARL Auxiliary Laboratory
2D-Gray	Fast Two-Dimensional-Gray
2D-S	Two-dimensional (2-D) stereo
A-ATOFMS	Aircraft Aerosol Time-of-Flight Mass Spectrometer
ACCACIA	Aerosol-Cloud Coupling and Climate Interactions in the Arctic
ACLOUD	Arctic Cloud Observations Using airborne measurements during polar Day
ACTIVATE	Aerosol Cloud meTeorology Interactions oVer the western ATlantic Experiment
ADL	Airborne Doppler Lidar
AERONET	Aerosol Robotic Network
AFLUX	Airborne measurements of radiative and turbulent Fluxes in the cloudy atmospheric boundary layer
ALP	Active Leveling Platform
AOD	Aerosol Optical Depth
AIMMS	Aircraft-Integrated Meteorological Measurement System
APS	Aerodynamic Particle Sizer
ARCSIX	Arctic Radiation Cloud aerosol Sea ice Interaction eXperiment
ASCOS	Arctic Summer Cloud Ocean Study
ASDC	Atmospheric Science Data Center
ASPEN	Atmospheric Sounding Processing EnviroNment
ARISE	Arctic Radiation Icebridge Sea ice Experiment)
ASTAR	Arctic Study of Tropospheric Aerosol, Clouds and Radiation
AVIRIS-NG	Airborne Visible Infrared Imaging Spectrometer - Next Generation
AWI	Alfred Wegener Institute
BASE	Beaufort and Arctic Storms Experiment BASE
BBR	BroadBand Radiometer Suite
BC	Black Carbon
BGTL	Pituffik Space Base

https://doi.org/10.5194/essd-2026-241
Preprint. Discussion started: 24 July 2026

BRDF	Bidirectional Reflectance Distribution Function
CAESAR	Cold Air Outbreak Experiment in the Sub-Arctic
CAFS	Coupled Arctic Forecast System
CAMP^{2}Ex	Cloud, Aerosol and Monsoon Processes Philippines Experiment
CAMS GFAS	Copernicus Global Fire Assimilated System
CCD	Charge-Coupled Device
CCN	Cloud Condensation Nuclei
CCN	Cloud Condensation Nuclei Counter
CCSEM-EDX	Computer-Controlled Scanning Electron Microscopy-Energy Dispersive X-ray
CER	Cloud Effective particle Radius
CERES	Clouds and the Earth's Radiant Energy System
CFDC-1H	Continuous Flow Diffusion Chamber 1H
CICE5	Community Ice Model 5
CLAVIER	CLeancloud Arctic VIllum ExpeRiment
CLM	Community Land Model
COMBLE	Cold-Air Outbreaks in the Marine Boundary Layer Experiment
COT	Cloud Optical Thickness
CPC	Condensation Particle Counters
CPI	Cloud Particle Imager
CRREL	Cold Regions Research and Engineering Laboratory
CRS	Cloud Radiative Swath
CVI	Counterflow Virtual Impactor
CYYR	Goose Bay, Canada
DAS	Data Assimilation System
DIAL	DIfferential Absorption Lidar
DLH	Diode Laser Hygrometer
DLH-SP	Diode Laser Hygrometer-short path
EnMAP	Environmental Mapping and Analysis Program
DOM	Residential and Commercial Emissions
EarthCARE	Earth Cloud Aerosol and Radiation Explorer
ECLIPSE	Evaluating the CLimate and Air Quality ImPacts of ShortlivEd Pollutants
EMSL	Environmental Molecular Sciences Laboratory
ENE	Energy Production Sector
F2D-S	Fast Two-dimensional (2-D) stereo
f(RH)	aerosol scattering enhancement factor
FATES	Flexible Analysis Toolkit for the Exploration of SPMS data
FCDP	Fast Cloud Droplet Probe
FES	Footprint Emission Sensitivity
FIMS	Fast-Integrated Mobility Spectrometer

https://doi.org/10.5194/essd-2026-241
Preprint. Discussion started: 24 July 2026

FIRE-ACE	First International Satellite Cloud Climatology Project (ISCCP) Regional Experiment-Arctic Cloud Experiment
FLEXPART	FLEXible PARTicle LaGrangian particle dispersion model
FLR	Gas Flaring Emissions
FPA	Focal Plane Array
GEOEO	Greenland Earth-Ocean-Ecosystem Observatory
GEOS-FP	Goddard Earth Observing System-Forward Processing
G-III	Gulfstream III
GFS	Global Forecast System
GMAO	Global Modeling and Assimilation Office
GOCART	Goddard Chemistry Aerosol Radiation and Transport
GPS	Global Positioning System
GTS	Global Telemetry System
GVR	G-Band Vapor Radiometer
HALO	High-Altitude Lidar Observatory
HDF5	Hierarchical Data Format
HR-ToF-AMS	High-Resolution Time-of Flight Aerosol Mass Spectrometer
HSR1	Hyper-Spectral Radiometer
HSRL	High Spectral Resolution Lidar
HVPS-4	High-Volume Precipitation Spectrometer
HVS	High-Volume Sampler
ICAP	International Cooperative for Aerosol Prediction
ICARTT	International Consortium for Atmospheric Research on Transport and Transformation
ICESat-2	Ice, Cloud, and land Elevation Satellite-2
IMPACTS	Investigation of Microphysics and Precipitation for Atlantic Coast-Threatening Snowstorms
IND	Industrial combustion
INP	Ice Nucleating Particle
INS	Inertial Navigational System
ISDAC	Indirect and Semi-Direct Aerosol Campaign
KBTV	Burlington, VT
KBGR	Bangor, ME
KLFI	NASA Langley Research Center
KPR	Ka-Band Probe Radar-Radiometer
KWAL	NASA Wallops Flight Facility
LARGE	Langley Aerosol Research Group Experiment
LOD	Limits Of Detection
LPM	Liters Per Minute
LSR	Lidar Scattering Ratio
LVIS	Land, Vegetation, and Ice Sensor
LW	Longwave

https://doi.org/10.5194/essd-2026-241
Preprint. Discussion started: 24 July 2026

LWP	Liquid Water Path
M-PACE	Mixed-Phase Arctic Cloud Experiment
MACS	Modular Aerial Camera System
MAN	Maritime Aerosol Network
MARLi	Multi-functional Airborne Raman Lidar
MERRA-2	Modern-Era Retrospective analysis for Research and Applications, Version 2
MPL	Micro-Pulse Lidar Network
MPS-3	3-stage Microanalysis Particle Sampler
MOSAiC-ACA	Multidisciplinary drifting Observatory for the Study of Arctic Climate – Airborne observations in the Central Arctic)
NAIS	Neutral cluster and Air Ion Spectrometer
NASA	National Aeronautics and Space Administration
NASCENT	Ny-Ålesund Aerosol Cloud Experiment
NCAR	National Center for Atmospheric Research
NCCS	NASA Center for Climate Simulation
NMASS	Nuclei-Mode Aerosol Size Spectrometer
NOAA	National Oceanic and Atmospheric Administration
NPF	New Particle Formation
OC	Organic Carbon
O-PTIR	Optical-PhotoThermal InfRared
PAMARCMiP	Polar Airborne Measurements and Arctic Regional Climate Model Simulation Project
PAMTRA	Passive and Active Microwave TRAnsfer
PAPS	Programmable Azimuthal Plane
PCASP	Passive Cavity Aerosol Spectrometer Probe
PCI	Pressure Controlled Inlet
PNII	Passive Near-Isokinetic Inlet
POP2	Parallel Ocean Program
POPS	Printed Optical Particle Spectrometer
PPS	Particle Phase Spectrometer
PRISMA	Hyperspectral Precursor and Application Mission
PSAP	Particle Soot Absorption Photometer
PTR-MS	Proton-Transfer-Reaction Mass Spectrometry
PUTLS	Particles in the Upper Troposphere, Lower Stratosphere
RASM	Regional Arctic System Model
RF	Research Flight
RH	Relative Humidity
RSP	Research Scanning Polarimeter
SIC	Sea Ice Concentration
SHP	Shipping Activities
SIMB	Sea Ice Mass Balance Buoy

https://doi.org/10.5194/essd-2026-241
Preprint. Discussion started: 24 July 2026

Open Access Earth System Science Data Discussions

SMPS	Scanning Mobility Particle Sizer
SNR	Signal-to-Noise Ratio
SOOT	Sub-Orbital Order Tool
SPEC	Stratton Park Engineering Company
SPN1	Sunshine Pyranometer
SQ	Science Question
SSA	Single Scattering Albedo
SSH	Sea Surface Height
SSFR	Solar Spectral Flux Radiometer
SSRR	Solar Spectral Radiance Radiometer
STAC	Size and Time-resolved Aerosol Collector
SW	Shortwave
SWIR	ShortWave InfraRed
TAMMS	Turbulent Air Motion Measurement System
TBD	To Be Determined
T_bs	Sky Brightness Temperatures
TEM	Transmission Electron Microscopy
THAAO	Thule High Arctic Atmospheric Observatory
TRA	Transportation
TWC	Total Water Content
UHSAS	Ultra-High Sensitivity Aerosol Spectrometer
WFOV	Wide Field-Of-View
WIBS	Wideband Integrated Bioaerosol Sensor
WELAS	White-Light Aerosol Spectrometer
WMO	World Meteorological Organization
WRF	Weather and Research and Forecasting
WST	Waste Treatment and Disposal Sector
WVP	Water Vapor Path

Code and Data Availability

NASA's Atmospheric Science Data Center (ASDC) is responsible for data curation, dissemination, and long-term preservation of ARCSIX data. It archives the latest versions of publication-quality data, including observational, derived, and value-added data products. It also houses contextual information to facilitate data use by the research community, in addition to documentation for maintaining reprocessing capability and openness. Digital object identifiers (DOIs) are assigned at both the project level and data products (collection) level for ARCSIX.

All data from the P-3B, G-III, and Learjet, unless otherwise stated, are publicly archived on ASDC's Distributed Active Archive Center (http://doi.org/10.5067/SUBORBITAL/ARCSIX/DATA001) and are accessible via the ARCSIX landing page (https://www.earthdata.nasa.gov/data/projects/arcsix last access: 08 May 2026), with each data file containing data from one flight or one calendar day. Various tabs on the web page include different data products (collections) and unique DOI codes. An

https://doi.org/10.5194/essd-2026-241
Preprint. Discussion started: 24 July 2026

open-data workshop was held to help new ARCSIX data users; recordings of these presentations are available. Data can also be accessed using a free account at https://earthdata.nasa.gov. ARCSIX data are available to download via Earthdata Search: https://search.earthdata.nasa.gov/. Data can also be accessed by direct download via the ASDC DOI links does not require an Earthdata login. Most files are in a special format called ICARTT (Northup et al., 2017), traditionally used by NASA and other agencies for airborne data. ICARTT is a self-describing text-based file format consisting of a metadata and description header with a prescribed structure followed by a numerical data section in comma-separated value (CSV) form (https://www.earthdata.nasa.gov/about/esdis/esco/standards-practices/icartt). P-3B *in-situ* observations are reported in ICARTT format, whereas remote-sensing data uses a combination of the ICARTT format, HDF, and netCDF. It is critical for any data user to review the ICARTT file headers or netCDF/HDF global attributes that provide guidance on how to both use and interpret data from individual instruments.

Dataset/Resource	Paper	Website (last access: March 12, 2026)	DOI	Citation
P-3B, MetNav	Sect. 3	https://www.earthdata.nasa.gov/data/catalog/larc-cloud-arcsix-metnav-aircraftinsitu-p3b-data-1	https://doi/org/10.5067/SUBORBITAL/ARCSIX/DATA001/P3B/MetNav_AircraftInSitu_1	Bennett et al. (2025a)
P-3B, In-situ aerosol data	Sect. 3	https://www.earthdata.nasa.gov/data/catalog/larc-cloud-arcsix-aerosol-aircraftinsitu-p3b-data-1	https://doi.org/10.5067/SUBORBITAL/ARCSIX/DATA001/P3B/Aerosol_AircraftInSitu_1	Brown et al. (2025)
P-3B, Trace gases	Sect. 3	https://www.earthdata.nasa.gov/data/catalog/larc-cloud-arcsix-tracegas-aircraftinsitu-p3b-data-1	https://doi.org/10.5067/SUBORBITAL/ARCSIX/DATA001/P3B/TraceGas_AircraftInSitu_1	DiGangi et al. (2025)
P-3B, Radiation	Sect. 3	https://www.earthdata.nasa.gov/data/catalog/larc-cloud-arcsix-radiation-aircraftinsitu-p3b-data-1	https://doi.org/10.5067/SUBORBITAL/ARCSIX/DATA001/P3B/Radiation_AircraftInSitu_1	Bucholtz et al. (2025)
P-3B, RSP	Sect. 3	https://www.earthdata.nasa.gov/data/catalog/larc-cloud-arcsix-aircraftremotesensing-p3b-rsp-data-1	https://doi.org/10.5067/SUBORBITAL/ARCSIX/DATA001/P3B/AircraftRemoteSensing/RSP_1	Cairns (2025)
P-3B in situ cloud	Sect. 3	https://www.earthdata.nasa.gov/data/catalog/larc-cloud-arcsix-cloud-aircraftinsitu-p3b-data-1	https://doi.org/10.5067/SUBORBITAL/ARCSIX/DATA001/P3B/Cloud_AircraftInSitu_1	Lawson et al. (2025a)
P-3B GVR	Sect. 3	https://www-air.larc.nasa.gov/cgi-bin/ArcView/arcsix#ZUIDEMA.PAQUITA/	https://doi.org/10.5067/SUBORBITAL/ARCSIX/DATA001/P3B/AircraftRemoteSensing/GVR_1	Perez and Zuidema (2026)
P-3B, MARLi	Sect. 3	https://www.earthdata.nasa.gov/data/catalog/larc-cloud-arcsix-aircraftremotesensing-p3b-marli-data-1	http://doi.org/10.5067/SUBORBITAL/ARCSIX/DATA001/P3B/AircraftRemoteSensing/MARLi_1	Wang (2025)
P-3B, Analysis	Sect. 3	https://www.earthdata.nasa.gov/data/catalog/larc-cloud-arcsix-analysis-p3b-data-1	https://doi.org/10.5067/SUBORBITAL/ARCSIX/DATA001/P3B/Analysis_1	Schlosser and Stamnes (2025a)
P-3B, LVIS	Sect. 3	https://nsidc.org/data/lvisf2/versions/1	https://doi.org/10.5067/VP7J20HJQISD	Blair and Hofton (2020)
G-III, MetNav	Sect. 4	https://www.earthdata.nasa.gov/data/catalog/larc-cloud-arcsix-metnav-aircraftinsitu-larc-g3-data-1	https://doi.org/10.5067/SUBORBITAL/ARCSIX/DATA001/G3/MetNav_AircraftInSitu_1	Bennett (2025b)
G-III, Dropsondes	Sect. 4	https://www.earthdata.nasa.gov/data/catalog/larc-cloud-arcsix-dropsondes-larc-g3-data-1	https://doi.org/10.5067/SUBORBITAL/ARCSIX/DATA001/G3/Dropsondes_1	Thornhill (2025)
G-III, Analysis	Sect. 4	https://www.earthdata.nasa.gov/data/catalog/larc-cloud-arcsix-analysis-larc-g3-data-1	https://doi.org/10.5067/SUBORBITAL/ARCSIX/DATA001/G3/Analysis_1	Schlosser and Stamnes (2025b)
G-III, HALO	Sect. 4	https://www.earthdata.nasa.gov/data/catalog/larc-cloud-arcsix-aircraftremotesensing-larc-g3-halo-data-1	https://doi.org/10.5067/SUBORBITAL/ARCSIX/DATA001/G3/AircraftRemoteSensing/HALO_1	Nehrir (2025)
G-III, AVIRIS-NG, L1B calibrated radiances	Sect. 4	https://www.earthdata.nasa.gov/data/catalog/ornl-cloud-aviris-ng-l1b-radiance-2095-1#overview	https://doi.org/10.3334/ORNLDAAC/2095	Green et al. (2025)
G-III, AVIRIS-NG,	Sect 4	https://www.earthdata.nasa.gov/data/catalog/ornl-cloud-aviris-ng-l2-reflectance-2110-1	https://doi.org/10.3334/ORNLDAAC/2110	Green et al. (2023)

https://doi.org/10.5194/essd-2026-241
Preprint. Discussion started: 24 July 2026

Open Access Earth System Science Data Discussions

L2, surface reflectance				
Learjet, MetNav	ect. 5	https://www.earthdata.nasa.gov/data/catalog/larc-cloud-arcsix-metnav-aircraftinsitu-learjet-data-1	https://doi.org/10.5067/SUBORBITAL/ARCSIX/DATA001/Learjet/MetNav_AircraftInSitu_1	Lawson (2025b)
Learjet, in-situ cloud	Sect. 5	https://www.earthdata.nasa.gov/data/catalog/larc-cloud-arcsix-cloud-aircraftinsitu-learjet-data-1	https://doi.org/10.5067/SUBORBITAL/ARCSIX/ARCSIX_Cloud_AircraftInSitu_Learjet_Data_1	Lawson (2025c)
Learjet, KPR	Sect. 5	https://www.earthdata.nasa.gov/data/catalog/larc-cloud-arcsix-aircraftremotesensing-learjet-kpr-data-1	https://doi.org/10.5067/SUBORBITAL/ARCSIX/DATA001/Learjet/AircraftRemoteSensing/KPR_1	Heckman and Korolev (2025)
Lincoln Sea, SIMBs	Sect. 6	https://arcticdata.io/catalog/view/doi:10.18739/A2T14TR46	https://doi.org/10.18739/A2T14TR46	Polashenski et al. (2024)
Lincoln Sea, SnoTATOS	Sect. 6	https://arcticdata.io/catalog/view/doi:10.18739/A2FJ29F6X	https://doi.org/10.18739/A2FJ29F6X	Raphael et al (2025)
CERES-Terra_FM2 multi-angle data	Sect. 7	https://asdc.larc.nasa.gov/project/CERES/CER_BDS_Terra-FM2_Edition1-CV	https://doi.org/10.5067/TERRA/CERES/BDS_TERRA-FM2_L1.004	NASA (2025a)
CERES-Terra_FM1 CRS	Sect. 7	https://asdc.larc.nasa.gov/project/CERES/CER_CRS_Terra-FM1-MODIS_Edition4A	https://doi.org/10.5067/TERRA/CERES/CRS_TERRA-FM1_L2.004A	NASA (2025b)
CERES-Terra_FM2 CRS	Sect. 7	https://asdc.larc.nasa.gov/project/CERES/CER_CRS_Terra-FM2-MODIS_Edition4A	https://doi.org/10.5067/TERRA/CERES/CRS_TERRA-FM2_L2.004A	NASA (2025c)
CERES-Aqua_FM3 CRS	Sect. 7	https://asdc.larc.nasa.gov/project/CERES/CER_CRS_Aqua-FM3-MODIS_Edition4A	https://doi.org/10.5067/AQUA/CERES/CRS_AQUA-FM3_L2.004A	NASA (2025d)
FLEXPART Data	Sect. 7	https://flexpart-request.nilu.no/arc6	https://doi.org/10.82160/mbkr-9r05	Evangeliou et al. (2026)
Model outputs	Sect. 7	https://www-air.larc.nasa.gov/cgi-bin/ArcView/arcsix?MODEL=1	https://doi.org/10.5067/SUBORBITAL/ARCSIX/DATA001/Model_1	Colarco and Solomon (2026)
THAAO-radiosonde	Sect. 7	https://www.thuleatmos-it.it/dataaccess/soundings/	https://doi.org/10.13127/THAAO/RS	Muscari et al. (2026)
THAAO-All-sky cameras	Sect. 7	https://www.thuleatmos-it.it/dataaccess/allskycamera/	https://doi.org/10.13127/thaao/skycam	Meloni et al. (2026c)
THAAO-meteorology	Sect. 7	https://www.thuleatmos-it.it/dataaccess/meteo/	https://doi.org/10.13127/THAAO/MET	Muscari et al. (2018c)
THAAO-Downward Shortwave and Longwave Irradiance	Sect. 7	https://www.thuleatmos-it.it/dataaccess/DSI/	https://doi.org/10.13127/thaao/dsli_hr	Meloni et al. (2026a)
THAAO-Upwelling Shortwave Irradiance	Sect. 7	https://www.thuleatmos-it.it/dataaccess/USI/	https://doi.org/10.13127/THAAO/USI	Meloni et al. (2026b)
THAAO-Upwelling Longwave Irradiance	Sect. 7	https://www.thuleatmos-it.it/dataaccess/ULI/	https://doi.org/10.13127/THAAO/ULI	Meloni et al. (2026c)
THAAO-Ceilometer	Sect. 7	https://www.thuleatmos-it.it/dataaccess/CBH/	https://doi.org/10.13127/THAAO/CBH	Di Iorio et al. (2022)
THAAO-Infrared Brightness Temperature	Sect. 7	https://www.thuleatmos-it.it/dataaccess/IBT/index.php	https://doi.org/10.12910/DATASET2023-001	Pace et al. (2023a)
THAAO-Integrated water vapor	Sect. 7	https://www.thuleatmos-it.it/dataaccess/vapor/index.php	https://doi.org/10.13127/THAAO/IWV	Muscari et la. (2018b)

THAAO-Integrated water vapor (HATPRO)	Sect. 7	https://www.thuleatmos-it.it/dataaccess/IWV/index.php	https://doi.org/10.12910/DATASET2023-002	Pace et al. (2023b)
THAAO-Liquid Water Path	Sect. 7	https://www.thuleatmos-it.it/dataaccess/LWP/index.php	https://doi.org/10.12910/DATASET2023-003	Pace et al. (2023d)
THAAO-Soot Photometer	Sect. 7	https://zenodo.org/records/21479230	https://doi.org/10.5281/zenodo.21479230	Khan and Peng (2026)

Supplement link

Supplementary material provides a week-by-week description of the flight details and weather conditions and additional tables and figure that provide data information and context.

Team list

All authors included in author list.

Author contributions

Conceptualization, resources, funding acquisition, and supervision: SS, PCT, LNB, HM, TM; writing – original draft preparation: PCT, AS, RU; data curation: MS, MAS, GC, MB, Sean Leavor, and GM; formal analysis, investigation, methodology, software, validation, and visualization: all authors; and writing, reviewing and editing: all authors.

Competing interests

The contact author has declared that none of the authors has any competing interests.

Disclaimer

Copernicus Publications adds a standard disclaimer: "Copernicus Publications remains neutral with regard to jurisdictional claims made in the text, published maps, institutional affiliations, or any other geographical representation in this paper. While Copernicus Publications makes every effort to include appropriate place names, the final responsibility lies with the authors. Views expressed in the text are those of the authors and do not necessarily reflect the views of the publisher."
Please feel free to add disclaimer text at your choice, if applicable.

Acknowledgements

The authors would like to thank the support and guidance of the NASA Radiation Sciences and Cryospheric Science programs. ARCSIX would not have been possible without the contributions of the NASA Earth Science Project Office (Dan Chirica, Stevie Phothisane, and Daisy Gonzalez), NASA Wallops Flight Facility Project and engineering support (Kelly Griffin, Monica Chance, Michael Cropper, Mike Terrell, Ariel "Eddy" Diaz, Chris Youngblood, Cristian Zanin, Kerry Gros, Donnie Cravers, Josh Bobek), ARCSIX P-3B and C-130 pilots (Brian Bernth, John Baycura, Alan Barringer, Greg Jenkins, Alexandra Lewis,

https://doi.org/10.5194/essd-2026-241
Preprint. Discussion started: 24 July 2026

Mike Granger, Billy Bushman), G-III pilots and engineering support (Pat Bookey, Greg Slover, Mattew Elder, Brian Baxley, Dennis Rippy, Chris Swanson), and Learjet Pilot (TR Vreeland) as without their effort the project could not have been a success. We acknowledge the use of imagery from the NASA Worldview application (https://worldview.earthdata.nasa.gov), part of the NASA Earth Science Data and Information System (ESDIS). We thank our hosts at Pituffik, Greenland and at Pituffik Space Base for their hospitality and support. We also thank our Environment Canada colleagues at the Alert station for coordination with us during this campaign.

Collaborators of ARCSIX acknowledge the many funding sources. The MPLNET project is funded by the NASA Radiation Sciences Program and Earth Observing System. The ØPAL MPL is part of Canada's MPLCAN project (https://www.uwo.ca/sci/mplcan/) and a partner of MPLNET. We thank MPLCAN PI Robert Sica and his team for their effort in establishing MPLCAN and the ØPAL site. ØPAL measurements were made at the Polar Environment Atmospheric Research Laboratory (PEARL) in Eureka by the Canadian Network for the Detection of Atmospheric Composition Change (CANDAC), primarily supported by the Natural Sciences and Engineering Research Council of Canada, the Canadian Space Agency, and Environment and Climate Change Canada. U. Im, H. Skov, A. Massling, L. Zhang, A. Nenes, and R. Foskinis acknowledge the European Commission's Horizon Europe funded CleanCloud project (grant agreement no: 101137639). AERONET data were made possible through support of NASA and Environment and Climate Change Canada, and we thank I. Abboud, V. Fioletov, P. Gupta, J. Hannigan, P. Itkin, E. Lind, and A. Smirnov for their effort in establishing and maintaining the Alert, Pituffik, and the icebreaker RV Kronprins Haakon sites. We also thank N. Risse and P. A. Dodd, who helped coordinate sun photometer measurements on the Polarstern and Kronprins Haakon, respectively. S. Becker and M. Wendisch thank the German Research Foundation (DFG) for funding the project (AC)^3 – Project ID 268020496 – TRR 172, which enabled their contribution to ARCSIX. The GEOS data used in this study/project have been provided by the Global Modeling and Assimilation Office (GMAO) at NASA Goddard Space Flight Center through the online data portal in the NASA Center for Climate Simulation. FLEXPART simulations are cross-atmospheric research infrastructure services provided by the ATMO-ACCESS project (EU grant agreement No 101008004). NE and CGZ were funded by the same project. The computations/simulations were performed on resources provided by Sigma2 - the National Infrastructure for High Performance Computing and Data Storage in Norway. The Italian scientific activities at THAAO have been supported by INGV, ENEA, by the Italian Antarctic Research Program (PNRA) and by the Italian Arctic Research Program (PRA) through the Effects of Changing Albedo and Precipitation on the Arctic Climate (ECAPAC) project. Both PNRA and PRA are directed by the Ministry of University and Research. INGV supports THAAO within the framework of the Pianeta Dinamico project, the Multidisciplinary Analysis of Climate change indicators in the Mediterranean And Polar regions (MACMAP) project, and through agreements with the National Science Foundation (USA) and Inussuk (DK). The participation of the Solar Radiation Group of the University of Valencia has been jointly supported by the Spanish Research Agency, through A ground-based remote sensing strategy to the exPlore aErosol cLoud InteraCtions and rAdiative forciNg (PELICAN) project (PID2021-123881OB-I00) and the Valencian Autonomous Government through CIAICO2023-088. The GEOEO expedition on IB Oden was organized by the Swedish Polar Research Secretariat and IB *Oden* is a Swedish national infrastructure supported by the Swedish Research Council (VR, Grant: 2021-00153_VR). A. Khan and P. Xian are supported by NSF Arctic System Sciences Award #: 2336702.

Financial support

The ARCSIX team and core data product collection effort was sponsored by NASA's Radiation Sciences and Cryospheric Science Programs (NNH21ZDA001N-ARCSIX).

Review statement

The review statement will be added by Copernicus Publications listing the handling editor as well as all contributing referees according to their status anonymous or identified.

References

Abbatt, J. P. D., Leaitch, W. R., Aliabadi, A. A., Bertram, A. K., Blanchet, J. P., Boivin-Rioux, A., Bozem, H., Burkart, J., Chang, R. Y. W., Charette, J., et al.: Overview paper: New insights into aerosol and climate in the Arctic, Atmos. Chem. Phys., 19, 2527–2560, https://doi.org/10.5194/acp-19-2527-2019, 2019.

Agresti, A. and Coull, B. A.: Approximate Is Better than "Exact" for Interval Estimation of Binomial Proportions, *The American Statistician*, 52, 119–126, https://doi.org/10.2307/2685469, 1998.

Alkama, R., et al.: Clouds damp the radiative impacts of polar sea ice loss, *The Cryosphere*, 14, 2673–2686, https://doi.org/10.5194/tc-14-2673-2020, 2020.

ASTM: Standard test method for calibration of a pyranometer using a pyrheliometer, ASTM G167-05, ASTM International, https://doi.org/10.1520/G0167-05, 2005.

Alexandrov, M. D., Cairns, B., and Mishchenko, M. I.: Rainbow Fourier transform. Journal of Quantitative Spectroscopy and Radiative Transfer, 113, 2521-2535, https://doi.org/10.1016/j.jqsrt.2012.03.025, 2012a.

Alexandrov, M. D., Cairns, B., Emde, C., Ackerman, A. S., and Van Diedenhoven, B.: Accuracy assessments of cloud droplet size retrievals from polarized reflectance measurements by the research scanning polarimeter. Remote Sensing of Environment, 125, 92-111, http://dx.doi.org/10.1016/j.rse.2012.07.012, 2012b.

Alexandrov, M. D., Cairns, B., Sinclair, K., Wasilewski, A. and coauthors: Retrievals of cloud droplet size from the research scanning polarimeter data: Validation using in situ measurements, Remote Sensing of Environment, 210, 76-95, https://doi.org/10.1016/j.rse.2018.03.005, 2018.

Anderson, T. L., Charlson R. J. , and Covert D. S.: Calibration of a counterflow virtual impactor at aerodynamic diameters from 1 to 15 μm. *Aer. Sci. Technol.*, 19, 317–329, https://doi.org/10.1080/02786829308959639, 1993.

Anderson, T. L. and Ogren, J. A.: Determining Aerosol Radiative Properties Using the TSI 3563 Integrating Nephelometer, Aerosol Sci. Tech., 29, 57–69, https://doi.org/10.1080/02786829808965551, 1998.

Badosa, J., Wood, J., Blanc, P., Long, C. N., Vuilleumier, L., Demengel, D., and Haeffelin, M.: Solar irradiances measured using SPN1 radiometers: uncertainties and clues for development, Atmos. Meas. Tech., 7, 4267–4283, https://doi.org/10.5194/amt-7-4267-2014, 2014.

Bahreini, R., Dunlea, E. J., Matthew, B. M., Simons, C., Docherty, K. S., DeCarlo, P. F., Jimenez, J. L., Brock, C. A., and Middlebrook, A. M.: Design and operation of a pressure-controlled inlet for airborne sampling with an aerodynamic aerosol lens, Aerosol Sci. Technol., 42, 465–471, 2008.

Blair, J. B. and Hofton, M: *LVIS Facility L2 Geolocated Surface Elevation and Canopy Height Product*. (LVISF2, Version 1). [Data Set]. Boulder, Colorado USA. NASA National Snow and Ice Data Center Distributed Active Archive Center. https://doi.org/10.5067/VP7J20HJQISD. [*Surface elevation*]. Date Accessed 07-21-2026.

Barry, K. R., Hill, T. C. J., Levin, E. J. T., Twohy, C. H., Moore, K. A., Weller, Z. D., et al.: Observations of ice nucleating particles in the free troposphere from western US wildfires, *Journal of Geophysical Research: Atmospheres*, 126, e2020JD033752, https://doi.org/10.1029/2020JD033752, 2021.

Barry, K. R., Hill, T. C. J., Jentzsch, C., Moffett, B. F., Stratmann, F., and DeMott, P. J.: Pragmatic protocols for working cleanly when measuring ice nucleating particles, Atmos. Res., 250, 105419, https://doi.org/10.1016/j.atmosres.2020.105419, 2021.

Baumgardner, D. and Rodi, A.: Laboratory and Wind Tunnel Evaluations of the Rosemount Icing Detector, J. of Atmos and Ocean Tech, 6, 971-979, https://doi.org/10.1175/1520-0426(1989)006<0971:LAWTEO>2.0.CO;2, 1989.

Baumgardner, D., Cooper, W. A., and Dye, J. E.: Optical and electronic limitations of the forward-scattering spectrometer probe. *Liquid Particle Size Techniques,* Vol. 2, ASTM STP 1083, E. D. Hirleman, W. D. Bachalo, and P. G. Felton, Eds., American Society for Testing and Materials, 115–127, 1990.

Belter, H. J., Krumpen, T., von Albedyll, L., Alekseeva, T. A., Birnbaum, G., Frolov, S. V., Hendricks, S., Herber, A., Polyakov, I., Raphael, I., Ricker, R., Serovetnikov, S. S., Webster, M., and Haas, C.: Interannual variability in Transpolar Drift summer sea ice thickness and potential impact of Atlantification, The Cryosphere, 15, 2575–2591, https://doi.org/10.5194/tc-15-2575-2021, 2021.

Bennett, J. R., Digangi, J. P., Diskin, G. S., and Thornhill, K. L.: ARCSIX P-3B In-Situ Meteorology and Navigation Data, NASA Langley Atmospheric Science Data Center DAAC [data set], https://doi.org/10.5067/SUBORBITAL/ARCSIX/DATA001/P3B/MetNav_AircraftInSitu_1, 2025a.

Bennett, J. R.: ARCSIX LaRC G-III In-Situ Meteorology and Navigation Data, NASA Langley Atmospheric Science Data Center DAAC [data set], https://doi.org/10.5067/SUBORBITAL/ARCSIX/DATA001/G3/MetNav_AircraftInSitu_1, 2025b.

Beswick, K. M., Gallagher, M. W., Webb, A. R., Norton, E. G., and Perry, F.: Application of the Aventech AIMMS20AQ airborne probe for turbulence measurements during the Convective Storm Initiation Project, Atmos. Chem. Phys., 8, 5449–5463, https://doi.org/10.5194/acp-8-5449-2008, 2008.

Bliss, A. C.: Passive microwave Arctic sea ice melt onset dates from the advanced horizontal range algorithm 1979–2022 [data set], *Sci Data*, 10, 857, https://doi.org/10.1038/s41597-023-02760-5, 2023.

Boisvert, L. N., Boeke, R. C., Taylor, P. C., and Parker, C. L.: Constraining Arctic Climate Projections of Wintertime Warming with Surface Turbulent Flux Observations and Representation of Surface-Atmosphere Coupling, Front. Earth Sci., 10, 765304, https://doi.org/10.3389/feart.2022.765304, 2022.

Bohn, K., Guanter, L., Kuester, T., Preusker, R., Segl, K.: Coupled retrieval of the three phases of water from spaceborne imaging spectroscopy measurements, Remote Sensing of Environment, 242, https://doi.org/10.1016/j.rse.2020.111708, 2020.

Bond, T. C., Doherty, S. J., Fahey, D. W., Forster, P. M., Berntsen, T., Deangelo, B. J., Flanner, M. G., Ghan, S., Kärcher, B., Koch, D., Kinne, S., Kondo, Y., Quinn, P. K., Sarofim, M. C., Schultz, M. G., Schulz, M., Venkataraman, C., Zhang, H., Zhang, S., Bellouin, N., Guttikunda, S. K., Hopke, P. K., Jacobson, M. Z., Kaiser, J. W., Klimont, Z., Lohmann, U., Schwarz, J. P., Shindell, D., Storelvmo, T., Warren, S. G., and Zender, C. S.: Bounding the role of black carbon in the climate system: A scientific assessment, J. Geophys. Res. Atmos., 118, 5380–5552, https://doi.org/10.1002/jgrd.50171, 2013.

Böttcher, K., Paunu, V.-V., Kupiainen, K., Zhizhin, M., Matveev, A., Savolahti, M., Klimont, Z., Väätäinen, S., Lamberg, H., and Karvosenoja, N.: Black carbon emissions from flaring in Russia in the period 2012-2017, Atmos. Environ., 254, 118390, https://doi.org/10.1016/j.atmosenv.2021.118390, 2021.

Box, J. E., Hubbard, A., Bahr, D. B., et al.: Greenland ice sheet climate disequilibrium and committed sea-level rise, Nat. Clim. Chang., 12, 808–813, https://doi.org/10.1038/s41558-022-01441-2, 2022.

Brodrick, P. G., Thompson, D. R., Garay, M. J., Giles, D. M., Holben, B. N., & Kalashnikova, O. V.: Simultaneous characterization of wildfire smoke and surface properties with imaging spectroscopy during the FIREX-AQ field campaign. Journal of Geophysical Research: Atmospheres, e2021JD034905. https://doi.org/10.1029/2021JD034905, 2022.

Brown, M., Edwards, E.-L., Gallo, F., Moore, R., Pratt, K. A., Shook, M., Sorooshian, A., Wang, J., Winstead, E., and Ziemba, L.: ARCSIX P-3B In-Situ Aerosol Data, NASA Langley Atmospheric Science Data Center DAAC [data set], https://doi.org/10.5067/SUBORBITAL/ARCSIX/DATA001/P3B/Aerosol_AircraftInSitu_1, 2025.

Burton, S. P., Ferrare, R. A., Hostetler, C. A., Hair, J.W., Rogers, R. R., Obland, M. D., Butler, C. F., Cook, A. L., Harper, D. B., and Froyd, K. D.: Aerosol classification using airborne High Spectral Resolution Lidar measurements – methodology and examples, Atmos. Meas. Tech., 5, 73–98, https://doi.org/10.5194/amt-5-73-2012 , 2012.

Burton, S. P., Hair, J. W., Kahnert, M., Ferrare, R. A., Hostetler, C. A., Cook, A. L., Harper, D. B., Berkoff, T. A., Seaman, S. T., Collins, J. E., Fenn, M. A., and Rogers, R. R.: Observations of the spectral dependence of linear particle depolarization ratio of aerosols using NASA Langley airborne High Spectral Resolution Lidar, Atmos. Chem. Phys., 15, 13453–13473, https://doi.org/10.5194/acp-15-13453-2015, 2015.

Buth, L. G., Krumpen, T., Neckel, N., Webster, M. A., Birnbaum, G., Fuchs, N., Heuser, P., Johannsen, O., and Haas, C.: Characterizing sea ice melt pond fraction and geometry in relation to surface morphology, The Cryosphere, 19, 6527–6545, https://doi.org/10.5194/tc-19-6527-2025, 2025.

Buchard, V., Randles, C. A., Silva, A. M. da, Darmenov, A., Colarco, P. R., Govindaraju, R., Ferrare, R., Hair, J., Beyersdorf, A. J., Ziemba, L. D., and Yu, H.: The MERRA-2 Aerosol Reanalysis, 1980 Onward. Part II: Evaluation and Case Studies, J Climate, https://doi.org/10.1175/jcli-d-16-0613.1, 2017.

Bucholtz, A., Bluth, R. T., Kelly, B., Taylor, S., Batson, K., Sarto, A. W., Tooman, T. P., and McCoy Jr., R. F.: The Stabilized Radiometer Platform (STRAP)—An actively stabilized horizontally level platform for improved aircraft irradiance measurements, J. Atmos. Oceanic Technol., 25, 2161–2175, https://doi.org/10.1175/2008JTECHA1085.1, 2008.

Bucholtz, A., Hlavka, D. L., McGill, M. J., Schmidt, K. S., Pilewskie, P., Davis, S. M., Reid, E. A., and Walker, A. L.: Directly Measured Heating Rates of a Tropical Subvisible Cirrus Cloud, Journal of Geophysical Research-Atmospheres, 115, 1–11, 2010.

Bucholtz, A., Chen, H., Perez, M., Schmidt, S., and Zuidema, P.: ARCSIX P-3B In-Situ Radiation Data, NASA Langley Atmospheric Science Data Center DAAC [data set], https://doi.org/10.5067/SUBORBITAL/ARCSIX/DATA001/P3B/Radiation_AircraftInSitu_1, 2025.

Cairns, B., Russell, E.E. and Travis, L.D.: The Research Scanning Polarimeter: Calibration and ground-based measurements. In Polarization: Measurement, Analysis, and Remote Sensing II, 18 Jul. 1999, Denver, Col., Proc. SPIE, vol. 3754, p. 186, doi:10.1117/12.366329, 1999.

Cairns, B.: ARCSIX P-3B Aircraft Research Scanning Polarimeter (RSP) Data, NASA Langley Atmospheric Science Data Center DAAC [data set], https://doi.org/10.5067/SUBORBITAL/ARCSIX/DATA001/P3B/AircraftRemoteSensing/RSP_1, 2025.

Cadeddu, M. P., Liljegren, J. C., and Pazmany, A.: Measurements and retrievals from a new 183-GHz water vapor radiometer in the Arctic, IEEE T. Geosci. Remote, 45, 2759–2777, https://doi.org/10.1109/TGRS.2006.888970, 2007.

Carroll, B. J., Nehrir, A. R., Kooi, S. A., Collins, J. E., Barton-Grimley, R. A., Notari, A., Harper, D. B., and Lee, J.: Differential absorption lidar measurements of water vapor by the High Altitude Lidar Observatory (HALO): retrieval framework and first results, Atmos. Meas. Tech., 15, 605–626, https://doi.org/10.5194/amt-15-605-2022, 2022.

Cassano, J.J., and coauthors: Development of the Regional Arctic System Model (RASM): Near-Surface Atmospheric Climate Sensitivity. Journal of Climate, 30, 5729-5753, https://doi.org/10.1175/JCLI-D-15-0775.1, 2017.

Cassiani, M., Stohl, A., and Brioude, J.: Lagrangian Stochastic Modelling of Dispersion in the Convective Boundary Layer with Skewed Turbulence Conditions and a Vertical Density Gradient: Formulation and Implementation in the FLEXPART Model, *Boundary-Layer Meteorol.*, 154, 367–390, https://doi.org/10.1007/s10546-014-9976-5, 2015.

Chapman, J., Thompson, D.R. , Helmlinger, M. C., Bue, B. D., and coauthors: Spectral and radiometric calibration of the Next Generation Airborne Visible Infrared Spectrometer (AVIRIS-NG), Remote Sens., 11(18), 2129; https://doi.org/10.3390/rs11182129, 2019.

Chen, B.: bochens/SizeDistMerge: v0.5.0 (v0.5.0). Zenodo. https://doi.org/10.5281/zenodo.20709064, 2026.

Cheng, Z., Sharma, N., Tseng, K.-P., Kovarik, L., and China, S.: Direct observation and assessment of phase states of ambient and lab-generated sub-micron particles upon humidification, *RSC Advances*, 11, 15264–15272, https://doi.org/10.1039/D1RA02530A, 2021.

https://doi.org/10.5194/essd-2026-241
Preprint. Discussion started: 24 July 2026

Cheng, Z., Liyu, A., Dexheimer, D., Lata, N. N., Kulkarni, G., Longbottom, C. M., Mei, F., and China, S.: An automated size and time-resolved aerosol collector platform integrated with environmental sensors to study the vertical profile of aerosols, *Environmental Science: Atmospheres*, 2, 1263–1276, https://doi.org/10.1039/D2EA00097K, 2022.

Cheng, Z., Morgenstern, M., Henning, S., Zhang, B., Roberts, G. C., Fraund, M., Marcus, M. A., Lata, N. N., Fialho, P., Mazzoleni, L., Wehner, B., Mazzoleni, C., and China, S.: Cloud condensation nuclei activity of internally mixed particle populations at a remote marine free troposphere site in the North Atlantic Ocean, *Science of The Total Environment*, 904, 166865, https://doi.org/10.1016/j.scitotenv.2023.166865, 2023.

Cheng, Z., Shrivastava, M., Ijaz, A., Veghte, D., Vandergrift, G. W., Tseng, K.-P., Lata, N. N., Kew, W., Suski, K., Weis, J., Kulkarni, G., Berg, L. K., Fast, J. D., Kovarik, L., Mazzoleni, L. R., Zelenyuk, A., and China, S.: Enhanced light absorption for solid-state brown carbon from wildfires due to organic and water coatings, *Nature Communications*, 15, 10326, https://doi.org/10.1038/s41467-024-54506-5, 2024.

Ciardini V., Muscari G., di Sarra A., Di Iorio T., Meloni D., Pace G., Scarchilli C., Calì Quaglia F., Tosco M., Bagiacchi P., Cannataro G., Iaccarino A.: Meteorological data at the precipitation mast at the Thule High Arctic Atmospheric Observatory (THAAO_Met_Prec). Agenzia Nazionale per le nuove tecnologie, l'energia e lo sviluppo economico sostenibile (ENEA). https://doi.org/10.13127/THAAO/MET_PREC, 2026.

Cober, S., Isaac, G.A., and Korolev, A.V.,: Assessing the Rosemount Icing Detector with In Situ Measurements, J. Atmos. Oceanic. Technol, 18, 515-528, https://doi.org/10.1175/1520-0426(2001)018<0515:ATRIDW>2.0.CO;2, 2001.

Cochrane, S. P., Schmidt, K. S., Chen, H., Pilewskie, P., Kittelman, S., Redemann, J., LeBlanc, S., Pistone, K., Kacenelenbogen, M., Segal Rozenhaimer, M., Shinozuka, Y., Flynn, C., Platnick, S., Meyer, K., Ferrare, R., Burton, S., Hostetler, C., Howell, S., Freitag, S., Dobracki, A., and Doherty, S.: Above-cloud aerosol radiative effects based on ORACLES 2016 and ORACLES 2017 aircraft experiments, Atmos. Meas. Tech., 12, 6505–6528, https://doi.org/10.5194/amt-12-6505-2019, 2019.

Colarco, P., Silva, A. D., Chin, M., and Diehl, T.: Online simulations of global aerosol distributions in the NASA GEOS-4 model and comparisons to satellite and ground-based aerosol optical depth, *J Geophys Res Atmospheres*, 115, D10S07, https://doi.org/10.1029/2009jd012820, 2010.

Colarco, P. and Solomon, A: Arctic Aerosol and Coupled Modeling Simulation Outputs, NASA Langley Atmospheric Science Data Center DAAC [data set], https://doi.org/10.5067/SUBORBITAL/ARCSIX/DATA001/Model_1 , 2026.

Collister, B., and Nehrir, A: HALO File Structure and Plotting Example. Zenodo. https://doi.org/10.5281/zenodo.20801228, 2026.

Crosbie, E., Hair, J. W., Nehrir, A. R., Ferrare, R. A., Hostetler, C., Shingler, T., Harper, D., Fenn, M., Collins, J., Barton-Grimley, R., Collister, B., Thornhill, K. L., Voigt, C., Kirschler, S., and Sorooshian, A.: A method to retrieve mixed-phase cloud vertical structure from airborne lidar, Atmos. Meas. Tech., 18, 2639–2658, https://doi.org/10.5194/amt-18-2639-2025, 2025.

DeCarlo, P. F., Dunlea, E. J., Kimmel, J. R., Aiken, and co-authors: Fast airborne aerosol size and chemistry measurements above Mexico City and Central Mexico during the MILAGRO campaign, Atmos. Chem. Phys., 8, 4027–4048, https://doi.org/10.5194/acp-8-4027-2008, 2008.

DeMott, P. J., Prenni, A. J., McMeeking, G. R., Sullivan, and coauthors: Integrating laboratory and field data to quantify the immersion freezing ice nucleation activity of mineral dust particles, Atmos. Chem. Phys., 15, 393–409, https://doi.org/10.5194/acp-15-393-2015, 2015.

DiGangi, J. P., Choi, Y., Nowak, J. B., Halliday, H. S., Diskin, G. S., Feng, S. and coauthors: Seasonal variability in local carbon dioxide biomass burning sources over central and eastern US using airborne in situ enhancement ratios. Journal of Geophysical Research: Atmospheres, 126, e2020JD034525. https://doi.org/10.1029/2020JD034525, 2021.

DiGangi, J. P., Diskin, G. S., Yoon, S., Alvarez, S. L., Flynn, J. H., Robinson, C. E., Shook, M. A., Thornhill, K. L., Winstead, E. L., Ziemba, L. D., Cambaliza, M. O. L., Simpas, J. B., Hilario, M. R. A., and Sorooshian, A.: Technical note: Apportionment of Southeast Asian biomass burning and urban influence via in situ trace gas enhancement ratios, Atmos. Chem. Phys., 25, 17387–17397, https://doi.org/10.5194/acp-25-17387-2025, 2025.

https://doi.org/10.5194/essd-2026-241
Preprint. Discussion started: 24 July 2026

Earth System Science Data Discussions
Open Access

DiGangi, J. P., and Diskin, G. S.: ARCSIX P-3B In-Situ Trace Gas Data, NASA Langley Atmospheric Science Data Center DAAC [data set], https://doi.org/10.5067/SUBORBITAL/ARCSIX/DATA001/P3B/TraceGas_AircraftInSitu_1, 2025.

Di Iorio, T., di Sarra, A., Pace, G., Meloni, D., Muscari, G., Di Liberto, L., Calì Quaglia, F., and Iaccarino, A.: Cloud Base Height at the Thule High Arctic Atmospheric Observatory (THAAO_CBH), https://doi.org/10.13127/THAAO/CBH, 2022.

Diskin, G.S., Podolske, J. R., Sachse, G. W., and Slate, T. A.: Open-path airborne tunable diode laser hygrometer, Open-path airborne tunable diode laser hygrometer", Proc. SPIE 4817, Diode Lasers and Applications in Atmospheric Sensing, https://doi.org/10.1117/12.453736, 2002.

Dmitrovic, S., Hair, J. W., Collister, B. L., Crosbie, E., Fenn, M. A., Ferrare, R. A., Harper, D. B., Hostetler, C. A., Hu, Y., Reagan, J. A., Robinson, C. E., Seaman, S. T., Shingler, T. J., Thornhill, K. L., Vömel, H., Zeng, X., and Sorooshian, A.: High Spectral Resolution Lidar – generation 2 (HSRL-2) retrievals of ocean surface wind speed: methodology and evaluation, Atmos. Meas. Tech., 17, 3515–3532, https://doi.org/10.5194/amt-17-3515-2024, 2024.

Duncan, B. N., Ott, L. E., Abshire, J. B., Brucker, L., Carroll, M. L., Carton, J., Comiso, J. C., Dinnat, E. P., Forbes, B. C., Gonsamo, A., Gregg, W. W., Hall, D. K., Ialongo, I., Jandt, R., Kahn, R. A., Karpechko, A., Kawa, S. R., Kato, S., Kumpula, T., Kyrölä, E., Loboda, T. V., McDonald, K. C., Montesano, P. M., Nassar, R., Neigh, C. S. R., Parkinson, C. L., Poulter, B., Pulliainen, J., Rautiainen, K., Rogers, B. M., Rousseaux, C. S., Soja, A. J., Steiner, N., Tamminen, J., Taylor, P. C., Tzortziou, M. A., Virta, H., Wang, J. S., Watts, J. D., Winker, D. M., and Wu, D. L.: Space-Based Observations for Understanding Changes in the Arctic-Boreal Zone, *Reviews of Geophysics*, 58, e2019RG000652, https://doi.org/10.1029/2019RG000652, 2020.

Elias, T., Cairns, B., and Chowdhary, J.: Surface optical properties measured by the airborne research scanning polarimeter during the CLAMS experiment, in: Remote Sensing of Clouds and the Atmosphere VIII, edited by: Schaefer, K., Comeron, A., Carleer, M. R. and Picard, R. H., Proc. SPIE,, 5235, 595–606, 2004.

Ephraim, S., Zuidema, P., Juliano, T. W., Grasmick, C., Geerts, B., French, J., Cadeddu, M., Pazmany, A., and Woods, S.: A New Machine Learning Retrieval of Liquid Water Path Optimized for Mixed-Phase Cold Air Outbreaks Using Radiometer and Radar Observations, J. Atmos. Oceanic Tech., 42, 1299–1316, https://doi.org/10.1175/JTEC-D-24-0132.1, 2025.

Evangeliou, N., Eckhardt, S., Groot Zwaaftink, C., and Sollum, E.: FLEXPART model tools for black carbon and mineral dust for NASA's ARCSIX campaign in 2024 [data set], https://doi.org/10.82160/mbkr-9r05, 2026.

Faber, S., French, J. R., and Jackson, R.: Laboratory and in-flight evaluation of measurement uncertainties from a commercial Cloud Droplet Probe (CDP), Atmos. Meas. Tech., 11, 3645–3659, https://doi.org/10.5194/amt-11-3645-2018, 2018.

Forster, C., Stohl, A., and Seibert, P.: Parameterization of convective transport in a Lagrangian particle dispersion model and its evaluation, J. Appl. Meteorol. Climatol., 46, 403–422, https://doi.org/10.1175/JAM2470.1, 2007.

Frey, M. M., Norris, S. J., Brooks, I. M., Anderson, P. S., Nishimura, K., Yang, X., Jones, A. E., Nerentorp Mastromonaco, M. G., Jones, D. H., and Wolff, E. W.: First direct observation of sea salt aerosol production from blowing snow above sea ice, *Atmospheric Chemistry and Physics*, 20, 2549–2578, https://doi.org/10.5194/acp-20-2549-2020, 2020.

Froyd, K. D., et al.: A new method to quantify mineral dust and other aerosol species from aircraft platforms using single-particle mass spectrometry, Atmos. Meas. Tech., 12, 6209–6239, https://doi.org/10.5194/amt-12-6209-2019, 2019.

Fu, Q., and Liou, K.-N.,: Parameterization of the radiative properties of cirrus clouds, J. Atmos. Sci., 50, 2008–2025, https://doi.org/10.1175/1520-0469(1993)050<2008:POTRPO>2.0.CO;2, 1993.

Fuentes, J. D., Lance, S., Pratt, K. A., Shepson, P. B., Simpson, W. R., Antczak, I., Bigge, K., Brockway, N., Garner, N., Hajny, K. D., Jeong, D., Kaeser, R., Peterson, P. K., Serratos, M., Starn, T., Stirm, B. H., and Woods, S.: Overview of the Chemistry in the Arctic: Clouds, Halogens, and Aerosols (CHACHA) Field Campaign, Bulletin of the American Meteorological Society, 106, E2276–E2299, https://doi.org/10.1175/BAMS-D-24-0192.1, 2025.

Gao, R. S., Telg, H., McLaughlin, R. J. Ciciora, S. J. , and coauthors: A light-weight, high-sensitivity particle spectrometer for PM2.5 aerosol measurements, Aerosol Science and Technology, 50:1, 88-99, https://doi.org/10.1080/02786826.2015.1131809, 2016.

The GEOEO Shipboard Scientific Party: GEOEO North of Greenland 2024: Expedition Report, Swedish Polar Research Secretariat, 288 pp., https://doi.org/10.23703/e0p8-8r10, 2025.

https://doi.org/10.5194/essd-2026-241
Preprint. Discussion started: 24 July 2026

Open Access Earth System Science Data Discussions

Gelato, R., and coauthors: The Modern-Era Retrospective Analysis for Research and Application, Version 2 (MERRA-2), J. Climate, 30, 5419–5454, https://doi.org/10.1175/jcli-d-16-0758, 2017.

Giles, D. M., Sinyuk, A., Sorokin, M. G., et al.: Advancements in the Aerosol Robotic Network (AERONET) Version 3 Database – Automated near-Real-Time Quality Control Algorithm with Improved Cloud Screening for Sun Photometer Aerosol Optical Depth (AOD) Measurements, *Atmospheric Measurement Techniques*, 12, 169–209, https://doi.org/10.5194/amt-12-169-2019, 2019.

Ginoux, P., Chin, M., Tegen, I., Prospero, J. M., Holben, B., Dubovik, O., and Shian-Jia: Sources and distributions of dust aerosols simulated with the GOCART model, 2-Journal Geophys. Res., 106, 20255–20273, 2001.

Gómez-Amo, J. L., Tarín, J., Valdelomar, P. C., Scarlatti, F., Estellés, V., and Utrillas, M. P.: A pixelwise approach to derive AOD and COD from all-sky imagery, IOP Conf. Series: Earth and Environmental Science, 1522, 012014, https://doi.org/10.1088/1755-1315/1522/1/012014, 2025.

Green, R. O., Brodrick, P. G., Chapman, J. W., Eastwood, M., Geier, S., Helmlinger, M., Lundeen, S. R., Olson-Duvall, W., Pavlick, R., Rios, L. M., Thompson, D. R., & Thorpe, A. K.: AVIRIS-NG L2 Surface Reflectance, Facility Instrument Collection, V1 (Version 1). ORNL Distributed Active Archive Center, [data set], https://doi.org/10.3334/ORNLDAAC/2110 Date Accessed: 2026-06-29, 2023.

Green, R. O., Brodrick, P. G., Chapman, J. W., Eastwood, M., Geier, S., Helmlinger, M., Lundeen, S. R., Olson-Duvall, W., Pavlick, R., Rios, L. M., Thompson, D. R., & Thorpe, A. K.: AVIRIS-NG L1B Calibrated Radiance, Facility Instrument Collection, V1 (Version 1). ORNL Distributed Active Archive Center, [data set], https://doi.org/10.3334/ORNLDAAC/2095 Date Accessed: 2026-06-29, 2025.

Groot Zwaaftink, C. D., Grythe, H., Skov, H., and Stohl, A.: Substantial contribution of northern high-latitude sources to mineral dust in the Arctic, J. Geophys. Res., 121, 13678–13697, https://doi.org/10.1002/2016JD025482, 2016.

Groot Zwaaftink, C. D., Aas, W., Eckhardt, S., Evangeliou, N., Hamer, P., Johnsrud, M., Kylling, A., Platt, S. M., Stebel, K., Uggerud, H., and Yttri, K. E.: What caused a record high PM10 episode in northern Europe in October 2020?, Atmos. Chem. Phys., 22, 3789–3810, 2022.

Grythe, H., Kristiansen, N. I., Groot Zwaaftink, C. D., Eckhardt, S., Ström, J., Tunved, P., Krejci, R., and Stohl, A.: A new aerosol wet removal scheme for the Lagrangian particle model FLEXPARTv10, Geosci. Model Dev., 10, 1447–1466, https://doi.org/10.5194/gmd-10-1447-2017, 2017.

Gunsch, M. J., Kirpes, R. M., Kolesar, K. R., Barrett, T. E., China, S., Sheesley, R. J., Laskin, A., Wiedensohler, A., Tuch, T., and Pratt, K. A.: Contributions of transported Prudhoe Bay oilfield emissions to the aerosol population in Utqiaġvik, Alaska, Atmos. Chem. Phys., 17, 10879–11892, https://doi.org/10.5194/acp-2017-453, 2017.

Gunsch, M. J., Liu, J., Moffett, C. E., Sheesley, R. J., Wang, N., Zhang, Q., Watson, T. B., and Pratt, K. A.: Diesel soot and amine-containing organic-sulfate aerosols in an Arctic oil field, Environ. Sci. Technol., 54, 92–101, https://doi.org/10.1021/acs.est.9b04825, 2020.

Haggerty, J. A., Maslanik, J. A., and Curry, J. A.: Heterogeneity of sea ice surface temperature at SHEBA from aircraft measurements, J. Geophys. Res., 108, 8052, https://doi.org/10.1029/2000JC000560, 2003.

Hair, J. W., Hostetler, C. A., Cook, A. L., Harper, D. B., Ferrare, R. A., Mack, T. L., Welch, W., Izquierdo, L. R., and Hovis, F. E.: Airborne High Spectral Resolution Lidar for profiling aerosol optical properties, Appl. Optics, 47, 6734–6752, https://doi.org/10.1364/AO.47.006734, 2008.

Hair, J., Cairns, B., Ferrare, R., Hostetler, C., and coauthors: Vertical Profiles of Cloud Extinction and Cloud Top Droplet Number Concentration in Warm Clouds Derived from Airborne Lidar and Polarimeter Measurements. *31st International Laser Radar Conference*, Landshut, Germany, https://doi.org/10.1051/epjconf/202636202004, 2026.

Halliday, H. S., DiGangi, J. P., Choi, Y., Diskin, G. S., Pusede, S. E., Rana, M., et al.. Using short-term CO/CO2 ratios to assess air mass differences over the Korean Peninsula during KORUS-AQ. Journal of Geophysical Research: Atmospheres, 124,10951–10972. https://doi.org/10.1029/2018JD029697, 2019.

https://doi.org/10.5194/essd-2026-241
Preprint. Discussion started: 24 July 2026

Open Access Earth System Science Data Discussions

Hamlin, L., Green, R. O., Mouroulis, P., Eastwood, M., Wilson, D., Dudik, M., andn Paine, C.: Imaging spectrometer science measurements for terrestrial ecology: AVIRIS and new developments. In 2011 Aerospace conference (pp. 1-7). IEEE, 2011.

Marchand, R. (2013), Trends in ISCCP, MISR, and MODIS cloud-top-height and optical-depth histograms, *J. Geophys. Res. Atmos*., 118, doi:10.1002/jgrd.50207

Heckman, I., and Korolev, A.: ARCSIX Learjet Ka-Band Probe Radar-Radiometer (KPR) Data, NASA Langley Atmospheric Science Data Center DAAC [data set], https://doi.org/10.5067/SUBORBITAL/ARCSIX/DATA001/Learjet/AircraftRemoteSensing/KPR_1, 2025.

Hersbach, H., Bell, B., Berrisford, P., Hirahara, S., Horányi, A., Muñoz-Sabater, J., Nicolas, J., Peubey, C., Radu, R., Schepers, D., Simmons, A., Soci, C., Abdalla, S., Abellan, X., Balsamo, G., Bechtold, P., Biavati, G., Bidlot, J., Bonavita, M., De Chiara, G., Dahlgren, P., Dee, D., Diamantakis, M., Dragani, R., Flemming, J., Forbes, R., Fuentes, M., Geer, A., Haimberger, L., Healy, S., Hogan, R. J., Hólm, E., Janisková, M., Keeley, S., Laloyaux, P., Lopez, P., Lupu, C., Radnoti, G., de Rosnay, P., Rozum, I., Vamborg, F., Villaume, S., and Thépaut, J. N.: The ERA5 global reanalysis, Q. J. R. Meteorol. Soc., 146, 1999–2049, https://doi.org/10.1002/qj.3803, 2020.

Hiranuma, N., Augustin-Bauditz, S., Bingemer, H., Budke, and coauthors: A comprehensive laboratory study on the immersion freezing behavior of illite NX particles: a comparison of 17 ice nucleation measurement techniques, Atmos. Chem. Phys., 15, 2489–2518, https://doi.org/10.5194/acp-15-2489-2015, 2015.

Holben, B. N., Eck, T. F., Slutsker, I., Tanré, D., Buis, J. P., Setzer, A., Vermote, E., Reagan, J. A., Kaufman, Y. J., Nakajima, T., Lavenu, F., Jankowiak, I., and Smirnov, A.: AERONET—A Federated Instrument Network and Data Archive for Aerosol Characterization, *Remote Sensing of Environment*, 66, 1–16, https://doi.org/10.1016/S0034-4257(98)00031-5, 1998.

Illingworth, A. J., Hogan, R. J., O'Connor, E. J., Bouniol, D., Brooks, M. E., Delanoé, J., Donovan, D. P., Eastment, J. D., Gaussiat, N., Goddard, J. W. F., Haeffelin, M., Baltink, H. K., Krasnov, O. A., Pelon, J., Piriou, J.-M., Protat, A., Russchenberg, H. W. J., Seifert, A., Tompkins, A. M., van Zadelhoff, G.-J., Vinit, F., Willén, U., Wilson, D. R., and Wrench, C. L.: Cloudnet, *Bulletin of the American Meteorological Society*, 88, 883–898, https://doi.org/10.1175/BAMS-88-6-883, 2007.

IPCC: Climate Change 2021: The Physical Science Basis, in: *Contribution of Working Group I to the Sixth Assessment Report of the Intergovernmental Panel on Climate Change*, edited by: Masson-Delmotte, V., Zhai, P., Pirani, A., Connors, S. L., Péan, C., Berger, S., et al., Cambridge University Press, Cambridge, In Press, 2021.

Jonsson, H. H., Wilson, J.C., Brock, C. A., Knollenberg, R. G, and coauthors: Performance of a focused cavity aerosol spectrometer for measurements in the stratosphere of particle size in the 0.06–2.0 mm diameter range, J. *Atmos. Ocean. Technol.,* **12,** 115-129, https://doi.org/10.1175/1520-0426(1995)012<0115:POAFCA>2.0.CO;2, 1995.

Kaiser, J. W., Heil, A., Andreae, M. O., Benedetti, A., Chubarova, N., Jones, L., Morcrette, J. J., Razinger, M., Schultz, M. G., Suttie, M., and Van Der Werf, G. R.: Biomass burning emissions estimated with a global fire assimilation system based on observed fire radiative power, *Biogeosciences*, 9, 527–554, https://doi.org/10.5194/bg-9-527-2012, 2012.

Kato, S., Ackerman, T. P., Mather, J. H., and Clothiaux, E. E.: The k-distribution method and correlated-k approximation for a shortwave radiative transfer model, J. Quant. Spectrosc. Radiat. Transf., 62,109–121, https://doi.org/10.1016/S0022-4073(98)00075-2, 1999.

Kato, S., F. G. Rose, and T. P. Charlock: Computation of domain averaged irradiance using satellite derived cloud properties, J. Atmos. Oceanic Technol., 22, 146–164, https://doi.org/10.1175/JTECH-1694.1, 2005.

Kato, S., F. G. Rose, Rutan, D. A., Thorsen, T. J., and coauthors: Surface Irradiances of Edition 4.0 Clouds and the Earth's Radiant Energy System (CERES) Energy Balanced and Filled (EBAF) Data Product, J. Climate, 31, 4501-4527, https://doi.org/10.1175/JCLI-D-17-0523.1, 2018.

Kipp & Zonen: CG4 pyrgeometer: Instruction manual, 64 pp., 2001.

Kipp & Zonen: CM22 precision pyranometer: Instruction manual, 65 pp., 2004.

https://doi.org/10.5194/essd-2026-241
Preprint. Discussion started: 24 July 2026

Khan, A. L., Wagner, S., Jaffe, R., Xian, P., Williams, M., Armstrong, R., and McKnight, D.: Impacts of coal dust on the spectral reflectance of Arctic surface snow in Svalbard, Norway, J. Geophys. Res.-Atmos., 122, 1767-1778, https://doi.org/10.1002/2016JD025757, 2017

Khan, A. L., Xian, P., and Schwarz, J. P.: Black carbon concentrations and modeled smoke deposition fluxes to the bare-ice dark zone of the Greenland Ice Sheet, The Cryosphere, 17, 2909–2918, https://doi.org/10.5194/tc-17-2909-2023, 2023.

Khan, A.& Xian, P.: Pituffik SP2-XR Surface Measured Surface Concentrations and NAAPs-RA modeled surface aerosol concentrations [Dataset]. Zenodo. https://doi.org/10.5281/zenodo.21479230, 2026.

Kirpes, R. M., Bondy, A. L., Bonanno, D., Moffet, R. C., Wang, B., Laskin, A., Ault, A. P., and Pratt, K. A.: Secondary sulfate is internally mixed with sea spray aerosol and organic aerosol in the winter Arctic, Atmos. Chem. Phys., 18, 3937–3949, https://doi.org/10.5194/acp-18-3937-2018, 2018.

Kirpes, R. M., Bonanno, D., May, N. W., Fraund, M., Barget, A. J., Moffet, R. C., Ault, A. P., and Pratt, K. A.: Wintertime Arctic Sea Spray Aerosol Composition Controlled by Sea Ice Lead Microbiology, *ACS Central Science*, 5, 1760–1767, https://doi.org/10.1021/acscentsci.9b00541, 2019.

Kirpes, R. M., Rodriguez, B., Kim, S., China, S., Laskin, A., Park, K., Jung, J., Ault, A. P., and Pratt, K. A.: Influence of marine emissions and atmospheric processing on individual particle composition of summertime Arctic aerosol in the Bering Strait and Chukchi Sea, *Environmental Science: Processes & Impacts*, 22, 1201–1213, https://doi.org/10.1039/C9EM00495E, 2020.

Kirpes, R. M., Lei, Z., Fraund, M., Gunsch, M. J., May, N. W., Barrett, T. E., Moffett, C. E., Schauer, A. J., Alexander, B., Upchurch, L. M., China, S., Quinn, P. K., Moffet, R. C., Laskin, A., Sheesley, R. J., Pratt, K. A., and Ault, A. P.: Solid Organic-Coated Ammonium Sulfate Particles at High Relative Humidity in the Summertime Arctic Atmosphere, *Proceedings of the National Academy of Sciences*, 119, e2104496119, https://doi.org/10.1073/pnas.2104496119, 2022.

Klimont, Z., Kupiainen, K., Heyes, C., Purohit, P., Cofala, J., Rafaj, P., Borken-Kleefeld, J., and Schöpp, W.: Global anthropogenic emissions of particulate matter including black carbon, Atmos. Chem. Phys., 17, 8681–8723, https://doi.org/10.5194/acp-17-8681-2017, 2017.

Knobelspiesse, K., Cairns, B., Ottaviani, M., Ferrare, and coauthors: Combined retrievals of boreal forest fire aerosol properties with a polarimeter and lidar, Atmos. Chem. Phys., 11, 7045–7067, https://doi.org/10.5194/acp-11-7045-2011, 2011.

Knobelspiesse, K., Cairns, B., Schaaf, C., Schmid, B., and Roman, M.: Surface BRDF estimation from an aircraft compared to MODIS and ground estimates at the Southern Great Plains site, J. Geophys. Res., 113, 1–21, D20105, https://doi.org/10.1029/2008JD010062, 2008.
Knollenberg, R.G.: Techniques for probing cloud microstructure. Clouds Their Formation, Optical Properties, and Effects, P.V. Hobbs and A. Deepak, Eds., Academic Press, New York, NY. 15-91, 1981.

Kok, J. F., Ridley, D. A., Zhou, Q., Miller, R. L., Zhao, C., Heald, C. L., Ward, D. S., Albani, S., and Haustein, K.: Smaller desert dust cooling effect estimated from analysis of dust size and abundance, Nat. Geosci., 10, 274–278, https://doi.org/10.1038/ngeo2912, 2017.

Korolev, A.V., J.W. Strapp, G.A. Isaac and A.N. Nevzorov: The Nevzorov Airborne Hot-wire LWC-TWC Probe: Principle of operation and performance characteristics. J. Atmos. Oceanic Technol., **15**, 6,1495-1510, 1998.

Kratz, D. P., and Rose, F. G.: Accounting for molecular absorption within the spectral range of the CERES window channel, J. Quant. Spectrosc. Radiat. Transf., 61, 83–95, https://doi.org/10.1016/S0022-4073(97)00203-3, 1999.

Krumpen, T., Von Albedyll, L., Bünger, H. J., Castellani, G., Hartmann, J., Helm, V., Hendricks, S., Hutter, N., Landy, J. C., Lisovski, S., Lüpkes, C., Rohde, J., Suhrhoff, M., and Haas, C.: Smoother sea ice with fewer pressure ridges in a more dynamic Arctic, Nature Climate Change, 15, 66–72, https://doi.org/10.1038/s41558-024-02199-5, 2025

Kulkarni, P., and Wang, J.: New fast integrated mobility spectrometer for real-time measurement of aerosol size distribution - I: Concept and theory, J. Aerosol Sci., 37, 1303–1325, 2006.

Kulkarni, P., and Wang, J.: New fast integrated mobility spectrometer for real-time measurement of aerosol size distribution: II. Design, calibration, and performance characterization, J. Aerosol Sci., 37, 1326–1339, 2006.

https://doi.org/10.5194/essd-2026-241
Preprint. Discussion started: 24 July 2026

Open Access Earth System Science Data Discussions

Kupc, A., Williamson, C., Wagner, N. L., Richardson, M., and Brock, C. A.: Modification, calibration, and performance of the Ultra-High Sensitivity Aerosol Spectrometer for particle size distribution and volatility measurements during the Atmospheric Tomography Mission (ATom) airborne campaign, Atmos. Meas. Tech., 11, 369–383, https://doi.org/10.5194/amt-11-369-2018, 2018.

Kwok, R. and Morison, J.**:** Sea surface height and dynamic topography of the ice-covered oceans from CryoSat-2: 2011–2014, J. Geophys. Res.-Oceans, 121, 674–692, https://doi.org/10.1002/2015JC011357, 2016.

Kurtz, N. (2026). ARCSIX LVIS Freeboard Code Archive (1.0). Zenodo. https://doi.org/10.5281/zenodo.20598957

Kwok, R.: Arctic sea ice thickness, volume, and multiyear ice coverage: losses and coupled variability (1958–2018), Environ. Res. Lett., 13, 105005, https://doi.org/10.1088/1748-9326/aae3ec, 2018.

Kwok, R., Bagnardi, M., Petty, A., and Kurtz, N.: ICESat-2 sea ice ancillary data - Mean Sea Surface Height Grids (1.0) [data set], Zenodo, https://doi.org/10.5281/zenodo.4294048, 2020.

Kwok, R., Kurtz, N., Wimert, J., Petty, A., Cunningham, G., Markus, T., Hancock, D., Ivanoff, A., Bagnardi, M., Herzfeld, U., Trantow, T., and the ICESat-2 Science Team: Ice, Cloud, and Land Elevation Satellite (ICESat-2) Project Algorithm Theoretical Basis Document (ATBD) for Sea Ice Products, Version 7, ICESat-2 Project, https://doi.org/10.5067/KPMXUOH7TNIY, 2025.

Landy J.C., Dawson G.J., Tsamados M., Bushuk M., and coauthors: A year-round satellite sea-ice thickness record from CryoSat-2. Nature. 517-522, https://doi.org/10.1038/s41586-022-05058-5, 2022.

Landy, J., Itkin, P., Polashenski, C., and Matthes, L.: Autonomous weather station measurements in the Central Arctic Ocean, Lincoln Sea and Canadian Arctic for the SI/3D project [data set], Norwegian Polar Institute, https://doi.org/10.21334/NPOLAR.2026.9B81D93D, 2026.

Landy, J., Taelman, C., and Krumpen, T.: IceBird sea ice thickness measurements in the Central Arctic Ocean and Lincoln Sea for the SI/3D project [data set], Norwegian Polar Institute, https://doi.org/10.21334/NPOLAR.2026.59F95D2E, 2026.

Lata, N. N., Zhang, B., Schum, S., Mazzoleni, L., Brimberry, R., Marcus, M. A., Cantrell, W. H., Fialho, P., Mazzoleni, C., and China, S.: Aerosol Composition, Mixing State, and Phase State of Free Tropospheric Particles and Their Role in Ice Cloud Formation, *ACS Earth Space Chem.*, 5, 3499, 2021.

Lata, N. N., Cheng, Z., Dexheimer, D., Zhang, D., Mei, F., and China, S.: Vertical Gradient of Size-Resolved Aerosol Compositions over the Arctic Reveals Cloud Processed Aerosol in-Cloud and above Cloud, Environ. Sci. Technol., 57, 5821–5830, https://doi.org/10.1021/acs.est.2c09498, 2023.

Lawson, R. P., and Cooper, W. A.: Performance of some airborne thermometers in clouds, J. Atmos. Oceanic Technol., 7, 480–494, https://doi.org/10.1175/1520-0426(1990)007<0480:POSATI>2.0.CO;2, 1990.

Lawson, R. P., Stewart, R. E., and Angus, L. J: Observations and numerical simulations of the origin and development of very large snowflakes. J. Atmos. Sciences, 55 (21), 3209-3229, https://doi.org/10.1175/1520-0469(1998)055<3209:OANSOT>2.0.CO;2, 1998.

Lawson, R.P., O'Connor, D., Zmarzly, P., Weaver, K., and coauthors: The 2D-S (Stereo) Probe: Design and preliminary tests of a new airborne, high speed, high-resolution particle imaging probe. J. Atmos. Oceanic Technol., **23**, 1462-1477. https://doi.org/10.1175/JTECH1927.1, 2006.

Lawson, R. P., Gurganus, C.,Woods, S., and R. Bruintjes: Aircraft Observations of Cumulus Microphysics Ranging from the Tropics to Midlatitudes: Implications for a "New" Secondary Ice Process, J. Atmos. Sci., **74**, 2899–2920, https://doi.org/10.1175/JAS-D-17-0033.1, 2017.

Lawson, P., Patnaude, R., & Perkins, R.: *ARCSIX P-3B In-Situ Cloud Data*, NASA Langley Atmospheric Science Data Center Distributed Active Archive Center [data set], https://doi.org/10.5067/SUBORBITAL/ARCSIX/DATA001/P3B/CLOUD_AIRCRAFTINSITU_1, 2025a.

Lawson, P.: ARCSIX Learjet In-Situ Meteorology and Navigation Data, NASA Langley Atmospheric Science Data Center DAAC [data set], https://doi.org/10.5067/SUBORBITAL/ARCSIX/DATA001/Learjet/MetNav_AircraftInSitu_1, 2025b.

https://doi.org/10.5194/essd-2026-241
Preprint. Discussion started: 24 July 2026

Open Access Earth System Science Data Discussions

Lawson, P.: ARCSIX Learjet In-Situ Cloud Data, NASA Langley Atmospheric Science Data Center DAAC [data set], https://doi.org/10.5067/SUBORBITAL/ARCSIX/DATA001/Learjet/Cloud_AircraftInSitu_1, 2025c.

L'Ecuyer, T. S., Drouin, B. J., Anheuser, J., Grames, M., Henderson, D. S., Huang, X., Kahn, B. H., Kay, J. E., Lim, B. H., Mateling, M., Merrelli, A., Miller, N. B., Padmanabhan, S., Peterson, C., Schlegel, N.-J., White, M. L., and Xie, Y.: The Polar Radiant Energy in the Far Infrared Experiment: A New Perspective on Polar Longwave Energy Exchanges, *Bulletin of the American Meteorological Society*, 102, E1431–E1449, https://doi.org/10.1175/BAMS-D-20-0155.1, 2021.

Lenschow, D. E., 1986: Probing the Atmospheric Boundary Layer. Amer. Meteor. Soc., 269 pp.

Lenssen, N. J. L., Schmidt, G. A., Hansen, J. E., Menne, M. J., Persin, A., Ruedy, R., et al.: Improvements in the GISTEMP Uncertainty Model, J. Geophys. Res. Atmos., 124, 6307–6326, https://doi.org/10.1029/2018JD029522, 2019.
Liu, B., et al.: Compact airborne Raman lidar for profiling aerosol, water vapor and clouds, *Optics express*, 22, 20613–20621, 2014.

Lillie, L., Emery, E., Strapp J. W., & Emery, J: A multiwire hot-wire device for measurement of icing severity, total water content, liquid water content, and droplet diameter. 43rd *AIAA Aerospace Sciences Meeting and Exhibit*, 10–13 January 2005. Aerospace Sciences Meetings. Reno, NV, 2005.

Litvinov, P., O. Hasekamp, B. Cairns, and Mishchenko, M.: Reflection models for soil and vegetation surfaces from multiple-viewing angle photopolarimetric measurements, J. Quant. Spectr. Rad. Trans, 111, 529-539, https://doi.org/10.1016/j.jqsrt.2009.11.001, 2011.

Litvinov, P., Hasekamp, O., and Cairns, B.: Models for surface reflection of radiance and polarized radiance: Comparison with airborne multi-angle photopolarimetric measurements and implications for modeling top-of-atmosphere measurements, Remote Sensing of Environment, 115, 781-792, https://doi.org.10.1016/j.rse.2010.11.005, 2011.

Loeb, N. G., and Coauthors: Clouds and the Earth's Radiant Energy System (CERES) Energy Balanced and Filled (EBAF) top-of-atmosphere (TOA) Edition-4.0 data product. J. Climate, **31**, 895–918, https://doi.org/10.1175/JCLI-D-17-0208.1, 2018.

Long, C. N., Bucholtz, A., Jonsson, H., Schmid, B., Vogelmann, A., and Wood, J.: A method of correcting for tilt from horizontal in downwelling shortwave irradiance measurements on moving platforms, Open Atmos. Sci. J., 4, 78–87, https://doi.org/10.2174/1874282301004010078, 2010.

Lorenzo, G. R., Ziemba, L. D., Arellano, A. F., Barth, M. C., Crosbie, E. C., DiGangi, J. P., Diskin, G. S., Ferrare, R., Hilario, M. R. A., Shook, M. A., Tilmes, S., Wang, J., Xiao, Q., Zhang, J., and Sorooshian, A.: Measurement report: Characterization of aerosol hygroscopicity over Southeast Asia during the NASA CAMP^{2}Ex campaign, Atmos. Chem. Phys., 25, 5469–5495, https://doi.org/10.5194/acp-25-5469-2025, 2025.

Lucchesi, R.: File Specification for GEOS FP, GMAO Office Note No. 4 (Version 1.2), 61 pp., 2018.

Maahn, M., Turner, D. D., Lohnert, U., Posselt, D. J., Ebell, K., Mace, G., and Comstock, J.: Optimal Estimation Retrievals and their Uncertainties: What every atmospheric scientist should know, Bull. Amer. Meteor. Soc., 101, E1512–E1523, https://doi.org/10.1175/BAMS-D-19-0027.1, 2020.Magruder, L. A., Neumann, T., Kurtz, N., Sutterley, T. C., Hancock, D., Vornberger, P., and co-authors: Assessment of the Ice, Cloud, and land Elevation Satellite-2 performance against prime mission science requirements. Earth and Space Science, 12, e2025EA004221. https://doi.org/10.1029/2025EA004221, 2025.

Mansoura, X., Cheng, Z., Vandergrift, G. W., Lata, N. N., Sola, V., Rahman, A., Dhas, J., Marcus, M. A., Zhu, Z., Tomlinson, J. M., Schmid, B., Zhang, D., Mei, F., and China, S.: Physicochemical and Molecular Insights into the Boundary Layer and Free Troposphere Aerosol Interactions over the Southern Great Plains, Environ. Sci. Technol., 59, 27648–27656, https://doi.org/10.1021/acs.est.5c10903, 2025.

Marchant, B., Platnick, S., Meyer, K., Arnold, G. T., and Riedi, J.: MODIS Collection 6 shortwave-derived cloud phase classification algorithm and comparisons with CALIOP, *Atmospheric Measurement Techniques*, 9, 1587–1599, https://doi.org/10.5194/amt-9-1587-2016, 2016.

Markus, T., Stroeve, J. C., and Miller, J.: Recent changes in Arctic sea ice melt onset, freezeup, and melt season length, J. Geophys. Res., 114, C12024, https://doi.org/10.1029/2009JC005436, 2009.

https://doi.org/10.5194/essd-2026-241
Preprint. Discussion started: 24 July 2026

Maslowski, W., Clement Kinney, J., Higgins, M., and Roberts, A.:The future of Arctic sea ice. *Annual Review of Earth and Planetary Sciences*, *40*(1), 625-654, https://doi.org/10.1146/annurev-earth-042711-105345, 2012.

Mason B., Wagner, N. L., Adler, G., Andres, E., and coauthors: Intercomparison of aerosol absorption measurements conducted during the SEAC4RS campaign, Aerosol Sci. and Tech., 52(9), 1012-1027, https://doi.org/10.1080/02786826.2018.1500012, 2018.

Mathai, S., Veghte, D., Kovarik, L., Mazzoleni, C., Tseng, K.-P., Bucci, S., Capek, T., Cheng, Z., Marinoni, A., and China, S.: Optical Properties of Individual Tar Balls in the Free Troposphere, Environ. Sci. Technol., 57, 16834–16842, https://doi.org/10.1021/acs.est.3c03498, 2023.

Maturi, E., Harris, A., Mittaz, J., Sapper, J., Wick, G., Zhu, X., Dash, P., and Koner, P.: A new high-resolution Sea Surface Temperature blended analysis, Bull. Amer. Meteor. Soc., 98, 1015–1026, https://doi.org/10.1175/BAMS-D-15-00002.1, 2017.

McCarty, J. L., Aalto, J., Paunu, V.-V., Arnold, S. R., Eckhardt, S., Klimont, Z., Fain, J. J., Evangeliou, N., Venäläinen, A., Tchebakova, N. M., Parfenova, E. I., Kupiainen, K., Soja, A. J., Huang, L., and Wilson, S.: Reviews and syntheses: Arctic fire regimes and emissions in the 21st century, *Biogeosciences*, 18, 5053–5083, https://doi.org/10.5194/bg-18-5053-2021, 2021.

McCluskey, C. S., Hill, T. C. J., Malfatti, F., Sultana, C. M., Lee, C., Santander, M. V., et al.: A dynamic link between ice nucleating particles released in nascent sea spray aerosol and oceanic biological activity during two mesocosm experiments, *Journal of the Atmospheric Sciences*, 74, 151–166, https://doi.org/10.1175/JAS-D-16-0087.1, 2017.

McCluskey, C. S., Ovadnevaite, J., Rinaldi, M., Atkinson, and coauthors: Marine and terrestrial organic ice-nucleating particles in pristine marine to continentally influenced Northeast Atlantic air masses. Journal of Geophysical Research: Atmospheres, 123. https://doi.org/10.1029/2017JD028033, 2018.

McFarquhar, G. M., and Coauthors: Indirect and Semi-Direct Aerosol Campaign. Bull. Amer. Meteor. Soc., 92, 183–201, https://doi.org/10.1175/2010BAMS2935.1, 2011.

McFarquhar, G. M., Baumgardner, D., Bansemer, A., et al.: Processing of Ice Cloud In-Situ Data Collected by Bulk Water, Scattering, and Imaging Probes: Fundamentals, Uncertainties and Efforts towards Consistency. Meteorological Monographs, 58. 11.1-11.3. ISSN: 0065-9401, 2017.

McNaughton, C. S., Clarke, A. D., Freitag, S., Kapustin, V. N., Kondo, Y., Moteki, N., Sahu, L., Takegawa, N., Schwarz, J. P., Spackman, J. R., Watts, L., Diskin, G., Podolske, J., Holloway, J. S., Wisthaler, A., Mikoviny, T., de Gouw, J., Warneke, C., Jimenez, J., Cubison, M., Howell, S. G., Middlebrook, A., Bahreini, R., Anderson, B. E., Winstead, E., Thornhill, K. L., Lack, D., Cozic, J., and Brock, C. A.: Absorbing aerosol in the troposphere of the Western Arctic during the 2008 ARCTAS/ARCPAC airborne field campaigns, Atmos. Chem. Phys., 11, 7561–7582, https://doi.org/10.5194/acp-11-7561-2011, 2011.

Mech, M., Maahn, M., Kneifel, S., Ori, D., Orlandi, E., Kollias, P., Schemann, V., and Crewell, S.: PAMTRA 1.0: the Passive and Active Microwave radiaTive tRAnsfer tool for simulating radiometer and radar measurements of the cloudy atmosphere, Geosci. Model Dev., 13, 4229–4251, https://doi.org/10.5194/gmd-13-4229-2020, 2020.

Meier, W. N., Hovelsrud, G. K., van Oort, B. E. H., Key, J. R., Kovacs, K. M., Michel, C., Haas, C., Granskog, M. A., Gerland, S., Perovich, D. K., Makshtas, A., and Reist, J. D.: Arctic sea ice in transformation: A review of recent observed changes and impacts on biology and human activity, Rev. Geophys., 52, 2013RG000431, https://doi.org/10.1002/2013RG000431, 2014.

Meloni D., Di Sarra A., Muscari G., Di Iorio T., Pace G., Calì Quaglia F., Ciardini V., Tosco M., Bagiacchi P., Cannataro G., Iaccarino A. (2026a). High Resolution Downward Shortwave and Longwave Irradiances at the Thule High Arctic Atmospheric Observatory (THAAO_DSLI_HR) [Dataset]. Agenzia Nazionale per le nuove tecnologie, l'energia e lo sviluppo economico sostenibile (ENEA). https://doi.org/10.13127/thaao/dsli_hr, 2026.

Meloni D., Di Sarra A., Muscari G., Di Iorio T., Pace G., Calì Quaglia F., Ciardini V., Tosco M., Bagiacchi P., Cannataro G., Iaccarino A.. High Resolution Upward Shortwave and Longwave Irradiances at the Thule High Arctic Atmospheric Observatory (THAAO_USLI_HR) [Dataset]. Agenzia Nazionale per le nuove tecnologie, l'energia e lo sviluppo economico sostenibile (ENEA). https://doi.org/10.13127/thaao/usli_hr, 2026.

Meloni D., Di Sarra A., Muscari G., Di Iorio T., Pace G., Calì Quaglia F., Ciardini V., Tosco M., Bagiacchi P., Cannataro G., Iaccarino A. (2026c). All-Sky Camera Images at the Thule High Arctic Atmospheric Observatory (THAAO_SKYCAM)

[Dataset]. Agenzia Nazionale per le nuove tecnologie, l'energia e lo sviluppo economico sostenibile (ENEA). https://doi.org/10.13127/thaao/skycam, 2026.

Meyer, K., Platnick, S., Arnold, G. T., Amarasinghe, N. and coauthors: Evaluating spectral cloud effective radius retrievals from the Enhanced MODIS Airborne Simulator (eMAS) during ORACLES, Atmos. Meas. Tech., 18, 981–1011, https://doi.org/10.5194/amt-18-981-2025, 2025.

Meyer, K.: Taylor et al. ESSD Figure 2 Code and Data. Zenodo. https://doi.org/10.5281/zenodo.20433712, 2026.

Mirrielees, J. A., Kirpes, R. M., Haas, S. M., Rauschenberg, C. D., Matrai, P. A., Remenapp, A., Boschi, V. L., Grannas, A. M., Pratt, K. A., and Ault, A. P.: Probing Individual Particles Generated at the Freshwater–Seawater Interface through Combined Raman, Photothermal Infrared, and X-ray Spectroscopic Characterization, *ACS Measurement Science Au*, 2, 605–619, https://doi.org/10.1021/acsmeasuresciau.2c00041, 2022.

Morrison, H., de Boer, G., Feingold, G., et al.: Resilience of persistent Arctic mixed-phase clouds, *Nature Geosci*, 5, 11–17, https://doi.org/10.1038/ngeo1332, 2012.

Monroe, E. E., Taylor, P. C., and Boisvert, L. N.: Arctic cloud response to a perturbation in sea ice concentration: The North Water polynya. Journal of Geophysical Research: Atmospheres, 126, e2020JD034409. https://doi.org/10.1029/2020JD034409, 2021.

Moore, R. and Nenes, A.: Scanning Flow CCN Analysis—A Method for Fast Measurements of CCN Spectra. Aerosol Sci, and Tech, 43(12), 1192-1207, https://doi.org/10/1080/02786820903289780, 2009.

Moore, R., Shook, M., Ziemba, L., and coauthors: Take-off engine particle emission indices for in-service aircraft at Los Angeles International Airport. Sci Data, 4, 170198. https://doi.org/10.1038/sdata.2017.198, 2017.

Murphy, D. M., et al.: The distribution of sea-salt aerosol in the global troposphere, Atmos. Chem. Phys., 19, 4093–4104, https://doi.org/10.5194/acp-19-4093-2019, 2019.

Muscari, G., di Sarra, A., Di Iorio, T., Meloni, D., Pace, G., Iaccarino, A., Calì Quaglia, F., and Sensale, G.: Integrated Water Vapor at the Thule High Arctic Atmospheric Observatory (THAAO_IWV), https://doi.org/10.13127/THAAO/IWV, 2018a.

Muscari, G., Mevi, G., di Sarra, A., Di Iorio, T., Meloni, D., Pace, G., Iaccarino, A., Calì Quaglia, F., and Sensale, G.: Middle Atmospheric Water vapor vertical Profiles at the Thule High Arctic Atmospheric Observatory (THAAO_MAWP), https://doi.org/10.13127/THAAO/MAWP, 2018b.

Muscari G., Di Sarra A., Di Iorio T., Pace G., Meloni D., Sensale G., Calì Quaglia F., Iaccarino A.: Meteorological data at the Thule High Arctic Atmospheric Observatory (THAAO_Met). Agenzia Nazionale per le nuove tecnologie, l'energia e lo sviluppo economico sostenibile (ENEA), https://doi.org/10.13127/THAAO/MET, 2018c.

Muscari G., Calì Quaglia F., di Sarra A., Ciardini V., Di Iorio T., Meloni D., Pace G., Tosco M., Bagiacchi P., Cannataro, G., Iaccarino A.: Atmospheric radiosonde soundings data from the Thule High Arctic Atmospheric Observatory (THAAO_RS). Agenzia Nazionale per le nuove tecnologie, l'energia e lo sviluppo economico sostenibile (ENEA), https://doi.org/10.13127/THAAO/RS, 2026.

Nakajima, T. and M. King: Determination of the optical thickness and effective particle radius of clouds from reflected solar radiation measurements. Part I- Theory. Journal of the Atmospheric Sciences, 47, 1878–1893, https://doi.org/10.1175/1520-0469(1990)047<1878:DOTOTA>2.0.CO;2, 1990.

NASA/LARC/SD/ASDC: CER_BDS_Terra-FM2_Edition4, NASA Langley Atmospheric Science Data Center DAAC [data set], https://doi.org/10.5067/TERRA/CERES/BDS_TERRA-FM2_L1.004, 2025a.

NASA/LARC/SD/ASDC: CERES Clouds and Radiative Swath Terra FM1 MODIS Edition4a, NASA Langley Atmospheric Science Data Center DAAC [data set], https://doi.org/10.5067/TERRA/CERES/CRS_TERRA-FM1_L2.004A, 2025b.

NASA/LARC/SD/ASDC: CERES Clouds and Radiative Swath Terra FM2 MODIS Edition4a, NASA Langley Atmospheric Science Data Center DAAC [data set], https://doi.org/10.5067/TERRA/CERES/CRS_TERRA-FM2_L2.004A, 2025c.

https://doi.org/10.5194/essd-2026-241
Preprint. Discussion started: 24 July 2026

NASA/LARC/SD/ASDC: CERES Clouds and Radiative Swath Aqua FM3 MODIS Edition4a, NASA Langley Atmospheric Science Data Center DAAC [data set], https://doi.org/10.5067/AQUA/CERES/CRS_AQUA-FM3_L2.004A, 2025d.

Nehrir, A: ARCSIX LaRC G-III High Altitude Lidar Observatory (HALO) Data [Dataset]. NASA Langley Atmospheric Science Data Center Distributed Active Archive Center. https://doi.org/10.5067/SUBORBITAL/ARCSIX/DATA001/G3/AIRCRAFTREMOTESENSING/HALO_1, 2025.

Nataraja, V.: Taylor et al. ARCSIX ESSD Figure 1a and Figure 4 Code and Data [Data set]. Zenodo. https://doi.org/10.5281/zenodo.20433892, 2026.

Neumann, T.A., Martino, A. J. Markus, T., Bae, S., and coauthors: The Ice, Cloud, and Land Elevation Satellite-2 mission: A global geolocated photon product derived from the Advanced Topographic Laser Altimeter System, Remote Sens. Environ., 233, https://doi.org/10.1016/j.rse.2019.111325, 2019.

Norgren, M. S., Wood, J., Schmidt, K. S., van Diedenhoven, B., Stamnes, S. A., Ziemba, L. D., Crosbie, E. C., Shook, M. A., Kittelman, A. S., LeBlanc, S. E., Broccardo, S., Freitag, S., and Reid, J. S.: Above-aircraft cirrus cloud and aerosol optical depth from hyperspectral irradiances measured by a total-diffuse radiometer, Atmos. Meas. Tech., 15, 1373, https://doi.org/10.5194/amt-15-1373-2022, 2022.

Northup, E., Aikin, K., Webster, C., & Chen, Gao: *ESDS Standards.* Retrieved from ICARTT File Format Standards V2.0: https://www.earthdata.nasa.gov/s3fs-public/imported/ESDS-RFC-029v2.pdf, 2017.

Oleson, K. W., Lawrence, D. M., Bonan, G. B., Drewniak, B., Huang, M., Koven, C., et al.: Technical description of version 4.5 of the Community Land Model (CLM), https://doi.org/10.5065/D6RR1W7M, 2013.

Olfert, J. S., Kulkarni, P., and Wang, J.: Measuring aerosol size distributions with the fast integrated mobility spectrometer, J. Aerosol Sci., 39, 940–956, 2008.Ottaviani, M., Chowdhary, J., Cairns, B.: Remote sensing of the ocean surface refractive index via short-wave infrared polarimetry. Remote Sens. Environ., 221, 14-23, doi:10.1016/j.rse.2018.10.016, 2019.

Ottaviani M, van Diedenhoven B, Cairns B: Photopolarimetric retrievals of snow properties. The Cryosphere 9, 1933–1942, https://doi.org/10.5194/tc-9-1933-2015, 2015.

Pace, G., Muscari, G., di Sarra, A., Calì Quaglia, F., Meloni, D., Iaccarino, A., and Di Iorio, T.: Infrared Brightness Temperature at the Thule High Arctic Atmospheric Observatory (THAAO_IBT), https://doi.org/10.12910/DATASET2023-001, 2023a.

Pace, G., Muscari, G., di Sarra, A., Calì Quaglia, F., Meloni, D., Iaccarino, A., and Di Iorio, T.: Integrated Water Vapor measured by an HATPRO microwave radiometer at the Thule High Arctic Atmospheric Observatory (THAAO_IWV_HATPRO), https://doi.org/10.12910/DATASET2023-002, 2023b.

Pace, G., Muscari, G., di Sarra, A., Calì Quaglia, F., Meloni, D., Iaccarino, A., and Di Iorio, T.: Liquid Water Path by an HATPRO microwave radiometer at the Thule High Arctic Atmospheric Observatory (THAAO_LWP_HATPRO), https://doi.org/10.12910/DATASET2023-003, 2023c.

Painter, T. H., Seidel, F. C., Bryant, A. C., McKenzie Skiles, S., and Rittger, K.: Imaging spectroscopy of albedo and radiative forcing by light-absorbing impurities in mountain snow, J. Geophys. Res. Atmos., 118, 9511–9523, https://doi.org/10.1002/jgrd.50520, 2013.

Painemal, D., and Zuidema, P.: The first aerosol indirect effect quantified through airborne remote sensing during VOCALS-REx, Atmos. Chem. Phys., 13, 917–931, https://doi.org/10.5194/acp-13-917-2013, 2013.

Pazmany, A.L. and S.J. Haimov: Coherent power measurements with a compact airborne Ka-band precipitation radar. J. Atmos. Oceanic Technol., **35**, 3–20. https://doi.org/10.1175/JTECH-D-17-0058.1, 2018.

Pearson, R., Phillips, S., Loranty, M., et al.: Shifts in Arctic vegetation and associated feedbacks under climate change, *Nature Clim Change*, 3, 673–677, https://doi.org/10.1038/nclimate1858, 2013.

Perez, M. and Zuidema, P.: ARCSIX P-3B G-band Vapor Radiometer Data, NASA Langley Atmospheric Science Data Center Distributed Active Archive Center [data set], 2026.

Perkins, R.: ARCSIX ESSD fig7. Zenodo. https://doi.org/10.5281/zenodo.20647607, 2026.

Petty, A. A., Kurtz, N. T., Kwok, R., Markus, T., Neumann, T. A., Keeney, N., & Cabaj, A. ICESat-2 L4 Monthly Gridded Sea Ice Thickness (IS2SITMOGR4, Version 4). [Data set]. Boulder, Colorado USA. NASA National Snow and Ice Data Center Distributed Active Archive Center. https://doi.org/10.5067/TXDHDJ1JT0CG, 2025.

Pilewskie, P. J., and Coauthors: Solar spectral radiative forcing during the Southern African Regional Science Initiative, J. Geophys. Res., 108, 8486, https://doi.org/10.1029/2002JD002411, 2003.

Pisso, I., Sollum, E., Grythe, H., Kristiansen, N. I., Cassiani, M., Eckhardt, S., Arnold, D., Morton, D., Thompson, R. L., Groot Zwaaftink, C. D., Evangeliou, N., Sodemann, H., Haimberger, L., Henne, S., Brunner, D., Burkhart, J. F., Fouilloux, A., Brioude, J., Philipp, A., Seibert, P., and Stohl, A.: The Lagrangian particle dispersion model FLEXPART version 10.4, Geosci. Model Dev., 12, 4955–4997, https://doi.org/10.5194/gmd-12-4955-2019, 2019.

Planck, C.J., Whitlock, J., Polashenski, C., Perovich, D.: The evolution of the seasonal ice mass balance buoy, Cold Regions Science and Technology, 165, https://doi.org/10.1016/j.coldregions.2019.102792, 2019.

Platnick S, Meyer K.G., King M.D., Wind G.,and coauthors: The MODIS cloud optical and microphysical products: Collection 6 updates and examples from Terra and Aqua, IEEE Trans Geosci Remote Sens, 55(1), 502-525, http://doi.org/10.1109/TGRS.2016.2610522, 2017.

Platnick, S., Meyer, K., Wind, G., Holz, R. E., Amarasinghe, N., Hubanks, P. A., et al.: The NASA MODIS-VIIRS Continuity Cloud Optical Properties Products, *Remote Sensing*, 13, 2, https://doi.org/10.3390/rs13010002, 2021.

Polashenski, C., Perovich, D. K., Richter-Menge, J.A., Elder, B.: Seasonal ice mass-balance buoys: adapting tools to the changing Arctic, Ann. Glaciol., 52(57), 18-26, https://doi.org/10.3189/172756411795931516, 2011.

Polashenski, C., Perovich, D., Raphael, I., and Planck, C.: *Ice Mass Balance Buoys 2024*. Arctic Data Center [Data set], https://doi.org/10.18739/A2T14TR46, 2025.

Polyakov, I. V., Bhatt, U. S., Walsh, J. E., Abrahamsen, E. P., Pnyushkov, A. V., and Wassmann, P. F.: Recent oceanic changes in the Arctic in the context of long-term observations, *Ecological Applications*, 23, 1745–1764, https://doi.org/10.1890/11-0902.1, 2013.

Popovicheva, O. B., Chichaeva, M. A., Evangeliou, N., Eckhardt, S., Diapouli, E., & Kasimov, N. S.: Multi-year black carbon observations and modeling close to the largest gas flaring and wildfire regions in the Western Siberian Arctic", Atmospheric Chemistry & Physics, 25, 7719-7739, https://doi.org/10.5194/acp-25-7719-2025, 2025.

Pratt, K. A., and Prather, K. A.: Aircraft measurements of vertical profiles of aerosol mixing states, J. Geophys. Res., 115, D11305, https://doi.org/10.1029/2009JD013150, 2010.

Pratt, K. A., and Prather, K. A.: Mass spectrometry of atmospheric aerosols - Recent developments & applications Part II: On-line mass spectrometry techniques, Mass Spectrom. Rev., 31, 17–48, 2012.

Pratt, K. A., Mayer, J. E., Holecek, J. C., Moffet, R. C., Sanchez, R. O., Rebotier, T. P., Furutani, H., Gonin, M., Fuhrer, K., Su, Y., Guazzotti, S., and Prather, K. A.: Development and Characterization of an Aircraft Aerosol Time-of-Flight Mass Spectrometer, Anal. Chem., 81, 1792–1800, https://doi.org/10.1021/ac801942r, 2009.

Randles, C. A., Silva, A. M. da, Buchard, V., Colarco, P. R., Darmenov, A., Govindaraju, R., Smirnov, A., Holben, B., Ferrare, R., Hair, J., Shinozuka, Y., and Flynn, C. J.: The MERRA-2 Aerosol Reanalysis, 1980 Onward. Part I: System Description and Data Assimilation Evaluation, J. Climate, https://doi.org/10.1175/jcli-d-16-0609.1, 2017.

Rantanen, M., Karpechko, A. Y., Lipponen, A., et al.: The Arctic has warmed nearly four times faster than the globe since 1979, *Commun Earth Environ*, 3, 168, https://doi.org/10.1038/s43247-022-00498-3, 2022.

Raphael, I., Perovich, D., and Polashenski, C.: *Snow Thickness and Temperature Observation System (SnoTATOS) snow depth and surface melt observations from the 2024 Arctic Radiation Cloud Aerosol Surface Interaction Experiment (ARCSIX) campaign, Lincoln Sea [Data set]*. Arctic Data Center, https://doi.org/10.18739/A2FJ29F6X, 2025.

Redemann, J., Wood, R., Zuidema, P., Doherty, S. J., Luna, B., LeBlanc, S. E., Diamond, M. S., Shinozuka, Y., Chang, I. Y., Ueyama, R., Pfister, L., Ryoo, J.-M., Dobracki, A. N., da Silva, A. M., Longo, K. M., Kacenelenbogen, M. S., Flynn, C. J., Pistone, K., Knox, N. M., Piketh, S. J., Haywood, J. M., Formenti, P., Mallet, M., Stier, P., Ackerman, A. S., Bauer, S. E.,

https://doi.org/10.5194/essd-2026-241
Preprint. Discussion started: 24 July 2026

Open Access Earth System Science Data Discussions

Fridlind, A. M., Carmichael, G. R., Saide, P. E., Ferrada, G. A., Howell, S. G., Freitag, S., Cairns, B., Holben, B. N., Knobelspiesse, K. D., Tanelli, S., L'Ecuyer, T. S., Dzambo, A. M., Sy, O. O., McFarquhar, G. M., Poellot, M. R., Gupta, S., O'Brien, J. R., Nenes, A., Kacarab, M., Wong, J. P. S., Small-Griswold, J. D., Thornhill, K. L., Noone, D., Podolske, J. R., Schmidt, K. S., Pilewskie, P., Chen, H., Cochrane, S. P., Sedlacek, A. J., Lang, T. J., Stith, E., Segal-Rozenhaimer, M., Ferrare, R. A., Burton, S. P., Hostetler, C. A., Diner, D. J., Seidel, F. C., Platnick, S. E., Myers, J. S., Meyer, K. G., Spangenberg, D. A., Maring, H., and Gao, L.: An overview of the ORACLES (ObseRvations of Aerosols above CLouds and their intEractionS) project: aerosol–cloud–radiation interactions in the southeast Atlantic basin, Atmos. Chem. Phys., 21, 1507–1563, https://doi.org/10.5194/acp-21-1507-2021, 2021.

Redemann, J., and Gao, L.: A machine learning paradigm for necessary observations to reduce uncertainties in aerosol climate forcing, *Nature Communications*, 15, 8343, https://doi.org/10.1038/s41467-024-52747-y, 2024.

Reid, J. S., Maring, H. B., Narisma, G. T., van den Heever, S., Di Girolamo, L., and coauthors: The Coupling Between Tropical Meteorology, Aerosol Lifecycle, Convection, and Radiation during the Cloud, Aerosol and Monsoon Processes Philippines Experiment (CAMP2Ex), B. Am. Meteorol. Soc., 104, E1179– E1205, https://doi.org/10.1175/BAMS-D-21-0285.1, 2023.

Rogers, D. C., DeMott, P. J., Kreidenweis, and Y. Chen: A Continuous Flow Diffusion Chamber for Airborne Measurements of Ice Nuclei. J. Atmos. Oceanic Technol., 18, 725-741, https://doi.org/10.1175/1520-0426(2001)018<725:ACFDCF>2.0.CO;2, 2001.

Rutan, D. A., S. Kato, D. R. Doelling, F. G. Rose, L. T. Nguyen, T. E. Caldwell, and N. G. Loeb: CERES synoptic product: Methodology and validation of surface radiant flux. *J. Atmos. Oceanic Technol.*, **32**, 1121–1143, https://doi.org/10.1175/JTECH-D-14-00165.1, 2015.

Schill, G. P., et al.: Widespread biomass burning smoke throughout the remote troposphere, *Nature Geoscience*, 13, 422–427, https://doi.org/10.1038/s41561-020-0586-1, 2020.

Schmidt, K. S., and P. Pilewskie: Airborne measurements of spectral shortwave radiation in cloud and aerosol remote sensing and energy budget studies. Light Scattering Reviews 6: Light Scattering and Remote Sensing of Atmosphere and Surface, A. A. Kokhanovsky, Ed., Springer, 239–288, https://doi.org/10.1007/978-3-642-15531-4_6, 2012.

Schmidt, K. S., Wendisch, M., and Kindel, B.: Airborne Solar Radiation Sensors, in: *Springer Handbook of Atmospheric Measurements*, edited by: Foken, T., Springer, Cham, https://doi.org/10.1007/978-3-030-52171-4_40, 2021.

Schlosser, J., and Stamnes, S.: ARCSIX P-3B Analysis Data, NASA Langley Atmospheric Science Data Center DAAC [data set], https://doi.org/10.5067/SUBORBITAL/ARCSIX/DATA001/P3B/Analysis_1, 2025a.

Schlosser, J., and Stamnes, S.: ARCSIX LaRC G-III Analysis Data, NASA Langley Atmospheric Science Data Center DAAC [data set], https://doi.org/10.5067/SUBORBITAL/ARCSIX/DATA001/G3/Analysis_1, 2025b.

Schwarz, J. P., Gao, R. S., Fahey, D. W., Thomson, D.S., and coauthors: Single-particle measurements of midlatitude black carbon and light-scattering aerosols from the boundary layer to the lower stratosphere, J. Geophys. Res., 111, D16207, https://doi.org/10.1029/2006JD007076, 2006.

Sharpe, S., Li, Y., Benjemia, S., Rivera-Adorno, F., Olayemi, T., Ese, J., Shen, X., Fraund, M., Moffet, R., Lata, N. N., Cheng, Z., China, S., Homeyer, C. R., Dykema, J., Marcus, M. A., Wang, J., Cziczo, D., Keutsch, F., and Laskin, A.: Chemical imaging of individual stratospheric particles sampled over North America, *Environmental Science: Atmospheres*, 6, 47–60, https://doi.org/10.1039/D5EA00127G, 2026.

Shingler, T., Dey, S., Sorooshian, A., Brechtel, F. J., Wang, Z., Metcalf, A., Coggon, M., Mulmenstadt, J., Russell, L. M., Jonsson, H. H., and Seinfeld, J. H.: Characterisation and airborne deployment of a new counterflow virtual impactor inlet, *Atmospheric Measurement Techniques*, 5, 1259–1269, https://doi.org/10.5194/amt-5-1259-2012, 2012.

Shingler, T., Sorooshian, A., Ortega, A., Crosbie, E., Wonaschütz, A., Perring, A. E., Beyersdorf, A., Ziemba, L., Jimenez, J. L., Campuzano-Jost, P., Mikoviny, T., Wisthaler, A., and Russell, L. M.: Ambient observations of hygroscopic growth factor and f(RH) below 1: Case studies from surface and airborne measurements, *Journal of Geophysical Research: Atmospheres*, 121, 661–677, https://doi.org/10.1002/2016JD025471, 2016a.

https://doi.org/10.5194/essd-2026-241
Preprint. Discussion started: 24 July 2026

Shingler, T., Crosbie, E., Ortega, A., Shiraiwa, M., Zuend, A., Beyersdorf, A., Ziemba, L., Anderson, B., Thornhill, L., Perring, A. E., Schwarz, J. P., Campazano-Jost, P., Day, D. A., Jimenez, J. L., Hair, J. W., Mikoviny, T., Wisthaler, A., and Sorooshian, A.: Airborne characterization of subsaturated aerosol hygroscopicity and dry refractive index from the surface to 6.5km during the SEAC4RS campaign, *Journal of Geophysical Research*, 121, 4188–4210, https://doi.org/10.1002/2015JD024498, 2016b.

Sinclair, K., van Diedenhoven, B., Cairns, B. , Yorks, J., Wasilewski, A., and McGill, M.: Remote sensing of multiple cloud layer heights using multi-angular measurements. Atmos. Meas. Tech., **10**, 2361-2375, https://doi.org/10.5194/amt-10-2361-2017, 2017.

Sledd, A., and L'Ecuyer, T.: How Much Do Clouds Mask the Impacts of Arctic Sea Ice and Snow Cover Variations? Different Perspectives from Observations and Reanalyses, *Atmosphere*, 10, 12, https://doi.org/10.3390/atmos10010012, 2019.

Smith, W. L., and co-authors: Arctic Radiation-IceBridge Sea and Ice Experiment (ARISE): The Arctic Radiant Energy System During the Critical Seasonal Ice Transition, Bull. Amer. Meteor. Soc., 98, 1399–1427, https://doi.org/10.1175/BAMS-D-14-00277.1, 2017.

Smith, S. L., O'Neill, H. B., Isaksen, K., et al.: The changing thermal state of permafrost, *Nat Rev Earth Environ*, 3, 10–23, https://doi.org/10.1038/s43017-021-00240-1, 2022.

Solomon, A., et al.: Description and Evaluation of the NOAA Experimental Coupled Arctic Forecast System (CAFS) Model, https://doi.org/10.25923/v7vj-z744, 2024.

Song, X. H., Hopke, P. K., Fergenson, D. P., and Prather, K. A.: Classification of single particles analyzed by ATOFMS using an artificial neural network, ART-2A, Anal. Chem., 71, 860–865, 1999.

Sorooshian, A., Hersey, S., Brechtel, F. J., Corless, A., Flagan, R. C., and Seinfeld, J. H.: Rapid, Size-Resolved Aerosol Hygroscopic Growth Measurements: Differential Aerosol Sizing and Hygroscopicity Spectrometer Probe (DASH-SP), *Aerosol Science and Technology*, 42, 445–464, https://doi.org/10.1080/02786820802178506, 2008.

Sorooshian, A., Alexandrov, M. D., Bell, A. D., Bennett, R., Betito, G., Burton, S. P., Buzanowicz, M. E., Cairns, B., Chemyakin, E. V., Chen, G., Choi, Y., Collister, B. L., Cook, A. L., Corral, A. F., Crosbie, E. C., van Diedenhoven, B., DiGangi, J. P., Diskin, G. S., Dmitrovic, S., Edwards, E. L., Fenn, M. A., Ferrare, R. A., van Gilst, D., Hair, J. W., Harper, D. B., Hilario, M. R. A., Hostetler, C. A., Jester, N., Jones, M., Kirschler, S., Kleb, M. M., Kusterer, J. M., Leavor, S., Lee, J. W., Liu, H., McCauley, K., Moore, R. H., Nied, J., Notari, A., Nowak, J. B., Painemal, D., Phillips, K. E., Robinson, C. E., Scarino, A. J., Schlosser, J. S., Seaman, S. T., Seethala, C., Shingler, T. J., Shook, M. A., Sinclair, K. A., Smith Jr, W. L., Spangenberg, D. A., Stamnes, S. A., Thornhill, K. L., Voigt, C., Vömel, H., Wasilewski, A. P., Wang, H., Winstead, E. L., Zeider, K., Zeng, X., Zhang, B., Ziemba, L. D., and Zuidema, P.: Spatially coordinated airborne data and complementary products for aerosol, gas, cloud, and meteorological studies: the NASA ACTIVATE dataset, Earth Syst. Sci. Data, 15, 3419–3472, https://doi.org/10.5194/essd-15-3419-2023, 2023.

Sorooshian, A., Siu, L. W., Butler, K., Brunke, M. A., Cairns, B., Chellappan, S., Chen, J., Choi, Y., Crosbie, E. C., Cutler, L., DiGangi, J. P., Diskin, G. S., Ferrare, R. A., Hair, J. W., Hostetler, C. A., Kirschler, S., Kleb, M. M., Li, X.-Y., Liu, H., McComiskey, A., Namdari, S., Painemal, D., Schlosser, J. S., Shingler, T., Shook, M. A., Silva, S., Sinclair, K., Smith, W. L., Soloff, C., Stamnes, S., Tang, S., Thornhill, K. L., Tornow, F., Tselioudis, G., Van Diedenhoven, B., Voigt, C., Vömel, H., Wang, H., Winstead, E. L., Xu, Y., Zeng, X., Zhang, B., Ziemba, L., and Zuidema, P.: The NASA ACTIVATE Mission, *Bulletin of the American Meteorological Society*, 106, E1517–E1538, https://doi.org/10.1175/BAMS-D-24-0136.1, 2025.

Stamnes, S., Hostetler, C., Ferrare, R., Burton, and coauthors.: Simultaneous polarimeter retrievals of microphysical aerosol and ocean color parameters from the "MAPP" algorithm with comparison to high-spectral-resolution lidar aerosol and ocean products, Appl. Optics, 57, 2394-2413, https://doi.org/10.1364/AO.57.002394, 2018.

Stohl, A., Forster, C., Frank, A., Seibert, P., and Wotawa, G.: Technical note: The Lagrangian particle dispersion model FLEXPART version 6.2, Atmos. Chem. Phys., 5, 2461–2474, https://doi.org/10.5194/acp-5-2461-2005, 2005.

Stroeve, J., and Notz, D.: Changing state of Arctic sea ice across all seasons, Environ. Res. Lett., 13, 103001, https://doi.org/10.1088/1748-9326/aade56, 2018.

Sultana, C. M., Cornwell, G. C., Rodriguez, P., and Prather, K. A.: FATES: a flexible analysis toolkit for the exploration of single-particle mass spectrometer data, Atmos. Meas. Tech., 10, 1323–1334, 2017.

https://doi.org/10.5194/essd-2026-241
Preprint. Discussion started: 24 July 2026

Sutterley, T. C., Howard, S. L., Padman, L., and Seigfried, M. R.: pyTMD: Python-based tidal prediction software. J. of Open Source Software, https://doi.org/10.21105/joss.08566, 2025.

Tan, I., Sotiropoulou, G., Taylor, P. C., Zamora, L., and Wendisch, M.: A Review of the Factors Influencing Arctic Mixed-Phase Clouds: Progress and Outlook, in: *Clouds and Their Climatic Impacts*, edited by: Sullivan, S. C. and Hoose, C., https://doi.org/10.1002/9781119700357.ch5, 2023.

Taylor, P. C., Kato, S., Xu, K.-M., and Cai, M.: Covariance between Arctic sea ice and clouds within atmospheric state regimes at the satellite footprint level. J. Geophys. Res. Atmos., 120, 12656-12678, doi:10.1002/2015JD023520, 2015.

Taylor, P. C., Hegyi, B. M., Boeke, R. C., and Boisvert, L. N.: On the increasing importance of air-sea exchange in a thawing Arctic: A review, *Atmosphere*, 9, 41, https://doi.org/10.3390/atmos9020041, 2018.

Taylor P. C., Boeke R. C., Boisvert L. N, Feldl N., Henry M., Huang Y., Langen P. L., Liu W., Pithan F., Sejas S. A. and Tan I: Process Drivers, Inter-Model Spread, and the Path Forward: A Review of Amplified Arctic Warming. Front. Earth Sci. 9:758361. doi: 10.3389/feart.2021.758361, 2022a.

Taylor, P. C., Itterly, K., Corbet, J., Bucholtz, A., Sejas, S., Su, W., Doeling, D., and Kato, S.: A Comparison of Top-of-Atmosphere Radiative Fluxes from CERES and ARISE, J. Geophys. Res., 127, e2022JD037473, https://doi.org/10.1029/2022JD037573, 2022b.

Tilling, R. L., Ridout, A., and Shepherd, A.: Estimating Arctic sea ice thickness and volume using CryoSat-2 radar altimeter data, *Advances in Space Research*, 62, 1203–1225, https://doi.org/10.1016/j.asr.2017.10.051, 2018.

Thompson, D. R., McCubbin, I., Gao, B. C., Green, R. O., Matthews, A. A., Mei, F., and coauthors: Measuring cloud thermodynamic phase with shortwave infrared imaging spectroscopy. Journal of Geophysical Research: Atmospheres, 121(15), 9174-9190, 2016.

Thompson, D. R., Natraj, V., Green, R. O., Helmlinger, M. C., Gao, B.-C., & Eastwood, M. L. (2018). Optimal estimation for imaging spectrometer atmospheric correction. *Remote Sensing of Environment*, 216, 355–373. https://doi.org/10.1016/j.rse.2018.07.003, 2018.

Thompson, D. R., A. K.Thorpe, C. Frankenberg, R. O. Green, R. Duren, L. Guanter, A. Hollstein, E. Middleton, L. Ong, and S. Ungar: Space-based remote imaging spectroscopy of the Aliso Canyon CH4 superemitter, *Geophys. Res. Lett.*, 43, 6571–6578, https://doi.org/10.1002/2016GL069079, 2016.

Thompson, D. R., Babu, K., Braverman, A. J., Eastwood, M. L., Green, R. O., Hobbs, J. M., and coauthors: Optimal estimation of spectral surface reflectance in challenging atmospheres. Remote Sensing of Environment, 232, 111258. https://doi.org/10.1016/j.rse.2019.111258, 2019.

Thompson, D. R., Kahn, B. H., Brodrick, P. G., Lebsock, M. D., Richardson, M., and Green, R. O.: Spectroscopic imaging of sub-kilometer spatial structure in lower-tropospheric water vapor, Atmos. Meas. Tech., 14, 2827–2840, https://doi.org/10.5194/amt-14-2827-2021, 2021.

Thornhill, K. L., Anderson, B. E., Barrick, J. D. W., Bagwell, D. R., Friesen, R., and Lenschow, D. H.: Air motion intercomparison flights during Transport and Chemical Evolution in the Pacific (TRACE-P)/ACE-ASIA, J. Geophys. Res., 108(D20), 9001, https://doi.org/10.1029/2002JD003108, 2003.

Thornhill, K. L.: ARCSIX LaRC G-III Dropsonde Data, NASA Langley Atmospheric Science Data Center DAAC [data set], https://doi.org/10.5067/SUBORBITAL/ARCSIX/DATA001/G3/Dropsondes_1, 2025.

Tjernström, M., Leck, C., Birch, C. E., Bottenheim, J. W., Brooks, B. J., Brooks, I. M., Bäcklin, L., Chang, R. Y.-W., de Leeuw, G., Di Liberto, L., et al.: The Arctic Summer Cloud Ocean Study (ASCOS): overview and experimental design, Atmos. Chem. Phys., 14, 2823–2869, https://doi.org/10.5194/acp-14-2823-2014, 2014.

Tobo, Y., Prenni, A. J., DeMott, P. J., Huffman, J. A., McCluskey, C. S., Tian, G., et al.: Biological aerosol particles as a key determinant of ice nuclei populations in a forest ecosystem, Journal of Geophysical Research: Atmosphere*s*, 118, 10100–10110, https://doi.org/10.1002/jgrd.50801, 2013.

https://doi.org/10.5194/essd-2026-241
Preprint. Discussion started: 24 July 2026

Twohy, C. H., Schanot, A. J. and Cooper, W.A.: Measurement of condensed water content in liquid and ice clouds using an airborne counterflow virtual impactor. J. Atmos. Oceanic Tech., 14, 197–202, https://doi.org/10.1175/1520-0426(1997)014<0197:MOCWCI>2.0.CO;2, 1996.

Ueyama, R., Smith, W. P., Brown, M., Jensen, E. J., Ziemba, L., Bui, T. P., Dean-Day, J., and Williamson, C. J.: On the fate of aerosols produced by new particle formation in the upper troposphere and lower stratosphere, *Geophysical Research Letters*, 52, e2025GL116860, https://doi.org/10.1029/2025GL116860, 2025.

Valdelomar, P., Gómez-Amo, J. L., Peris-Ferrús, C., Scarlatti, F., and Utrillas, M. P.: Feasibility of ground-based sky-camera HDR imagery to determine solar irradiance and Sky Radiance over different geometries and Sky Conditions, *Remote Sensing*, 13, 5157, https://doi.org/10.3390/rs13245157, 2021.

Vali, G.: Quantitative evaluation of experimental results on the heterogeneous freezing nucleation of supercooled liquids, J. Atmos. Sci., 28, 402–409, 1971.

Vay, S. A., Choi, Y., Vadrevu, K.P., Blake, D.R., and coauthors: Patterns of CO2 and radiocarbon across high northern latitudes during International Polar Year 2008, *J. Geophys. Res.*, 116, D14301, https://doi.org/10.1029/2011JD015643, 2011.

Veghte, D. P., China, S., Weis, J., Lin, P., Hinks, M. L., Kovarik, L., Nizkorodov, S. A., Gilles, M. K., and Laskin, A.: Heating-Induced Transformations of Atmospheric Particles: Environmental Transmission Electron Microscopy Study, Anal. Chem., 90, 9761–9768, https://doi.org/10.1021/acs.analchem.8b01410, 2018.

Verlinde, J., and Coauthors, 2007: The Mixed-Phase Arctic Cloud Experiment. Bull. Amer. Meteor. Soc., 88, 205–222, https://doi.org/10.1175/BAMS-88-2-205, 2007.

Vinogradova, A. A., Kopeikin, V. M., Vasileva, A. V., Smirnov, N. S., and Ivanova, Yu. A.: Concentration of Black Carbon in the Near-Surface Atmosphere in the Pechora-Ilych Natural Reserve: Measurements and Merra-2 Reanalysis, Izv. Atmos. Ocean. Phys., 56, 1191–1201, https://doi.org/10.1134/S0001433820100084, 2020.

Virkkula, A.: Correction of the Calibration of the 3-wavelength Particle Soot Absorption Photometer (PSAP), Aerosol Sci. Technol., 44, 706–712, https://doi.org/10.1080/02786826.2010.482110, 2010.

Vömel, H., Goodstein, M., Tudor, L., Witte, J., Fuchs-Stone, and coauthors: High-resolution in situ observations of atmospheric thermodynamics using dropsondes during the Organization of Tropical East Pacific Convection (OTREC) field campaign, Earth Syst. Sci. Data, 13, 1107–1117, https://doi.org/10.5194/essd-13-1107-2021, 2021.

Vömel, H., Sorooshian, A., Robinson, C., Shingler, T. J., Thornhill, K. L., and Ziemba, L. D.: Dropsonde observations during the Aerosol Cloud meTeorology Interactions oVer the western ATlantic Experiment, Sci. Data, 10, 753, https://doi.org/10.1038/s41597-023-02647-5, 2023.

Waquet, F., Cairns, B., Knobelspiesse, K., Chowdhary, J., and coauthors: Polarimetric remote sensing of aerosols over land, J. Geophys. Res., 114, D01206, https://doi.org/10.1029/2008JD010619, 2009.

Wang, J.: A fast integrated mobility spectrometer with wide dynamic size range: Theoretical analysis and numerical simulation, J. Aerosol Sci., 40, 890–906, 2009.

Wang, J., Krejci, R., Giangrandel, S., Kuang, C., Barbosa, H. M. J., Brito, J., Carbone, S., Chi, X. G., Comstock, J., Ditas, F., Lavric, J., Manninen, H. E., Mei, F., Moran-Zuloaga, D., Pohlker, C., Pohlker, M. L., Saturno, J., Schmid, B., Souza, R. A. F., Springston, S. R., Tomlinson, J. M., Toto, T., Walter, D., Wimmer, D., Smith, J. N., Kulmala, M., Machado, L. A. T., Artaxo, P., Andreae, M. O., Petaja, T., and Martin, S. T.: Amazon boundary layer aerosol concentration sustained by vertical transport during rainfall, *Nature*, 539, 416–419, https://doi.org/10.1038/nature19819, 2016.

Wang, J., Pikridas, M., Spielman, S. R., and Pinterich, T.: A fast integrated mobility spectrometer for rapid measurement of sub-micrometer aerosol size distribution, Part I: Design and model evaluation, J. Aerosol Sci., 108, 44–55, https://doi.org/10.1016/j.jaerosci.2017.02.012, 2017.

Wang, Y., Pinterich, T., and Wang, J.: Rapid measurement of sub-micrometer aerosol size distribution using a fast integrated mobility spectrometer, J. Aerosol Sci., 121, 12–20, https://doi.org/10.1016/j.jaerosci.2018.03.006, 2018.

Wang, Z: ARCSIX P-3B Aircraft Multi-function Airborne Raman Lidar (MARLi) Data, NASA Langley Atmospheric Science Data Center DAAC [data set], https://doi.org/10.5067/SUBORBITAL/ARCSIX/DATA001/P3B/AircraftRemoteSensing/MARLi_1, 2025.

Wei, Y., Shrestha, R., Pal, S., Gerken, T., and coauthors: Atmospheric Carbon and Transport – America (ACT-America) Data Sets: Description, Management, and Delivery, Earth and Space Science, 8, e2020EA001634, https://doi.org/10.1029/2020EA001634, 2021.

Wendisch, M., Müller, D., Schell, D., and Heintzenberg, J.: An Airborne Spectral Albedometer with Active Horizontal Stabilization, J. Atmos. Oceanic Technol., 18, 1856–1866, https://doi.org/10.1175/1520-0426(2001)018<1856:AASAWA>2.0.CO;2, 2001.

Wendisch, M., Brückner, M., Crewell, S., Ehrlich, A., Notholt, J., Lüpkes, C., Macke, A., Burrows, J. P., Rinke, A., Quaas, J., Maturilli, M., Schemann, V., Shupe, M. D., Akansu, E. F., Barrientos-Velasco, C., Bärfuss, K., Blechschmidt, A.-M., Block, K., Bougoudis, I., Bozem, H., Böckmann, C., Bracher, A., Bresson, H., Bretschneider, L., Buschmann, M., Chechin, D. G., Chylik, J., Dahlke, S., Deneke, H., Dethloff, K., Donth, T., Dorn, W., Dupuy, R., Ebell, K., Egerer, U., Engelmann, R., Eppers, O., Gerdes, R., Gierens, R., Gorodetskaya, I. V., Gottschalk, M., Griesche, H., Gryanik, V. M., Handorf, D., Harm-Altstädter, B., Hartmann, J., Hartmann, M., Heinold, B., Herber, A., Herrmann, H., Heygster, G., Höschel, I., Hofmann, Z., Hölemann, J., Hünerbein, A., Jafariserajehlou, S., Jäkel, E., Jacobi, C., Janout, M., Jansen, F., Jourdan, O., Jurányi, Z., Kalesse-Los, H., Kanzow, T., Käthner, R., Kliesch, L. L., Klingebiel, M., Knudsen, E. M., Kovács, T., Körtke, W., Krampe, D., Kretzschmar, J., Kreyling, D., Kulla, B., Kunkel, D., Lampert, A., Lauer, M., Lelli, L., von Lerber, A., Linke, O., Löhnert, U., Lonardi, M., Losa, S. N., Losch, M., Maahn, M., Mech, M., Mei, L., Mertes, S., Metzner, E., Mewes, D., Michaelis, J., Mioche, G., Moser, M., Nakoudi, K., Neggers, R., Neuber, R., Nomokonova, T., Oelker, J., Papakonstantinou-Presvelou, I., Pätzold, F., Pefanis, V., Pohl, C., van Pinxteren, M., Radovan, A., Rhein, M., Rex, M., Richter, A., Risse, N., Ritter, C., Rostosky, P., Rozanov, V. V., Ruiz Donoso, E., Saavedra-Garfias, P., Salzmann, M., Schacht, J., Schäfer, M., Schneider, J., Schnierstein, N., Seifert, P., Seo, S., Siebert, H., Soppa, M. A., Spreen, G., Stachlewska, I. S., Stapf, J., Stratmann, F., Tegen, I., Viceto, C., Voigt, C., Vountas, M., Walbröl, A., Walter, M., Wehner, B., Wex, H., Willmes, S., Zanatta, M., and Zeppenfeld, S.: Atmospheric and Surface Processes, and Feedback Mechanisms Determining Arctic Amplification: A Review of First Results and Prospects of the (AC)3 Project, Bull. Amer. Meteorol. Soc., 104, E208–E242, https://doi.org/10.1175/BAMS-D-21-0218.1, 2023.

Wendisch, M., Crewell, S., Ehrlich, A., Herber, A., Kirbus, B., Lüpkes, C., Mech, M., Abel, S. J., Akansu, E. F., Ament, F., Aubry, C., Becker, S., Borrmann, S., Bozem, H., Brückner, M., Clemen, H.-C., Dahlke, S., Dekoutsidis, G., Delanoë, J., De La Torre Castro, E., Dorff, H., Dupuy, R., Eppers, O., Ewald, F., George, G., Gorodetskaya, I. V., Grawe, S., Groß, S., Hartmann, J., Henning, S., Hirsch, L., Jäkel, E., Joppe, P., Jourdan, O., Jurányi, Z., Karalis, M., Kellermann, M., Klingebiel, M., Lonardi, M., Lucke, J., Luebke, A. E., Maahn, M., Maherndl, N., Maturilli, M., Mayer, B., Mayer, J., Mertes, S., Michaelis, J., Michalkov, M., Mioche, G., Moser, M., Müller, H., Neggers, R., Ori, D., Paul, D., Paulus, F. M., Pilz, C., Pithan, F., Pöhlker, M., Pörtge, V., Ringel, M., Risse, N., Roberts, G. C., Rosenburg, S., Röttenbacher, J., Rückert, J., Schäfer, M., Schaefer, J., Schemann, V., Schirmacher, I., Schmidt, J., Schmidt, S., Schneider, J., Schnitt, S., Schwarz, A., Siebert, H., Sodemann, H., Sperzel, T., Spreen, G., Stevens, B., Stratmann, F., Svensson, G., Tatzelt, C., Tuch, T., Vihma, T., Voigt, C., Volkmer, L., Walbröl, A., Weber, A., Wehner, B., Wetzel, B., Wirth, M., and Zinner, T.: Overview: quasi-Lagrangian observations of Arctic air mass transformations – introduction and initial results of the HALO-(AC)^3 aircraft campaign, Atmos. Chem. Phys., 24, 8865–8892, https://doi.org/10.5194/acp-24-8865-2024, 2024.

Wendisch, M., Kirbus, B., Ori, D., Shupe, M. D., Crewell, S., Sodemann, H., and Schemann, V.: Observed and modeled Arctic airmass transformations during warm air intrusions and cold air outbreaks, Atmos. Chem. Phys., 25, 15047–15076, https://doi.org/10.5194/acp-25-15047-2025, 2025.

Williamson, C., Kupc, A., Wilson, J., Gesler, D. W., Reeves, J. M., Erdesz, F., McLaughlin, R., and Brock, C. A.: Fast time response measurements of particle size distributions in the 3–60 nm size range with the nucleation mode aerosol size spectrometer, Atmos. Meas. Tech., 11, 3491–3509, https://doi.org/10.5194/amt-11-3491-2018, 2018.

Woods, S., Lawson, R. P., Jensen, E., Bui, T. P., Thornberry, T., and coauthors: Microphysical Properties of Tropical Tropopause Layer Cirrus. Journal of Geophysical Research: Atmospheres, 123(11), 6053-6069. https://doi.org/10.1029/2017JD028068, 2018.

Wright, N. C. and Polashenski, C. M.: Open-source algorithm for detecting sea ice surface features in high-resolution optical imagery, The Cryosphere, 12, 1307–1329, https://doi.org/10.5194/tc-12-1307-2018, 2018.

https://doi.org/10.5194/essd-2026-241
Preprint. Discussion started: 24 July 2026

Wu, J., Liu, J., Gunsch, M. J., Mirrielees, J. A., Moffett, C. E., Zhang, Q., Sheesley, R. J., and Pratt, K. A.: Quantifying the Diversity of an Atmospheric Aerosol Population in an Arctic Oil Field on a Single-Particle Level, *Journal of Geophysical Research: Atmospheres*, 129, e2024JD041001, https://doi.org/10.1029/2024JD041001, 2024.

Wu, D., Wang, Z., Wechsler, P., Mahon, N., Deng, M., Glover, B., Burkhart, M., Kuestner, W., and Heesen, B.: Airborne compact rotational Raman lidar for temperature measurement, Opt. Express, 24, A1210–A1223, 2016.

Wu, M., Liu, X., Yu, H., Wang, H., Shi, Y., Yang, K., Darmenov, A., Wu, C., Wang, Z., Luo, T., Feng, Y., and Ke, Z.: Understanding processes that control dust spatial distributions with global climate models and satellite observations, *Atmospheric Chemistry and Physics*, 20, 13835–13855, https://doi.org/10.5194/acp-20-13835-2020, 2020.

Xian, P., Zhang, J., O'Neill, N. T., Toth, T. D., Sorenson, B., Colarco, P. R., Kipling, Z., Hyer, E. J., Campbell, J. R., Reid, J. S., and Ranjbar, K.: Arctic spring and summertime aerosol optical depth baseline from long-term observations and model reanalyses – Part 1: Climatology and trend, *Atmospheric Chemistry and Physics*, 22, 9915–9947, https://doi.org/10.5194/acp-22-9915-2022, 2022.

Xiao, Q., Zhang, J., Wang, Y., Ziemba, L. D., Crosbie, E., Winstead, E. L., Robinson, C. E., DiGangi, J. P., Diskin, G. S., Reid, J. S., Schmidt, K. S., Sorooshian, A., Hilario, M. R. A., Woods, S., Lawson, P., Stamnes, S. A., and Wang, J.: New particle formation in the tropical free troposphere during CAMP2Ex: statistics and impact of emission sources, convective activity, and synoptic conditions, Atmos. Chem. Phys., 23, 9853–9871, https://doi.org/10.5194/acp-23-9853-2023, 2023.

Zamora, L. M., Kahn, R. A., Evangeliou, N., Groot Zwaaftink, C. D., and Huebert, K. B.: Comparisons between the distributions of dust and combustion aerosols in MERRA-2, FLEXPART, and CALIPSO and implications for deposition freezing over wintertime Siberia, *Atmospheric Chemistry and Physics*, 22, 12269–12285, https://doi.org/10.5194/acp-22-12269-2022, 2022.

Zaveri, R. A., Wang, J., Fan, J., Zhang, Y., Shilling, J. E., Zelenyuk, A., Mei, F., Newsom, R., Pekour, M., Tomlinson, J., Comstock, J. M., Shrivastava, M., Fortner, E., Machado, L. A. T., Artaxo, P., and Martin, S. T.: Rapid growth of anthropogenic organic nanoparticles greatly alters cloud life cycle in the Amazon rainforest, *Science Advances*, 8, eabj0329, https://doi.org/10.1126/sciadv.abj0329, 2022.

Ziemba L. D., Thornhill, K. L., Ferrare, R., Barrick, J., and coauthors: Airborne observations of aerosol extinction by in situ and remote-sensing techniques: Evaluation of particle hygroscopicity, Geophys. Res. Lett., 40, 417–422, https://doi.org/10.1029/2012GL054428, 2013.

Zheng, G. J., Wang, Y., Wood, R., Jensen, M. P., Kuang, C. A., McCoy, I. L., Matthews, A., Mei, F., Tomlinson, J. M., Shilling, J. E., Zawadowicz, M. A., Crosbie, E., Moore, R., Ziemba, L., Andreae, M. O., and Wang, J.: New particle formation in the remote marine boundary layer, *Nature Communications*, 12, https://doi.org/10.1038/s41467-020-20773-1, 2021.

Zhuravleva, T. B., Artyushina, A. V., Vinogradova, A. A., and Voronina, Yu. V.: Black Carbon in the Near-Surface Atmosphere Far Away from Emission Sources: Comparison of Measurements and MERRA-2 Reanalysis Data, *Atmos Ocean Opt*, 33, 591–601, https://doi.org/10.1134/S1024856020060251, 2020.

Zuidema, P., Geerts, B., McFarquhar, G., Bailey, A., Cassano, J., Doyle, J., French, J., Perkins, R., Petters, M., Snider, J., Wang, Y., Wang, Z., et al.: Flying into the Cold: The NSF Cold Air outbreak Experiment in the Sub-Arctic Region (CAESAR), Bull. Am. Meteor. Soc., manuscript ID BAMS-D-25-0241, https://doi.org/10.22541/essoar.176894796.63570701/v1, 2026.

Zuidema, P., Leon, D., Pazmany, A., and Cadeddu, M.: Aircraft millimeter-wave passive sensing of cloud liquid water and water vapor during VOCALS-REx, Atmos. Chem. Phys., 12, 355–369, https://doi.org/10.5194/acp-12-355-2012, 2012.